

MICROSTRUCTURAL EVOLUTION AND OXIDATION BEHAVIOR OF ALNICRCOSI
MULTI-COMPONENT ALLOYS

by

JOEL PHILIP ALFANO

MARK L. WEAVER, COMMITTEE CHAIR
VIOLA L. ACOFF
MARCUS D. ASHFORD
AMBER GENAU
SUBHADRA GUPTA
GREGORY B. THOMPSON

A DISSERTATION

Submitted in partial fulfillment of the requirements
for the degree of Doctor of Philosophy in the
Department of Metallurgical and Materials Engineering
in the Graduate School of
The University of Alabama

TUSCALOOSA, ALABAMA

2013

Copyright Joel Philip Alfano 2013
ALL RIGHTS RESERVED

ABSTRACT

Equiatomic or near-equiatomic multicomponent alloys, often termed high-entropy alloys (HEAs), are an emerging class of metallic materials that are being investigated for a wide range of technical applications. Unlike conventional engineering alloys, HEAs lack a principal component and are instead composed of at least five major metallic elements, each with compositions generally ranging from 5 to 35 at. %. Unlike conventional alloys, HEAs have high entropies of mixing that are said to enhance the formation of solid solutions and other metastable phases resulting in materials exhibiting unique combinations of properties including high thermal stability, high strength/hardness, and high corrosion/oxidation resistance. Most studies of HEAs have focused on optimizing microstructures or mechanical properties. Relatively few have designed an alloy for or investigated oxidation behavior of HEAs.

This dissertation describes the microstructural evolution and oxidation behavior of three HEA alloys that were designed with the intent to provide high oxidation resistance whilst offering the possibility for high temperature precipitation hardening. The alloys were intentionally designed to contain four elements that are commonly utilized in high temperature high-temperature Ni-based alloys, Al, Ni, Cr, and Co. A fifth element, Si, was also added. Though not a typical addition to structural Ni-based superalloys, it has been shown to improve their resistance to oxidation, hot corrosion, and wear, particularly when incorporated into surface layers or protective coatings [1-6]. All of the alloys investigated were designed using the phase selection rules proposed by Yang and Zhang which predicted that the alloys would consist of a mixture of solid solution and intermetallic phases in the as-cast or as-deposited state [7]. Two

alloys were designed to have higher concentrations of Al and Cr, thus maximizing the possibility of forming disordered BCC phases, while one was designed to have lower concentrations of Al and Cr, thus maximizing the chances of forming disordered FCC phases.

Detailed microstructural and chemical analysis showed that characterizations have confirmed the presence of the expected solid solution phases, however, the majority phases in all of the alloys were found to be ordered intermetallics which increased in volume fraction upon annealing. The majority of the phases that formed were consistent with thermodynamic predications made using the Thermo-Calc™ software package; however the alloys were subject to phase transformations that could not be predicted using existing thermodynamic data.

Isothermal and cyclic oxidation tests demonstrated that both sets of alloys were capable of forming aluminum oxide (aka alumina) surface scales, but that alloys containing higher Al and Cr were more stable. Coatings with similarly high Al and Cr levels were found to significantly improve the oxidation resistance of pure Ni and to exceed the 250 h oxidation upon the already excellent oxidation resistance of β -NiAl based coatings. This result was surprising in that the HEA coatings produced in this study were thinner and were deposited on a less oxidation resistant substrate than the β -NiAl based coatings.

Collectively these results have confirmed that complex multicomponent HEAs that are capable of forming protective alumina scales can be designed and processed using existing phase selection rules. These results also reiterate the need for refinement of the phase selection rules for HEA formation and improved thermodynamic databases to facilitate the design of better HEAs.

DEDICATION

This dissertation is dedicated to everyone who provided help and support during the research and formation of this document. Specifically, my wife Christine who provided continual support and encouragement as well as the many friends and colleagues who provide insight.

LIST OF ABBREVIATIONS AND SYMBOLS

Abbreviations:

APT	Atom probe tomography
at. %	Atomic percent
EDS	Energy dispersive spectrometer
HAADF	High angle annular dark field
HEA	High Entropy Alloy
SAED	Selected area electron diffraction
SEM	Scanning electron microscopy
STEM	Scanning Transmission Electron Microscopy
TBC	Thermal barrier coating
TEM	Transmission electron microscope
TGO	Thermally grown oxide
wt. %	Weight percent
XRD	X-ray diffraction

Symbols:

β	Ordered BCC intermetallic phase with B2 crystal structure
σ	Body-centered tetragonal phase
χ	Body-centered cubic phase ($\text{Co}_{50}\text{Cr}_{30}\text{Si}_{20}$)
γ	Disordered FCC phase with A1 crystal structure

γ'	Ni_3Al
L1_0	Martensite ($\text{Al}_{29}\text{Co}_{38}\text{Ni}_{33}$)
L1_2	Ordered FCC intermetallic phase with Cu_3Au structure
G	$\text{Ni}_{16}\text{Si}_7\text{Cr}_6$

ACKNOWLEDGEMENTS

In this opportunity, I would like to thank my advisor, Dr. Mark L Weaver. For his continued support, guidance, and encouragement that made this work possible.

I would also like to thank my committee members Marcus Ashford, Viola Acoff, Greg Thompson, Su Gupta, and Amber Genau for their valuable insight and assistance.

I would like to thank Johnny Goodwin and Rich Martens for their help with training and operation of the Central Analytical Facility (CAF) equipment. Specifically Rich for his help and assistance on the LEAP and Johnny for continually trouble shooting my problems on the TEM.

Finally I would like to thank my colleges: Todd Butler, Bradford Shultz, Chad Hornbuckle, and Nicholas De Leon among others for helping me working through research problems and providing insight into the microstructural analysis.

TABLE OF CONTENTS

ABSTRACT	ii
DEDICATION	iv
LIST OF ABBREVIATIONS AND SYMBOLS	v
Abbreviations:	v
Symbols:	v
ACKNOWLEDGEMENTS	vii
LIST OF TABLES	xi
LIST OF FIGURES	xii
1. INTRODUCTION	1
1.1 General Background	1
1.2 Motivation	2
2. LITERATURE REVIEW	3
2.1 HEA Phase Prediction:	3
2.2 Phase Prediction via Computational Modeling	7
2.3 Effect of Composition on Microstructure	8
2.4 HEAs as Coating Systems	11
3. EXPERIMENTAL PROCEDURE	13

3.1 Production of Bulk Multi-Component Alloys.....	13
3.2 Production of Multi-Component Alloy Coatings.....	13
3.3 Heat Treatment, Hardness Testing, and Oxidation Testing	15
3.4 Microstructural Characterization.....	16
4. $\text{Al}_{20}\text{Ni}_{25}\text{Cr}_{25}\text{Co}_{25}\text{Si}_5$ ALLOY.....	17
4.1 Alloy Design and Crystal Structures.....	17
4.2 Microstructure of the As-Cast Alloy.....	17
4.3 Influences of Annealing	26
4.4 Comparison of Experimental and Computed Phase Equilibria.....	37
4.5 Isothermal Oxidation Behavior.....	41
4.6 Conclusions.....	55
5. $\text{Al}_{15}\text{Ni}_{35}\text{Cr}_{15}\text{Co}_{35}\text{Si}_5$ ALLOY.....	57
5.1 Alloy Design and Crystal Structure	57
5.2 Influence of Annealing on Microstructure.....	62
5.3 Comparison of Experimental and Computed Phase Equilibria.....	69
5.4 Isothermal Oxidation Behavior.....	74
5.5 Conclusions.....	84
6. $\text{Al}_{17}\text{Ni}_{28}\text{Cr}_{26}\text{Co}_{28}\text{Si}_1$ COATINGS.....	85
6.1 As-Cast and Annealed Microstructure	85
6.2 Oxidation Behavior.....	92

6.3 Conclusions	96
7. GENERAL DISCUSSION AND CONCLUSIONS	101
7.1 Summary and Discussion of Work.....	101
7.2 Conclusions	105
7.3 Suggestions for Future Work	106
REFERENCES	110

LIST OF TABLES

Table 3-1: Power settings used to deposit the $\text{Al}_{17}\text{Ni}_{28}\text{Cr}_{26}\text{Co}_{28}\text{Si}_1$ coatings.	14
Table 4-1: Chemical compositions and lattice parameters for the phases observed in the $\text{Al}_{20}\text{Cr}_{25}\text{Co}_{25}\text{Ni}_{25}\text{Si}_5$ alloy in the as-cast state.	21
Table 4-2: Chemical compositions and lattice parameters for the phases observed in the $\text{Al}_{20}\text{Cr}_{25}\text{Co}_{25}\text{Ni}_{25}\text{Si}_5$ alloy after annealing at $700^\circ\text{C}/5$ hr.	32
Table 4-3: Chemical compositions and lattice parameters for the phases observed in the $\text{Al}_{20}\text{Cr}_{25}\text{Co}_{25}\text{Ni}_{25}\text{Si}_5$ alloy after annealing at $900^\circ\text{C}/100$ h.	34
Table 4-4: Comparison of the phases observed experimentally with those determined using Thermo-Calc™.	40
Table 4-5: Isothermal oxidation results for the as-cast alloy (at.%).	42
Table 4-6: Compositions of the three main phases observed in the oxidized samples.	46
Table 4-7: Composition values for phases observed in atom probe analysis (at.%).	49
Table 5-1: Compositions of the (gamma)-region and martensitic region (at.%).	61
Table 5-2: Compositions of the γ -matrix with γ' -precipitates as determined via APT (at.%).	64
Table 5-3: Compositions of the G-phase and surrounding matrix as determined via APT (at.%).	71
Table 5-4: Comparison of the phases observed experimentally to that determined via Thermo-Calc	73
Table 5-5: Oxidation results for the $\text{Al}_{20}\text{Cr}_{25}\text{Co}_{25}\text{Ni}_{25}\text{Si}_5$ alloy.	76
Table 6-1: Phase compositions as determined via APT for the sputter deposited coating after annealing at $600^\circ\text{C}/500$ h.	90
Table 6-2: Coating composition after each step of isothermal oxidation at 1050°C	97
Table 6-3: Composition of Al depleted zone and Al rich zone within CMSX-4.	98
Table 7-1: Design of Experiments to determine optimum sputtering conditions.	109

LIST OF FIGURES

Figure 2-1: Relationship between parameters δ and Ω for multi-component alloys. Figure re-plotted from reference [7].	5
Figure 2-2: Relationship between ΔS_{mix} , ΔH_{mix} , and δ . Figure re-plotted from references [7,14].	5
Figure 4-1: XRD patterns for $\text{Al}_{20}\text{Cr}_{25}\text{Co}_{25}\text{Ni}_{25}\text{Si}_5$ in the as-cast and annealed conditions. (a) As-cast, (b) annealed at $700^\circ\text{C}/5$ h, (c) annealed at $700^\circ\text{C}/1000$ h, and (d) annealed at $900^\circ\text{C}/100$ h.....	19
Figure 4-2: SEM backscattered electron images of the $\text{Al}_{20}\text{Cr}_{25}\text{Co}_{25}\text{Ni}_{25}\text{Si}_5$ alloy in the as-cast state. (a) Low magnification; (b) and (c) high magnification.	20
Figure 4-3: Mosaic STEM-HAADF image illustrating the morphological differences observed in the dendritic and interdendritic regions of the cast alloy. Note the presence of high atomic number contrast platelets in the dendritic regions and interconnected high atomic number contrast strands within the interdendritic regions.	23
Figure 4-4: Brightfield TEM micrographs and SAED patterns collected from zone A of the as-cast alloy. (a) The dendritic region showing disordered BCC precipitates in an ordered B2 matrix. (b) SAED pattern of the $\langle 001 \rangle_{\text{B2}}$ zone axis. (c) SAED pattern of the $\langle 001 \rangle_{\text{BCC}}$ zone axis.	24
Figure 4-5: Atom probe reconstruction of precipitates observed for the as-cast alloy with corresponding TEM bright field image.	25
Figure 4-6: Brightfield TEM micrographs and SAED patterns collected from zone B of the as-cast alloy. (a) The interdendritic region showing σ phase precipitates in an ordered B2 matrix. (b) SAED pattern of the $\langle 012 \rangle_{\sigma}$ zone axis. (c) SAED pattern of the $\langle 011 \rangle_{\text{B2}}$ zone axis.	27
Figure 4-7: SEM backscattered electron images of the $\text{Al}_{20}\text{Cr}_{25}\text{Co}_{25}\text{Ni}_{25}\text{Si}_5$ alloy after annealing. (a and b) Annealed at $700^\circ\text{C}/5$ h. (c and d) Annealed at $700^\circ\text{C}/1000$ h. (e and f) Annealed at $1000^\circ\text{C}/100$ h.	29
Figure 4-8: TEM results after aging at 700°C for 5 h. (a) Bright-field image; (b) STEM-HAADF image; (c) SAED pattern collected from the σ -phase; (d) SAED pattern collected from the χ -phase illustrating coherency with the B2 matrix; and (e) SAED pattern collected from the needles indicating a disordered FCC crystal structure.	30
Figure 4-9: (a) Atom probe reconstruction of precipitates observed after aging at 700°C for 5 h. (b) Bright-field image; (c) STEM-HAADF image; (d) SAED pattern collected from the σ -phase;	

(e) SAED pattern collected from the χ -phase illustrating coherency with the B2 matrix; and (f) SAED pattern collected from the needles indicating a disordered FCC crystal structure. Dimensions in (a) are in nm.	31
Figure 4-10: TEM results after aging at 700°C for 1000 h. (a) Bright-field image; (b) STEM-HAADF image; (c) SAED pattern collected from the σ -phase.	33
Figure 4-11: TEM results after aging at 900°C for 100 h. (a) A bright field TEM image collected from the dendritic region along with an SAED pattern for the B2 phase. (b) A bright field TEM image collected from the interdendritic region along with an SAED pattern for the σ phase. (c) A STEM-HAADF image collected from the boundary between dendritic and interdendritic regions.	36
Figure 4-12: Variation in Vickers hardness with aging time for $\text{Al}_{20}\text{Cr}_{25}\text{Co}_{25}\text{Ni}_{25}\text{Si}_5$	38
Figure 4-13: Equilibrium phase fractions (mole) as a function of temperature for the $\text{Al}_{20}\text{Cr}_{25}\text{Co}_{25}\text{Ni}_{25}\text{Si}_5$ alloy. Calculations were done using Thermo-Calc™ and the TCNI5 database.	39
Figure 4-14: XRD patterns of the $\text{Al}_{20}\text{Cr}_{25}\text{Co}_{25}\text{Ni}_{25}\text{Si}_5$ for as-cast, 20 h, 96 h, 500 h, and 1000 h oxidized samples at 1050°C.	44
Figure 4-15: Backscattered SEM images of the oxide scale and microstructure within the alloy after (A) 20 h (B) 96 h and (C) 500 h of isothermal oxidation at 1050°C.	45
Figure 4-16: (a) Brightfield TEM image of 20 h oxidized sample with TEM diffraction for (b) σ region and (c) B2 region. (d) Brightfield TEM image of γ -FCC region with accompanying SAED pattern.	47
Figure 4-17: Three dimensional APT reconstructions of: (a) the B2 region revealing the presence of Cr-rich σ phase precipitates; and (b) the interface between coarse σ phase and a B2 region. Dimensions are in nm.	48
Figure 4-18: Mass gain curve for stepped/sequential oxidation tests at 1050°C.	51
Figure 4-19: BSE images of the oxide formation for the $\text{Al}_{15}\text{Cr}_{10}\text{Co}_{35}\text{Ni}_{35}\text{Si}_5$ alloy after 5 h (a), 10 h (b), 24 h, and 50 h of oxidation at 1050°C and cross sectional BSE images of the alloy (e) and oxide scale (f) after 100 h of oxidation.	52
Figure 4-20: XRD patterns for the $\text{Al}_{20}\text{Cr}_{25}\text{Co}_{25}\text{Ni}_{25}\text{Si}_5$ alloy after oxidation for (a) 5 h, (b) 10 h, (c) 25 h, (d) 50 h, (e) 100 h at 1050°C.	53
Figure 5-1: SEM backscattered electron images of the $\text{Al}_{15}\text{Cr}_{10}\text{Co}_{35}\text{Ni}_{35}\text{Si}_5$ alloy in the as-cast state. (a) Low magnification image showing disordered NiCo FCC regions (labeled A) and martensitic regions (labeled B). (b) A higher magnification SEM image.	58
Figure 5-2: XRD patterns for the $\text{Al}_{15}\text{Cr}_{10}\text{Co}_{35}\text{Ni}_{35}\text{Si}_5$ alloy in the as-cast and select annealed conditions. (a) As-cast, (b) 600°C/20 h, and (c) 900°C/100 h.	59

Figure 5-3: TEM bright field images and SAED patterns collected from regions A and B in the microstructure. Figures (a) and (c), which were collected from region A, indicate the presence of γ -FCC and γ' -L1 ₂ phases. Figures (b) and (d), which were collected from region B, indicate the presence of a twinned L1 ₀ martensite.	60
Figure 5-4: A 3D reconstruction of the Al ₁₅ Cr ₁₀ Co ₃₅ Ni ₃₅ Si ₅ alloy showing γ' -precipitation (green) within a γ -matrix (blue). Dimensions are in nm.	63
Figure 5-5: Variation in Vickers hardness with aging time for Al ₁₅ Cr ₁₀ Co ₃₅ Ni ₃₅ Si ₅ alloy	65
Figure 5-6: SEM backscattered electron image of the Al ₁₅ Cr ₁₀ Co ₃₅ Ni ₃₅ Si ₅ alloy after aging for 600°C/20 hr (a-b) and 900°C/100 hr (c-d).	66
Figure 5-7: STEM-HAADF image illustrating the needle-like G phase precipitates in the martensitic region of the 600°C/20 hr heat treated specimen with accompanying SAED patterns for the two regions.	67
Figure 5-8: Brightfield TEM images showing needle-like G-phase precipitates and an SAED pattern collected from one of the precipitates.	68
Figure 5-9: A 3D reconstruction of the G-phase precipitates with accompanying concentration profile for a select precipitate. Dimensions are in nm.	70
Figure 5-10: Thermo-Calc equilibrium phase diagram calculated for Al ₁₅ Cr ₁₀ Co ₃₅ Ni ₃₅ Si ₅ using the CALPHAD method with the TCNI5 database.	72
Figure 5-11: Backscattered SEM images of the oxide scale and microstructure within the alloy for (a) 20 h (b) 96Hrs and (c) 500 h of isothermal oxidation at 1050°C	75
Figure 5-12: XRD pattern of the Al ₁₅ Cr ₁₀ Co ₃₅ Ni ₃₅ Si ₅ alloy for the as-cast and oxidized states. (a) as-cast, (b) 20 h oxidized, (c) 96 h oxidation, (d) 500 h oxidation	78
Figure 5-13: Brightfield TEM images and associated SAED patterns collected from regions A and B of the alloy after oxidation at 1050°C. (a) and (c) were collected from region A showing the results of a martensitic transformation. (b) and (d) were collected from the region B which contained fine γ' precipitates dispersed in an FCC γ matrix.	79
Figure 5-14: Mass gain curve for stepped/sequential oxidation.	80
Figure 5-15: Backscattered electron images of the oxide formation for the Al ₁₅ Cr ₁₀ Co ₃₅ Ni ₃₅ Si ₅ alloy after 5 h (a), 10 h (b), 24 h, and 50 h of oxidation at 1050°C and cross sectional backscattered electron images of the alloy (e) and oxide scale (f) after 100 h of oxidation	81
Figure 5-16: XRD patterns for the Al ₁₅ Cr ₁₀ Co ₃₅ Ni ₃₅ Si ₅ alloy after oxidation for (A) 5 h, (B) 10 h, (C) 25 h, (D) 50 h, (E) 100 h at 1050°C.	82
Figure 6-1: XRD patterns for the Al ₁₇ Cr ₂₆ Co ₂₈ Ni ₂₈ Si ₁ coating on alumina in the as-cast and annealed conditions. (a) As-cast, (b) 600°C/0.25 h, (c) 600°C/100 h, and (d) 600°C/500 h.	86

Figure 6-2: Bright Field TEM imaged of microstructure for (a) 600°C/100 h and (b) 600°C/500 h with corresponding SAED patterns for (c) L1 ₀ with a twinning structure, (d) γ-FCC, and (e) σ phase.	87
Figure 6-3: 3-D reconstructions of the 4 phases observed within the 600°C/500 hr heat treated coating: (a) γ'-Ni ₃ Al, (b) τ ₃ -Al ₆ Ni ₃ Si, (c) γ-NiCo, (d) σ-CrCo. Dimensions are in nm.	89
Figure 6-4: Thermo-Calc TM phase predictions for AlNiCrCoSi coatings.	91
Figure 6-5: Mass change for oxidation time for pure Ni, Ni+HEA coating, CMSX-4 + HEA coating.	93
Figure 6-6: XRD patterns for the Al ₁₇ Cr ₂₆ Co ₂₈ Ni ₂₈ Si ₁ coating on CMSX-4 in the as-cast and oxidized states: (a) As-cast, (b) 600°C/0.25 h, (c) 600°C/100 h, and (d) 600°C/500 h.	94
Figure 6-7: Backscattered electron SEM images the isothermal oxidation test performed on CMSX-4 for: (a) As-deposited, (b) 5 h oxidation, (c) 115 h oxidation, (d) 240 h oxidation	95
Figure 6-8: A comparison of previously studied β-NiAl+Cr+Zr/Hf coatings to the HEA coating produced in this study. Isothermal oxidation at 1050°C.	99

1. INTRODUCTION

1.1 General Background

Equiatomic or near-equiatomic multicomponent alloys, often termed high-entropy alloys (HEAs), represent an emerging class of materials that are being investigated for a wide range of applications [8-12]. Unlike conventional engineering alloys, HEAs lack a principal component and are generally composed of at least five major metallic elements, each with compositions ranging from 5-35 at. %. They may also include additions of minor elements in concentration ranges of ≤ 5 at. % [7,13,14]. Many HEAs tend to form solid solution phases with simple FCC and/or BCC crystal structures, a fact often attributed to their having high entropies of mixing which suppresses the formation of intermetallic compounds or other equilibrium phases [8-12]. It has been proposed that the retention of simple solid solution structures will lead to the development of new alloys exhibiting unique combinations of physical and chemical properties [8-12]. However, many of these alloys can also form amorphous and/or intermetallic phases rather than (or in addition to) solid solution phases [11,15-21], which can be either beneficial or detrimental depending upon the intended application. This microstructural variability has prompted a considerable amount of research into the phase formation rules for HEAs in order to custom tailor desired alloy properties.

To date, the majority of the work on HEAs has focused on alloys containing Al, Ni, Cu, Fe, Co, Mn, and Cr [8-12]. Though it is often noted that HEAs exhibit good resistances to wear, oxidation, and corrosion, very few studies have been conducted that focus on the oxidation behavior of metallic HEAs [15,22-25].

This dissertation will provide insight into the microstructural evolution and oxidation behavior of multicomponent HEAs containing Al, Ni, Cr, Co, and Si by providing detailed microstructural characterizations of bulk $\text{Al}_{20}\text{Ni}_{25}\text{Cr}_{25}\text{Co}_{25}\text{Si}_5$ and $\text{Al}_{15}\text{Ni}_{35}\text{Cr}_{10}\text{Co}_{35}\text{Si}_5$ alloys in their annealed and oxidized states. Additionally, an $\text{Al}_{17}\text{Ni}_{28}\text{Cr}_{26}\text{Co}_{28}\text{Si}_1$ coating was produced via DC magnetron sputtering and similarly characterized to assess the potential for using these alloys as high temperature protective coatings. To facilitate alloy development and understanding, thermodynamic calculations were performed using the CALculation of PHase Diagram (CALPHAD) method to obtain an estimate of equilibrium phases in each alloy as a function of temperature [26]. The calculated results were compared with the experimental results to further elucidate phase relationships and understand performance.

1.2 Motivation

This study was motivated by the desire to develop HEAs that would be alumina-formers, maintain chemical compatibility with commercial high-temperature alloys (i.e., superalloys and stainless steels), and exhibit high hardness/strength due to precipitation hardening mechanisms. As such, two bulk HEAs, $\text{Al}_{20}\text{Ni}_{25}\text{Cr}_{25}\text{Co}_{25}\text{Si}_5$ and $\text{Al}_{15}\text{Ni}_{35}\text{Cr}_{10}\text{Co}_{35}\text{Si}_5$, and one sputter-deposited coating, $\text{Al}_{17}\text{Ni}_{28}\text{Cr}_{26}\text{Co}_{28}\text{Si}_1$, were investigated experimentally. The focus was to investigate microstructural evolution during annealing and oxidation. It is expected that the results of this dissertation will provide a better understanding of HEAs and the feasibility of their use in high temperature environments by examining isothermal and cyclic oxidation behavior of the previously mentioned alloys and coating.

2. LITERATURE REVIEW

2.1 HEA Phase Prediction:

Zhang and co-workers [12,14] have proposed that minimal atomic size differences and near-zero values of the entropy of mixing promotes the formation of solid solutions in HEAs. In particular, solid-solution forming HEAs should possess an atomic size difference (δ) of less than 4.6%, an enthalpy of mixing (ΔH_{mix}) ranging from -2.685δ -2.54 kJ/mol to -1.28δ +5.44 kJ/mol (i.e., -15 to +5 kJ/mol), and an entropy of mixing (ΔS_{mix}) exceeding 1.61R, where R is the ideal gas constant. Ordered solid solution phases could form either as precipitates or as the primary phase for the same ΔH_{mix} and ΔS_{mix} but with $4.6\% < \delta < 6.6\%$, though unambiguous delineation between regimes cannot be provided [12,14].

More recently, these rules have been revised [7,20] by incorporating a new parameter, Ω , that combines the effects of ΔH_{mix} and ΔS_{mix} along with the average melting temperature of the alloy components (T_m). The parameters used are defined as follows:

$$\Omega = \frac{T_m \Delta S_{mix}}{|\Delta H_{mix}|}, \quad (2-1)$$

$$T_m = \sum_{i=1}^n c_i (T_m)_i, \quad (2-2)$$

$$\delta = \sqrt{\sum_{i=1}^n c_i (1 - r_i / \bar{r})^2}, \quad (2-3)$$

$$\bar{r} = \sum_{i=1}^n c_i r_i, \quad (2-4)$$

where T_m is the average melting temperature of the n -element alloy estimated using the rule of mixtures, c_i is the mole percent of component i , $(T_m)_i$ is the melting point of component i , r_i is the atomic radius of component i , and \bar{r} is the average atomic radius. Yang and Zhang [7] deduced that solid solution phases should form in alloys with $\Omega \geq 1.1$ and $\delta \leq 6.6\%$, whereas combinations phases would form in alloys not satisfying these criteria. The enthalpies of mixing for any two elements have been tabulated by Takeuchi et. al [27]. To properly determine these values one has to make an assumption that ΔG at a certain composition is approximately equal to the free energy of mixing (ΔG_{mix}) of the liquid phases.

From the parameters Ω and δ , the graph presented in Fig. 2-1 can be formed, which provides an approximation of the conditions required to form each type of microstructure. The region enclosed in the dashed lines represents alloys that fall within the predicted HEA region, $\delta \leq 6.6\%$ and $\Omega \geq 1.1$, presented by Yang *et. al.* [7]. Within this region, the green triangle highlights HEA alloys that form solid solutions. The blue region represents the area where a solid solution plus intermetallic phase are likely to form, while the red and green regions represent the intermetallic and bulk metallic glass phase formation areas, respectively.

Additional studies have been performed to determine the effect of ΔS_{mix} and ΔH_{mix} on phase formation. Zhang *et. al.* investigated their influence on the formation of solid solutions, intermediate phases, and bulk metallic glasses [14]. They found that a higher ΔS_{mix} results in the formation of a solid solution. This is the result of lowering the free energy, which reduces the atom's desire to segregate, making a stable solid solution more favorable than an intermetallic or a bulk metallic glass (BMG). This is also true when looking at the ΔH_{mix} . Lower ΔH_{mix} results in the formation of bulk metallic glasses because of a higher free energy. The correlation between ΔS_{mix} , ΔH_{mix} , and δ can be seen in Fig. 2-2.

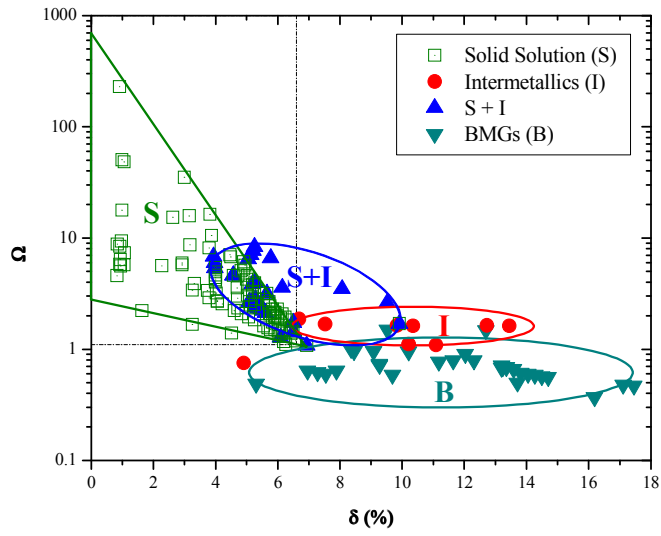


Figure 2-1: Relationship between parameters δ and Ω for multi-component alloys. Figure re-plotted from reference [7].

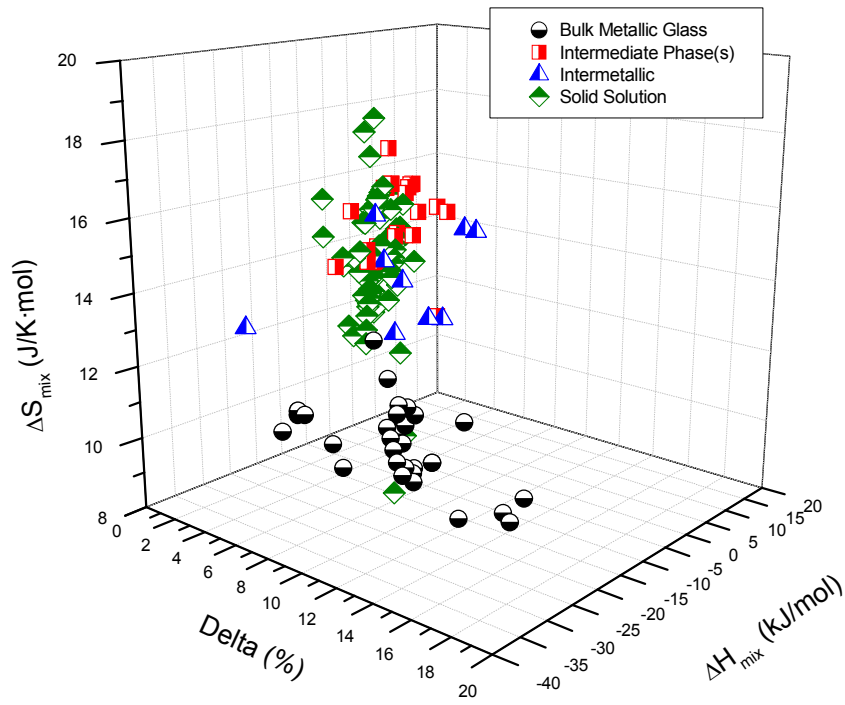


Figure 2-2: Relationship between ΔS_{mix} , ΔH_{mix} , and δ . Figure re-plotted from references [7,14].

Guo *et. al.* augmented the work of Zhang *et. al.* by incorporating the electronegativity difference, which is defined by:

$$\Delta\chi = \sqrt{\sum_{i=1}^n c_i (\chi_i - \bar{\chi})^2} \quad (0-1)$$

where $\bar{\chi} = \sum_{i=1}^n c_i (\chi_i)$, and χ_i is the Pauling electronegativity for the i^{th} element [13]. Another parameter, the valence electron concentration (VEC), was also incorporated and is defined by:

$$VEC = \sum_{i=1}^n c_i (VEC)_i \quad (0-2)$$

where $(VEC)_i$ is the VEC for the i^{th} element. This study showed that the electronegativity has little effect on the formation of a solid solutions or amorphous phases. The VEC was found to exhibit only a minor effect on phase formation and stability, but has been shown to be helpful in predicting the formation of FCC or BCC solid solutions [28]. Interestingly, it was shown that the atomic size difference plays the largest role in determining whether a solid solution or BMG will form.

Otto *et. al.* investigated the effects of enthalpy and entropy on phase formation by investigating a known single phase solid solution HEA (CoCrFeMnNi) and making substitutions that would have little effect on the configurational entropy [29]. The study showed that configurational entropy played little to no role in the stabilization of a single phase solid solution, but that alloying elements could affect phase formation depending upon their tendency to form more favorable binary phases resulting in a multi-phase microstructure. Because of this Otto *et. al.* proposed calling only true solid solutions, such as those observed by Cantor *et. al.*, HEAs and all others multi-component alloys [29].

Guo et. al performed a similar investigation into the driving force for solid solution phase formation and determined that enthalpy and atomic size difference played a significant role in phase formation [19]. They found that to form a solid solution the atomic size difference δ must be less than 6.6% and ΔH_{mix} must be between -11.6 kJ/mol to 3.2 kJ/mol. Further refinement is then required to avoid the formation of intermetallic compounds. Guo et. al proposed that the formation of intermetallics is the result of high negative mixing enthalpies between alloying elements. To reduce intermetallic formation the concentration of the compounding element must be reduce; this often results in a smaller ΔH_{mix} and δ for solid solution formation.

2.2 Phase Prediction via Computational Modeling

Attempts have also been made to predict the phases formed in HEAs through computer modeling. Studies by Zhang *et. al.*, Ng *et. al.*, and Manzoni *et. al.* looked into the correlation between computer simulation and actual phase formation in bulk HEAs [30-32]. Manzoni *et. al.* compared AlCoCrCuFeNi HEAs with Al concentrations of 8 and 23at.% to the phases predicted by the CALPHAD method using the Thermo-Calc software package. The CALPHAD method uses the assumption that a thermodynamic description of a system can be achieved through the Gibbs energy of a phase because most thermodynamic properties can be derived from the Gibbs energy function [33,34]. The results showed good agreement between the calculated and experimentally observed phases for the higher concentration aluminum alloy, but there were noticeable discrepancies in phase concentration between the two methods. Specifically, the high concentration aluminum alloy was found experimentally to contain a B2 matrix (ordered BCC), A2 phase (disordered BCC), and Cu-rich platelets via TEM, which were all predicted by Thermo-Calc. For the low aluminum containing alloy, large inconsistencies were found between

the predictions and experimental results. Specifically, the low concentration aluminum alloy was found to have a Ni rich FCC matrix with a second main Ni-Al-rich phase with an ordered $L1_2$ structure, which was predicted in Thermo-Calc, but many other phases not found experimentally were predicted in the sample. The reason for the discrepancies was attributed to inadequate cooling time, which did not allow the alloy to reach equilibrium.

Ng *et al.* compared the phases that formed in $Al_{0.5}CoCrFeNi$ at varying temperatures to those predicted by Thermo-Calc and found close agreement between the predicted results and experimentally determined phase formation [31]. The main discrepancies between the experimental and Thermo-Calc results were the ordering of the FCC and BCC phases as well as the formation of a second FCC phase, which was not observed experimentally. The discrepancies are thought to be a result of the slow kinetics in the HEA system which inhibits the ordering process, increasing the time it takes for an alloy to reach equilibrium.

Zhang *et al.* compared the results of previously studied $AlCoCrFeNi$ alloys to those predicted using the CALPHAD approach [32]. In this study, phase diagrams were generated corresponding to varying aluminum ratios and compared with published experimental results. The predicted results match closely with experimental data in terms of the aluminum ratio for transitions FCC to FCC+BCC and finally to BCC. The slight discrepancies were again thought to be a result of the slow diffusion kinetics of HEAs, which may have prevented equilibrium from being reached.

2.3 Effect of Composition on Microstructure

The ability to predict which phases will form is important to the design of viable HEAs because certain phases provide different material properties, such as higher hardness for BCC

materials. As previously mentioned, studies on bulk HEAs have demonstrated their potential to provide improved properties over conventional alloys; specifically slow diffusion kinetics, high hardness, and high oxidation and corrosion resistance [8,9,32,35,36]. The studies on bulk HEAs have also showed that alloy composition greatly affects the microstructure. Li *et. al.* investigated the influences of varying the concentration of Al and the addition of Zr to the FeNiCrCoAl alloys [37]. The results showed that Al, which has an FCC structure, promotes the formation of a BCC structure. The study also showed that the addition of Al typically resulted in a dendritic crystal structure, which was also seen by many others [30,35,38-41]. This dendritic structure is coarsened with increasing Al content (Al concentration varied from 20 to 42.8 at. % in this study). The addition of Zr to the alloys helped promote a BCC structure and resulted in complex precipitation behavior. This was believed to be a result of the strong chemical bond between Zr and the alloying elements [37]. Similar results for the effect of aluminum on the alloy structure were seen by Chuang *et. al.*, who looked at varying the Al and Ti concentrations in AlCoCrFeNiTi alloys [35]. The addition of Al resulted in the formation of a coarse needle-like phase that increased the hardness of the alloy.

As previously stated, the elemental concentration can also affect the hardness of the material by changing the structure. The addition or increase in the concentration of Al has been shown to increase the hardness because the structure changes from FCC to BCC [35,37,41]. The addition of other elements, such as Zr or Hf, can increase the hardness by forming complex compounds and promoting precipitation throughout the alloy. It has also been proposed that for certain alloys the high hardness in HEAs is a result of sigma phase matrix in the alloy [38]. Tsai *et. al.* looked into an $Al_{0.3}CrFe_{1.5}MnNi_{0.5}$ alloy and found hardening behavior much different in comparison to traditional precipitation hardened alloys. The alloy reached peak hardness almost

immediately and did not over aged. In this alloy, the rapid hardening has been attributed to a phase transformation from BCC to tetragonal sigma. In this system very little diffusion was involved because the compositions of BCC and sigma phases are similar. Based on TEM results, the sigma phase was found to be a result of a supersaturated solution.

The oxidation behavior of HEAs is of importance if these alloys are to be used in high temperature environments. Chuang *et. al.* performed oxidation experiments on a series of AlCoCrFeNiTi HEAs with varying Al contents [35]. They reported little to no oxidation after 24 h at 600°C. However, when the tests were repeated at 800°C, slight oxidation was observed in the alloys resulting in mass gains on the order of 0.01 mg/mm². Alloys containing a higher concentration of Al were reported to have the lowest mass gains. Not enough data was collected to evaluate the oxidation kinetics of these alloys.

Chen *et. al.* performed oxidation experiments on a series of age-hardenable AlCrFeMnNi HEAs at 800°C for up to 200 h [41]. The Al concentrations in these alloys varied from 6.98 to 11.1at%. All of the investigated alloys obeyed the parabolic rate law during the initial stages of oxidation. Furthermore, it was found that alloys with higher Al contents provided superior oxidation protection. It was also reported that these alloys formed a dense and protective layer consisting of of Cr and Al oxides underneath a transient Mn oxide layer. This suggests that it might be possible to design HEAs that are capable of forming long-lasting Al oxide scales while simultaneously maintaining favorable mechanical properties.

Jiang and Luo studied the oxidation behavior of AlCuTiFeNiCr HEAs at 850°C [24]. They found that this alloy obeyed the parabolic rate law and that it formed a complex oxide scale consisting primarily of transient Ti_xO_y, (Ni,Ti)_xO_y, and (Ni,Cr,Fe)_xO_y with a small quantity of Al₂O₃. As their tests were only conducted for 400 h in static air, and no microstructural

information was reported, it could not be discerned whether a protective Al oxide scale formed beneath the transient oxides. However, the appearance of the specimen surfaces suggests this as a distinct possibility. Clearly more research is warranted to understand the oxidation behavior of HEAs.

2.4 HEAs as Coating Systems

Interest in the use of HEAs as protective coatings has spurred research into viable deposition methods. Huang *et. al.* have explored the production of AlSiTiCrFeNiMo-based HEA coatings, some containing Co, via thermal spraying [15]. This study demonstrated that this processing method was feasible, yielding materials with rapid age-hardening characteristics, high hardness, and favorable oxidation resistances up to 1100°C. However, very few details were provided about the microstructures or the mechanisms leading to the observed performance. In related work, Wang *et. al.* also used thermal spraying to produce NiCoFeCrSiAlTi-based HEAs, noting that this method of production yields alloys with rapid age-hardening characteristics and with high hardness at elevated temperatures [42]. Given, what has already been written about composition effects, the fact that Si has been shown to promote significant hardening in Al-containing Cu-free HEAs [17], and the well-known effects of Si on the behavior of traditional oxidation-resistant coating alloys [6], more investigations of alloys containing this addition are warranted.

Magnetron sputtering is another interesting deposition method for HEAs. The application of HEAs via magnetron sputtering is an area that has not been heavily studied but has recently been explored by V. Dolique *et. al.* [36,43,44]. Dolique focused on the anti-adhesion properties found in HEAs, specifically for use as an alternative to Teflon. In their work, an

AlCoCrCuFeNi-based HEA coating of was produced via magnetron sputtering onto 1 μm thick Si substrates. One goal of these studies was to investigate the effects small variations in element concentration on the structure and properties of the alloys. The alloys were deposited with the use of three mosaic targets and varying voltage to provide the desired compositions. The studies showed that for the given HEA an Al concentration below 15 at.% resulted in the formation of an FCC solid solution, while an Al concentration above 15 at.% resulted in a BCC solid solution [44]. These studies also showed that the presence of Ni and Co helped to stabilize the FCC structure. In general, these results matched the work of Wang *et. al.* who studied the influences of composition on bulk $\text{Al}_x\text{CoCrFeNi}$ alloys [45] who showed the Al contents of less than ~ 11 at.% yielded FCC solid solutions, while concentrations above $\sim 18\%$ yielded BCC solid solutions; however the specific compositional regimes were different. It is clear that chemical composition and processing methods can lead to changes in structure and properties, which can complicate the prediction of the structure of a sputtered alloy.

Feng *et. al.* also looked into the deposition of multi-element alloy films via magnetron sputtering [46]. A TaNbTiW film was deposited using two alloy targets of equal Ti:W and Ta:Nb along with a single Ta target to create the films. The films were found to be a single phase with a BCC crystal structure that was not affected by annealing temperature or time. The films also exhibited a relatively low residual stress, below 2.0 GPa, which reduces the risk of spallation at high temperatures.

3. EXPERIMENTAL PROCEDURE

3.1 Production of Bulk Multi-Component Alloys

Bulk alloy buttons were produced by vacuum arc melting in a Ti-gettered, high-purity argon atmosphere on a water-cooled copper hearth. Raw materials with purities exceeding 99.5% were used. Alloy buttons were melted at least five times to promote homogeneity.

3.2 Production of Multi-Component Alloy Coatings

Direct current magnetron sputtering was used to deposit the multicomponent alloy $\text{Al}_{17}\text{Ni}_{28}\text{Cr}_{26}\text{Co}_{28}\text{Si}_1$. The coatings were deposited from elemental and alloy sputtering targets with dimensions of 50.8 mm diameter \times 6.1 mm thickness or 50.8 mm diameter \times 3.2 mm thickness. The targets used included pure Ni, Cr, and Co along with an Al-5 at.% Si alloy target. All of the target materials had purities of 99.95% or higher.

To obtain the desired composition, stage rotation with a speed of 20 rpm was used in conjunction with varying power for each target based on deposition rate. The deposition powers used for each target are summarized in Table 3-1.

Coatings, approximately 10 μm in thickness, were deposited onto polycrystalline alumina, high-purity nickel, and single crystal CMSX-4TM substrates using an AJA International, Inc. (Scituate, MA) ORION 4 sputtering system with a sputter-down configuration. Prior to coating, the alumina was heat treated at 1000°C/24 h to stabilize its microstructure and to remove any binders that might be present. The Ni substrates were ground to a 1000 grit finish with SiC paper. Before deposition each substrate was ultrasonically cleaned in baths of acetone,

Table 3-1: Power settings used to deposit the $\text{Al}_{17}\text{Ni}_{28}\text{Cr}_{26}\text{Co}_{28}\text{Si}_1$ coatings.

Sputtering Target	Power (watts)
Ni	225
Co	250
Al-5Si	175
Cr	225

methanol, ethanol, and isopropanol followed by plasma cleaning to remove any surface films or impurities. In the deposition chamber, the Ni substrates were heated above the Curie temperature to 400°C and allowed to sit at temperature until base pressures of 1.0×10^{-5} mTorr or better was achieved. As high purity Ni is magnetic, this temperature was selected to minimize the effects of extra magnetic fields on coating deposition. The depositions on alumina and CMSX-4™ were done without any substrate heating. A working gas of ultrahigh purity (UHP) Ar was used to maintain a working pressure of 2.4 mTorr (0.32 Pa) during deposition.

3.3 Heat Treatment, Hardness Testing, and Oxidation Testing

Annealing studies were conducted on selected alloys and coatings to assess microstructural evolution. Prior to annealing, specimens were vacuum sealed in quartz tubes that were partially backfilled with UHP argon. This step was performed to provide a static atmosphere that would reduce the chances for unintended oxidation. For annealing, specimens were placed in a resistance furnace at temperatures of 600°C, 700°C, and/or 900°C for times varying from 0.25 to 500 h. At the end of the annealing period, the specimens were removed from the furnace and quenched in water.

Age hardening behavior was assessed via post-annealing Vickers microhardness testing. A test load of 1 kgf load was used with a hold time of 15 s. A minimum of ten measurements were made of each specimen and the average and standard deviations are reported.

Isothermal oxidation experiments were conducted in laboratory air at 1050°C for time periods ranging from 1 to 1,000 h. Specimens were placed in annealed aluminum oxide boats for insertion into the hot zone of the furnace. Most specimens were oxidized sequentially by removing them from the furnace at regular intervals and allowing them to air cool to room

temperature. At this point the specimens (inside of the alumina boats) were weighed prior to returning them to the furnace.

3.4 Microstructural Characterization

Phase identification and microstructural evaluations were accomplished via X-ray diffraction (XRD), scanning electron microscopy (SEM), and transmission electron microscopy (TEM). Phase chemistries were assessed using energy dispersive X-ray spectroscopy (EDS) and atom probe tomography (APT). Specimens for TEM and APT were produced via in-situ focused-ion-beam (FIB) lift out techniques in a Quanta 200 3D dual-beam FIB [47,48]. XRD measurements were done after each heat treatment and oxidation step using a Philips X'Pert MPD XRD system with a Cu source. Cross sectional images were collected using a JEOL 7000F SEM in the backscattered mode. Brightfield images, selected area electron diffraction (SAED) patterns, and high angle annular dark field (HAADF) images were captured on a 200keV FEI Technai G² F-20 Supertwin (scanning) transmission electron microscope ((S)TEM).

Atom probe tomography was conducted in a Cameca LEAP[®] 3000XSi local electrode atom probe in the laser pulsed mode. The experimental data were collected using a pulse repetition rate of 200 kHz, a pulse energy of 0.2 nJ, a temperature of 30K, and an evaporation rate of 0.5%. The APT data was analyzed using Cameca's IVAS[™] 3.4 software package. Clearly visible atom-enriched regions were defined by isoconcentration surfaces [49]. Based upon these surfaces, proximity histograms (proxigrams) were calculated to obtain chemical compositions within the regions of interest [50].

4. $\text{Al}_{20}\text{Ni}_{25}\text{Cr}_{25}\text{Co}_{25}\text{Si}_5$ ALLOY

4.1 Alloy Design and Crystal Structures

The majority of the work on HEAs has focused on alloys containing Al, Cr, Fe, Co, Cu, and Ni, along with other transition metal additions. In high temperature environments some elements, such as Cu and Fe, are undesirable as they can contribute towards reduced high-temperature capabilities [51,52]. Thus, our approach was to design an alloy that contained Al, Co, Cr, and Ni as primary constituents, which would be capable of forming an aluminum oxide scale when exposed to oxidizing conditions. A fifth element, Si, was also added based upon its well-known influences on the oxidation and hot corrosion resistance of superalloys and their protective coatings [6,52]. In addition, enhanced hardenability, wear resistance and oxidation resistance has been reported in Si-containing multi-principal-element HEAs and HEA coatings [15,17]. Using the atomic radii values published in reference [53], values of $\delta = 6.13\%$, $\Delta H_{\max} = 12.57 \text{ J/K}\cdot\text{mol}$, $\Delta S_{\max} = -18.72 \text{ kJ/mol}$, and $\Omega \approx 1.14$ were determined for the alloy which should, based upon the phase selection rules proposed by Yang and Zhang [7,20], yield an alloy consisting of a mixture of solid solution and intermetallic phases.

4.2 Microstructure of the As-Cast Alloy

Microstructural characterization was performed via XRD, SEM and TEM revealing the presence of at least six distinct phases in the studied alloy. The chemical compositions of the alloy and phases were determined via EDS and APT. The lattice parameters for the observed phases were determined via XRD and SAED. Both are summarized in Table 4-1 and will be

discussed below. The large variability between the atom probe and TEM EDS compositions are the result of TEM EDS collecting compositions from both the matrix and precipitates. The electron beam within TEM EDS travels a certain depth into a given material. Because of the thinness of the precipitates the electrons often travel through a given precipitate and is reflected back to the detector within the matrix. The collection of this spectrum results in a skewing of the precipitate composition. Atom probe concentrations provide a more accurate composition based on its ability to separate the precipitate and matrix.

Fig. 4-1 shows representative XRD patterns from the alloy in the as-cast and annealed conditions. The patterns indicate the presence of two phases: (1) an ordered B2 phase which based on peak intensities represented the majority phase and (2) a body-centered tetragonal σ phase ($D8_b$ -type crystal structure). Similar observations have been reported in a number of AlCrFeNi-based HEAs, with the structure of the second phase being dependent upon alloy composition [17,38,54-56].

Fig. 4-2(a) shows a representative SEM backscattered electron image collected from the as-cast alloy. The as-cast alloy consisted of coarse low atomic number contrast (i.e., Z-contrast) dendrites (labeled D) surrounded by higher Z-contrast interdendritic regions (labeled ID). A small number of black oxide inclusions were also observed in the interdendritic regions. The presence of these particles, which constituted less than 2% of the alloy microstructure, was traced to some of the raw materials that were used to produce the alloy. No additional evidence of oxygen contamination was detected within the alloy. Relative to the bulk alloy composition, EDS analysis (Table 4-1) showed the dendrites to be rich in Ni and Al whereas the interdendritic regions were richer in Cr and Co.

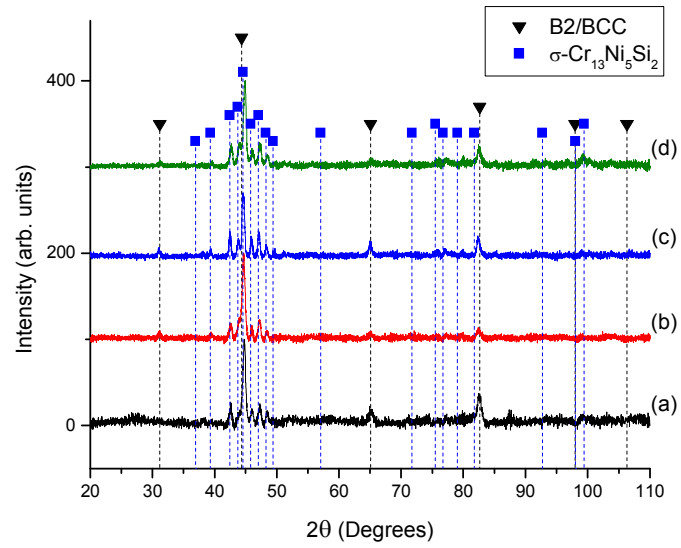


Figure 4-1: XRD patterns for $\text{Al}_{20}\text{Cr}_{25}\text{Co}_{25}\text{Ni}_{25}\text{Si}_5$ in the as-cast and annealed conditions. (a) As-cast, (b) annealed at $700^\circ\text{C}/5\text{ h}$, (c) annealed at $700^\circ\text{C}/1000\text{ h}$, and (d) annealed at $900^\circ\text{C}/100\text{ h}$.

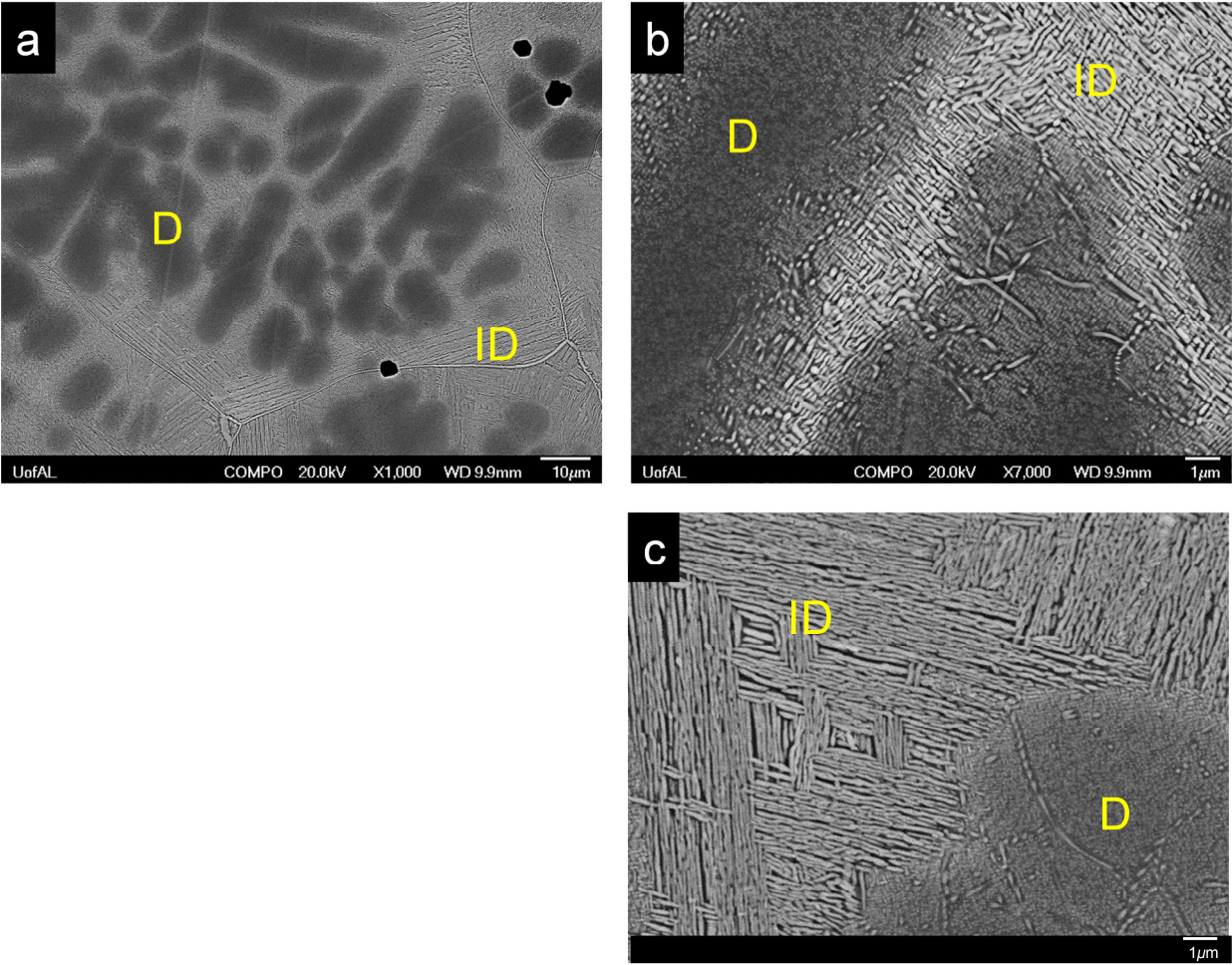


Figure 4-2: SEM backscattered electron images of the $\text{Al}_{20}\text{Cr}_{25}\text{Co}_{25}\text{Ni}_{25}\text{Si}_5$ alloy in the as-cast state. (a) Low magnification; (b) and (c) high magnification.

Table 4-1: Chemical compositions and lattice parameters for the phases observed in the $\text{Al}_{20}\text{Cr}_{25}\text{Co}_{25}\text{Ni}_{25}\text{Si}_5$ alloy in the as-cast state.

CHEMICAL COMPOSITION (at.%)						
Collection Method	Zone/phase	Al	Co	Cr	Ni	Si
	Nominal	20.00	25.00	25.00	25.00	5.00
SEM-EDS	Overall	19.83 ± 0.50	24.33 ± 0.46	25.59 ± 0.20	24.30 ± 0.40	5.95 ± 0.26
SEM-EDS	D / overall	22.12 ± 0.10	24.58 ± 0.16	23.97 ± 0.13	25.06 ± 0.17	4.28 ± 0.06
TEM-EDS	D / B2	21.40 ± 0.14	25.04 ± 0.27	10.18 ± 0.15	39.31 ± 0.49	3.31 ± 0.06
TEM-EDS	D / BCC	11.66 ± 0.09	31.12 ± 0.23	34.76 ± 0.21	25.40 ± 0.20	4.72 ± 0.06
APT	D / B2	27.34 ± 0.08	23.23 ± 0.08	11.59 ± 0.05	34.26 ± 0.09	3.58 ± 0.01
APT	D / BCC	14.56 ± 0.06	22.78 ± 0.08	36.65 ± 0.09	22.71 ± 0.07	3.32 ± 0.01
SEM-EDS	ID / overall	8.51 ± 0.07	26.37 ± 0.16	35.92 ± 0.15	20.27 ± 0.16	8.93 ± 0.07
TEM-EDS	ID / B2	21.77 ± 0.22	25.04 ± 0.40	12.89 ± 0.25	36.97 ± 0.49	3.33 ± 0.09
TEM-EDS	ID / σ	1.93 ± 0.06	28.47 ± 0.39	53.05 ± 0.44	9.36 ± 0.23	7.18 ± 0.11
LATTICE PARAMETERS (Å)						
TEM	BCC	a=2.936 ± 0.057				
TEM	B2	a=2.902 ± 0.049				
TEM	σ	a=8.958 ± 0.067 , c=4.514 ± 0.053				

ID = interdendritic region ; D = dendritic region

Higher magnification images, presented in Figs. 4-2(b) and 4-2(c), revealed fine multiphase microstructures in both regions. The dendritic regions were composed of a large volume fraction of high Z-contrast precipitates dispersed in a lower Z-contrast matrix. Conversely, the interdendritic regions were primarily composed of interconnected high Z-contrast lamellae interspersed with a lower Z-contrast phase. The lamellae were arranged either in modulated net-like structures or in packets consisting of long interweaving side plates that often emanated from grain boundaries. The side plates were reminiscent of the Widmanstätten structures commonly observed in Ti-based alloys and steels [57]. In the interdendritic regions, many of the grain boundaries were decorated with a semi-continuous high Z-contrast phase. The interconnected natures of these microstructures can be seen more clearly in the mosaic STEM-HAADF image presented in Fig. 4-3.

The low Z-contrast matrix phase in the dendritic regions and the low Z-contrast phase in the interdendritic regions were found to be rich in Ni and Al, with nearly identical compositions. Conversely, the higher Z-contrast phases in each region were richer in Co and Cr, and leaner in Al. Fig. 4-4 shows a representative bright-field TEM image along with SAED patterns collected from the two phases observed in the dendritic region (i.e., region D). From the patterns, it was determined that the precipitates had a disordered BCC crystal structure and that they were dispersed in an ordered B2 matrix. The matrix and precipitate phases also had nearly identical lattice parameters (i.e., $a_{B2} = 2.936 \pm 0.057 \text{ \AA}$ and $a_{BCC} = 2.903 \pm 0.035 \text{ \AA}$ respectively) and were fully coherent exhibiting a cube-on-cube orientation relationship (i.e., $\langle 001 \rangle_{B2} // \langle 001 \rangle_{BCC}$).

The dendritic region was further investigated by APT. Fig. 4-5 shows a three-dimensional reconstruction of the dendritic region with accompanying compositional data in

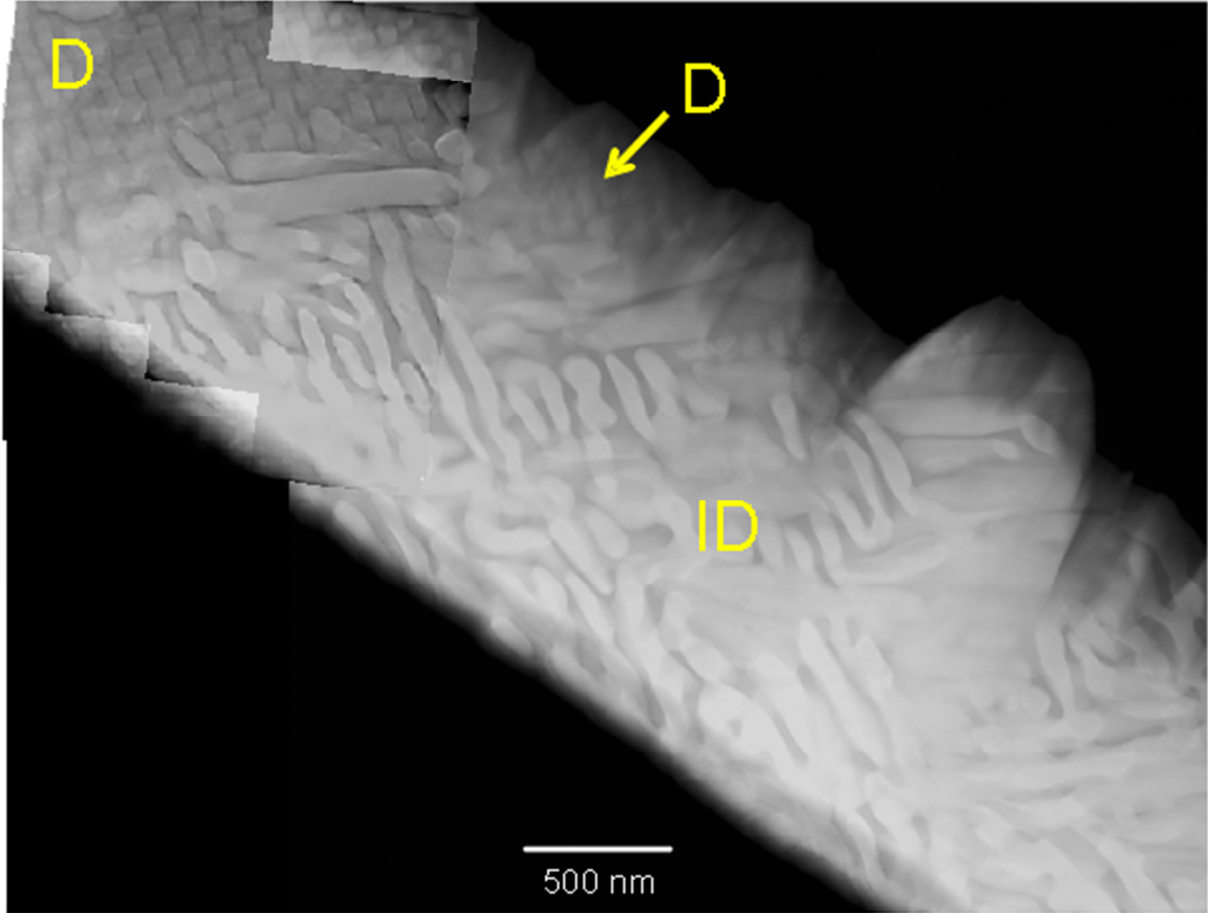


Figure 4-3: Mosaic STEM-HAADF image illustrating the morphological differences observed in the dendritic and interdendritic regions of the cast alloy. Note the presence of high atomic number contrast platelets in the dendritic regions and interconnected high atomic number contrast strands within the interdendritic regions.

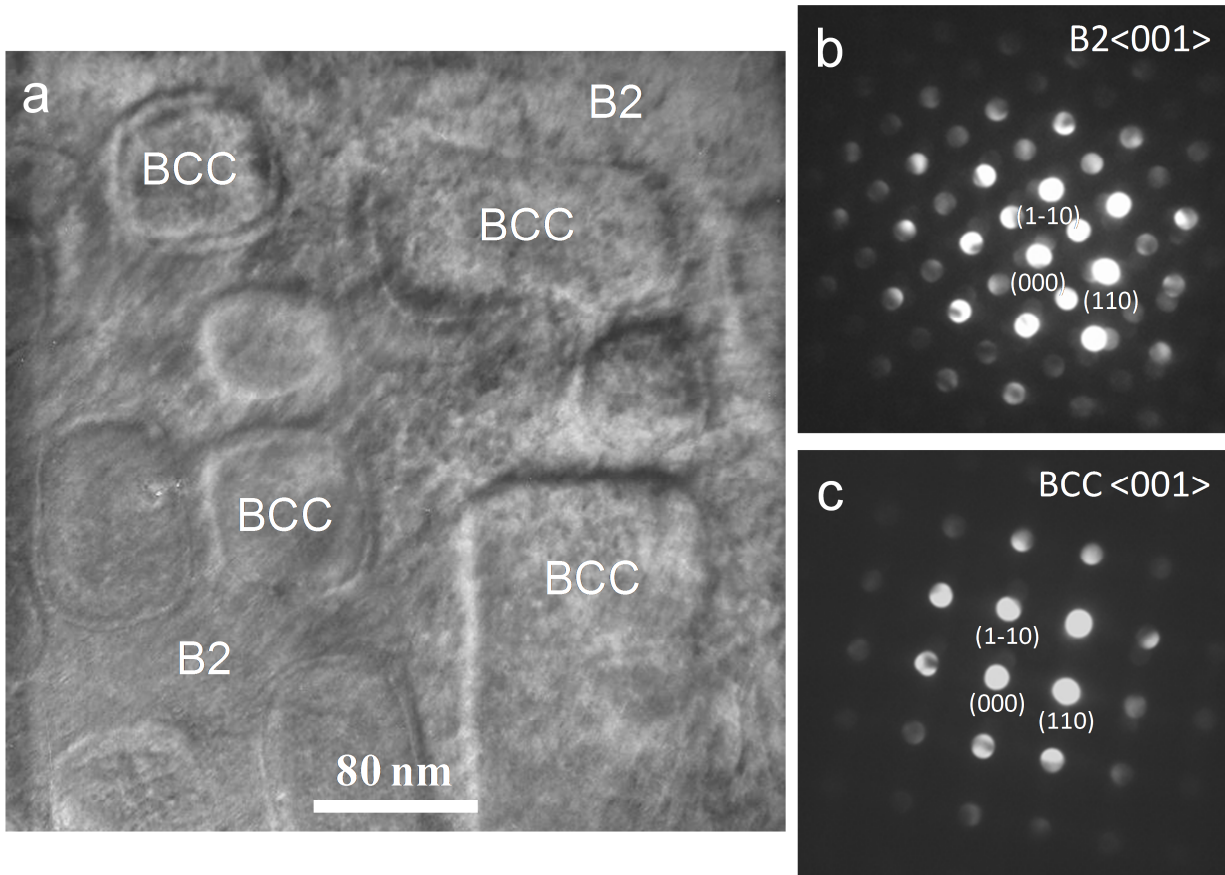


Figure 4-4: Brightfield TEM micrographs and SAED patterns collected from zone A of the as-cast alloy. (a) The dendritic region showing disordered BCC precipitates in an ordered B2 matrix. (b) SAED pattern of the $\langle 001 \rangle_{B2}$ zone axis. (c) SAED pattern of the $\langle 001 \rangle_{BCC}$ zone axis.

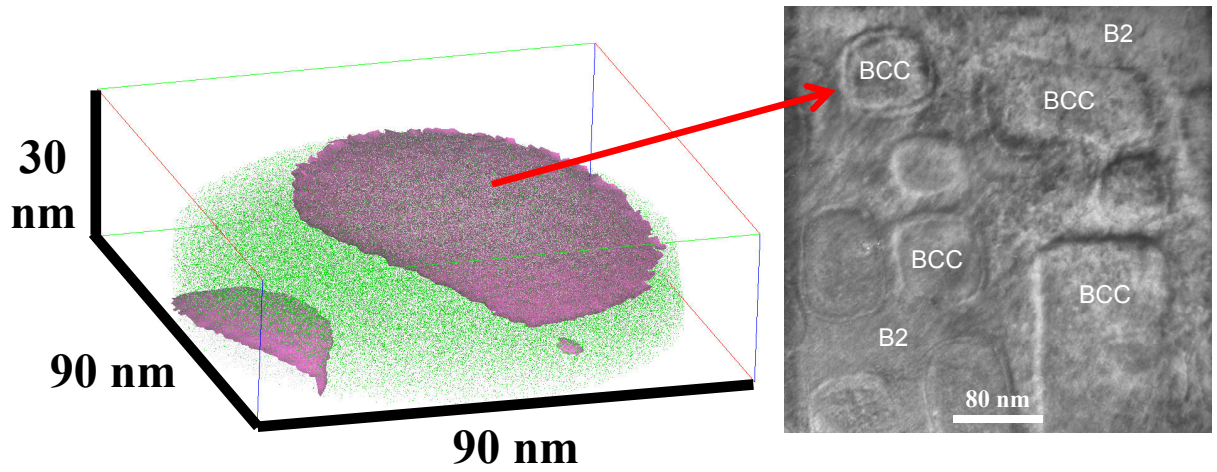


Figure 4-5: Atom probe reconstruction of precipitates observed for the as-cast alloy with corresponding TEM bright field image.

Table 4-1. Precipitates with plate like morphologies, similar to those observed in the TEM, were observed. These precipitates were found to have higher concentrations of Cr, Co, and Ni than the surrounding matrix phase. Based upon the phase compositions and the TEM results, these precipitates are believed to be a supersaturated α -Cr. This hypothesis is based upon the fact that the lattice parameter for this was found to be nearly identical to that of α -Cr. It is additionally noted that α -Cr exhibits a high solubility for Ni and Co at elevated temperatures [58].

Fig. 4-6 shows a bright-field TEM image and SAED patterns collected from the two phases observed in the interdendritic region. This region was composed of interconnected σ -phase lamellae interspersed with a semi-continuous ordered B2 phase. The σ -phase was richer in Co, Cr and Si, but was severely depleted in Ni and Al. The B2 phase was richer in Ni and Al and had nearly the same composition as the matrix phase in the dendritic region. Similar multiphase microstructures and chemical distributions have been reported for a number of multicomponent HEA systems and have been attributed to a combination of eutectic and spinodal type decomposition reactions [30,32,37,39,45,59-69].

4.3 Influences of Annealing

Annealing caused significant changes in the microstructures, phase compositions, and hardness of the alloy. Figs. 4-7(a) and 4-7(b) show representative backscattered SEM images of the alloy after aging at 700°C/5 h. The alloy appeared to maintain its dendritic microstructure; however, this was accompanied by noticeable microstructural coarsening and by the formation of small needle-like precipitates.

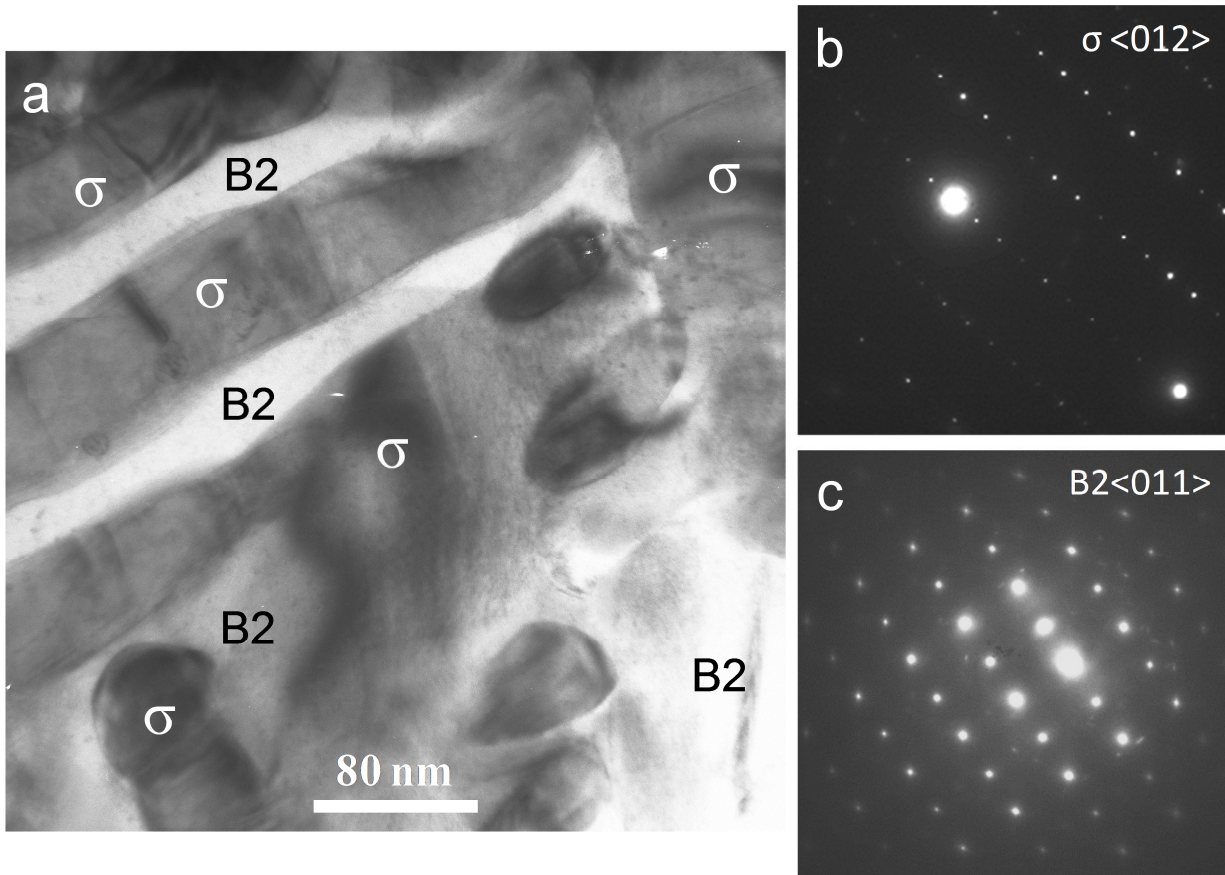


Figure 4-6: Brightfield TEM micrographs and SAED patterns collected from zone B of the as-cast alloy. (a) The interdentritic region showing σ phase precipitates in an ordered B2 matrix. (b) SAED pattern of the $\langle 012 \rangle_{\sigma}$ zone axis. (c) SAED pattern of the $\langle 011 \rangle_{B2}$ zone axis.

Fig. 4-8 shows a bright-field TEM image, a STEM-HAADF image, and SAED patterns collected from alloy after aging at 700°C/5 h. The TEM foil was prepared from the dendritic region of the specimen using an FIB microscope. Using SAED, four distinct phases were identified: a B2 matrix phase, elongated σ -phase lamellae, heavily faceted χ -phase precipitates, and short γ -FCC needles. The χ -phase was found to be fully coherent with the B2 phase, exhibiting a cube-on-cube orientation relationship as is shown in Fig. 4-7(d), and had a lattice parameter that was approximately three times that of the B2 matrix phase (i.e., 8.745 Å versus 2.936 Å).

Atom probe tips were prepared from the dendritic region to determine the compositions of the phases observed in the TEM and to look for instances of elemental segregation or elemental clustering that might not be observable in the TEM. The results, some of which are presented in Fig. 4-9, confirmed the presence of a B2 matrix that contained χ , σ , and FCC precipitates. A comparison of phase compositions as determined via TEM EDS and APT are presented in Table 4-2.

Figs. 4-7(c) and 4-7(d) show backscattered SEM images of the alloy after aging at 700°C/1000 h. As was the case after 5 h of annealing, the dendritic microstructure was retained. However, additional microstructural coarsening was observed throughout the alloy. TEM analysis (Fig. 4-10) revealed the presence of two different σ phases based on chemical composition. The long strands, labeled “A”, correspond to a σ phase more rich in Al and Ni, while the nodule-like precipitates, labeled “B”, correspond to a σ phase that is highly depleted in Al, yet very rich in Cr. Accordingly, a slight difference in lattice parameters was observed, as shown indicated Table 4-2, which can be attributed to the observed compositional variations.

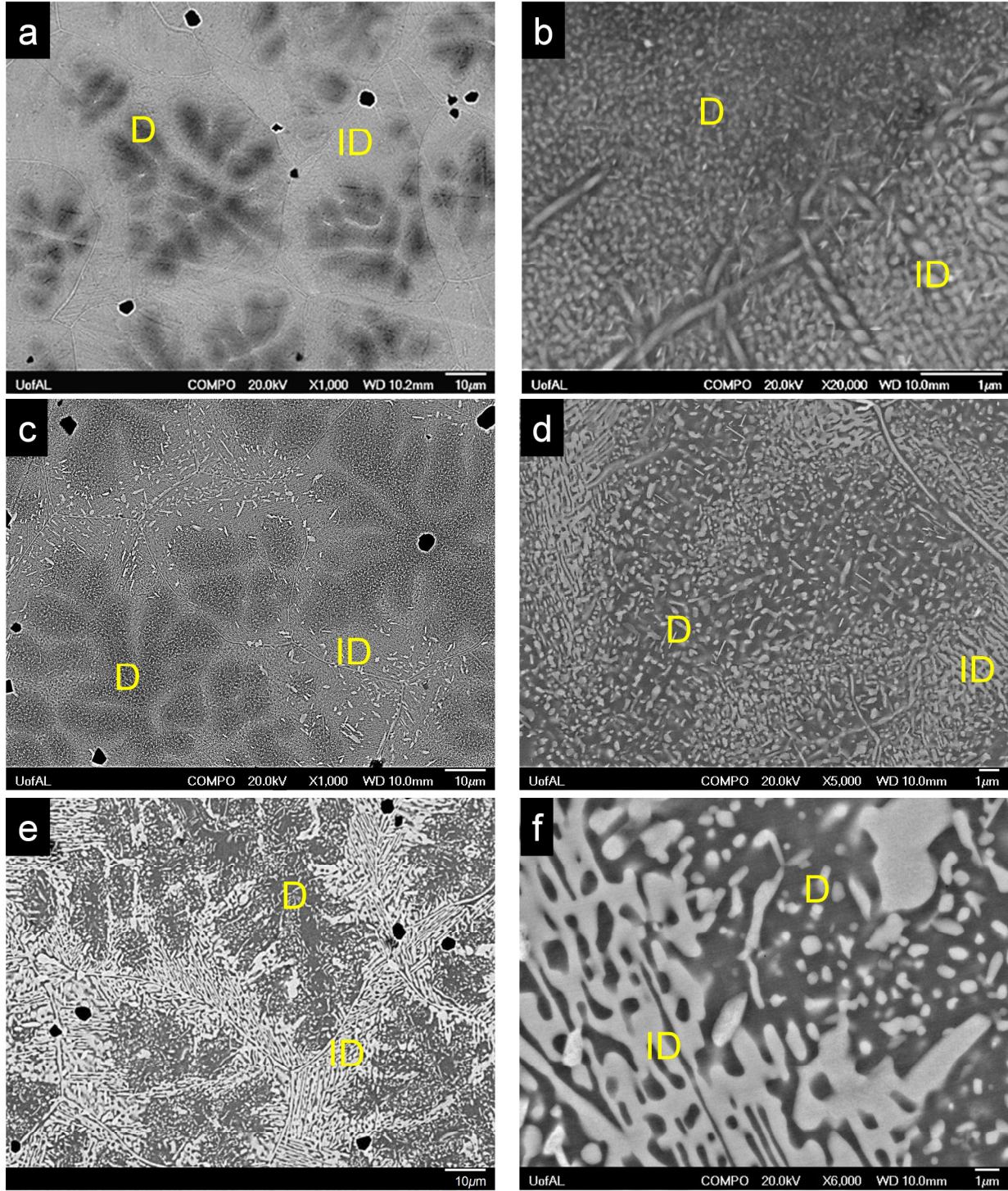


Figure 4-7: SEM backscattered electron images of the $\text{Al}_{20}\text{Cr}_{25}\text{Co}_{25}\text{Ni}_{25}\text{Si}_5$ alloy after annealing. (a and b) Annealed at 700°C/5 h. (c and d) Annealed at 700°C/1000 h. (e and f) Annealed at 1000°C/100 h.

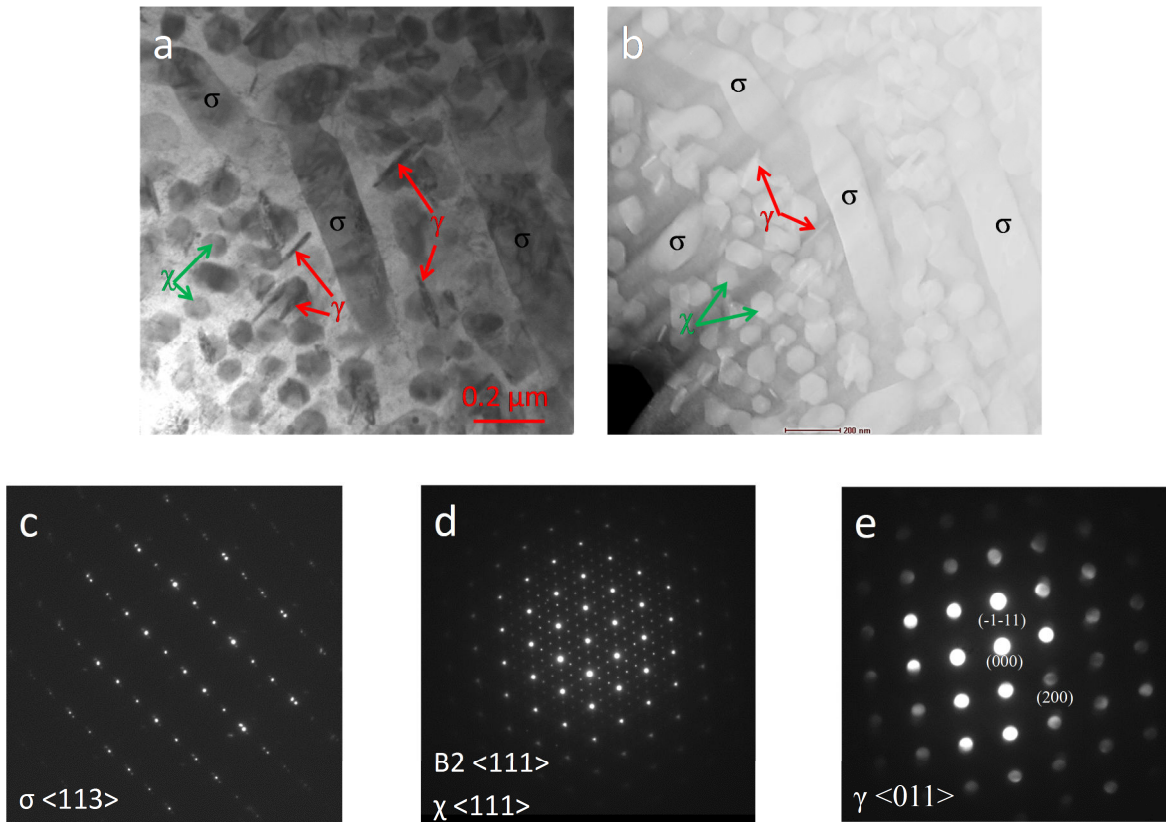


Figure 4-8: TEM results after aging at 700°C for 5 h. (a) Bright-field image; (b) STEM-HAADF image; (c) SAED pattern collected from the σ -phase; (d) SAED pattern collected from the χ -phase illustrating coherency with the B2 matrix; and (e) SAED pattern collected from the needles indicating a disordered FCC crystal structure.

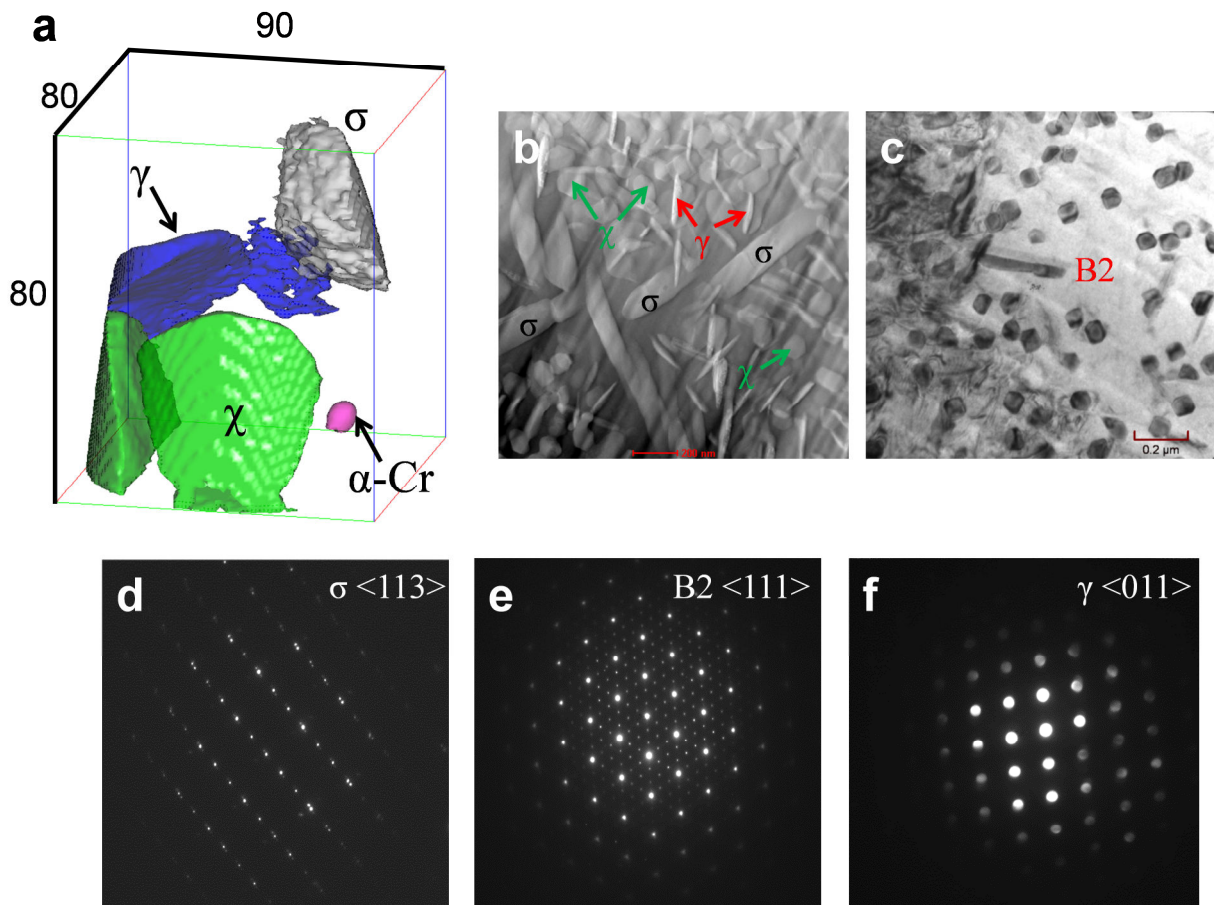


Figure 4-9: (a) Atom probe reconstruction of precipitates observed after aging at 700°C for 5 h. (b) Bright-field image; (c) STEM-HAADF image; (d) SAED pattern collected from the σ -phase; (e) SAED pattern collected from the χ -phase illustrating coherency with the B2 matrix; and (f) SAED pattern collected from the needles indicating a disordered FCC crystal structure. Dimensions in (a) are in nm.

Table 4-2: Chemical compositions and lattice parameters for the phases observed in the Al₂₀Cr₂₅Co₂₅Ni₂₅Si₅ alloy after annealing at 700°C/5 hr.

CHEMICAL COMPOSITION (at.%)						
Collection Method	Zone/phase	Al	Co	Cr	Ni	Si
TEM EDS	D / B2	24.94 ± 0.13	19.99 ± 0.17	17.53 ± 0.19	35.70 ± 0.25	1.84 ± 0.04
	D / FCC	12.36 ± 0.11	39.61 ± 0.33	23.03 ± 0.22	22.38 ± 0.25	2.61 ± 0.05
	D / χ	13.76 ± 0.10	31.65 ± 0.25	23.59 ± 0.20	23.95 ± 0.22	7.06 ± 0.07
	ID / σ	2.25	30.91	48.83	10.38	7.63
	ID / B2	27.31	17.74	3.39	47.82	3.74
APT	D / B2	33.47 ± 0.02	15.67 ± 0.02	4.55 ± 0.01	43.06 ± 0.023	3.24 ± 0.012
	D / FCC	1.19 ± 0.025	42.98 ± 0.103	30.52 ± 0.102	22.79 ± 0.086	2.52 ± 0.043
	D / χ	0.58 ± 0.015	26.31 ± 0.083	34.18 ± 0.010	29.04 ± 0.095	9.90 ± 0.076
	D / σ	2.00 ± 0.013	35.80 ± 0.045	39.68 ± 0.045	10.57 ± 0.028	11.95 ± 0.031
SEM-EDS for all	D \ B2	29.70 ± 1.72	20.99 ± 0.96	14.16 ± 1.53	32.13 ± 1.32	2.99 ± 0.56
	D \ σ	13.77 ± 1.84	25.67 ± 0.57	33.74 ± 1.21	19.58 ± 0.45	7.24 ± 0.65
	D \ FCC (needles)	7.68 ± 2.52	38.78 ± 1.44	25.49 ± 1.75	22.00 ± 0.66	6.05 ± 0.37
TEM-EDS	B2	34.75 ± 0.13	17.83 ± 0.17	2.28 ± 0.05	44.19 ± 0.26	0.93 ± 0.02
	ID \ σ (strands)	9.98 ± 0.05	28.60 ± 0.16	36.45 ± 0.15	20.24 ± 0.13	5.50 ± 0.04
	ID \ σ (nodule)	0.77 ± 0.01	33.54 ± 0.19	52.89 ± 0.22	4.77 ± 0.07	8.00 ± 0.05
LATTICE PARAMETERS (Å)						
TEM	B2	a=2.903 ± 0.035				
TEM	FCC	a = 3.54 ± 0.021				
TEM	χ	a= 8.745 ± 0.078				
TEM	σ (strands)	a= 8.625 ± 0.027 , c= 4.672 ± 0.038				
TEM	σ (nodule)	a= 8.951 ± 0.052 , c= 4.522 ± 0.066				

ID = interdendritic region; D = dendritic region

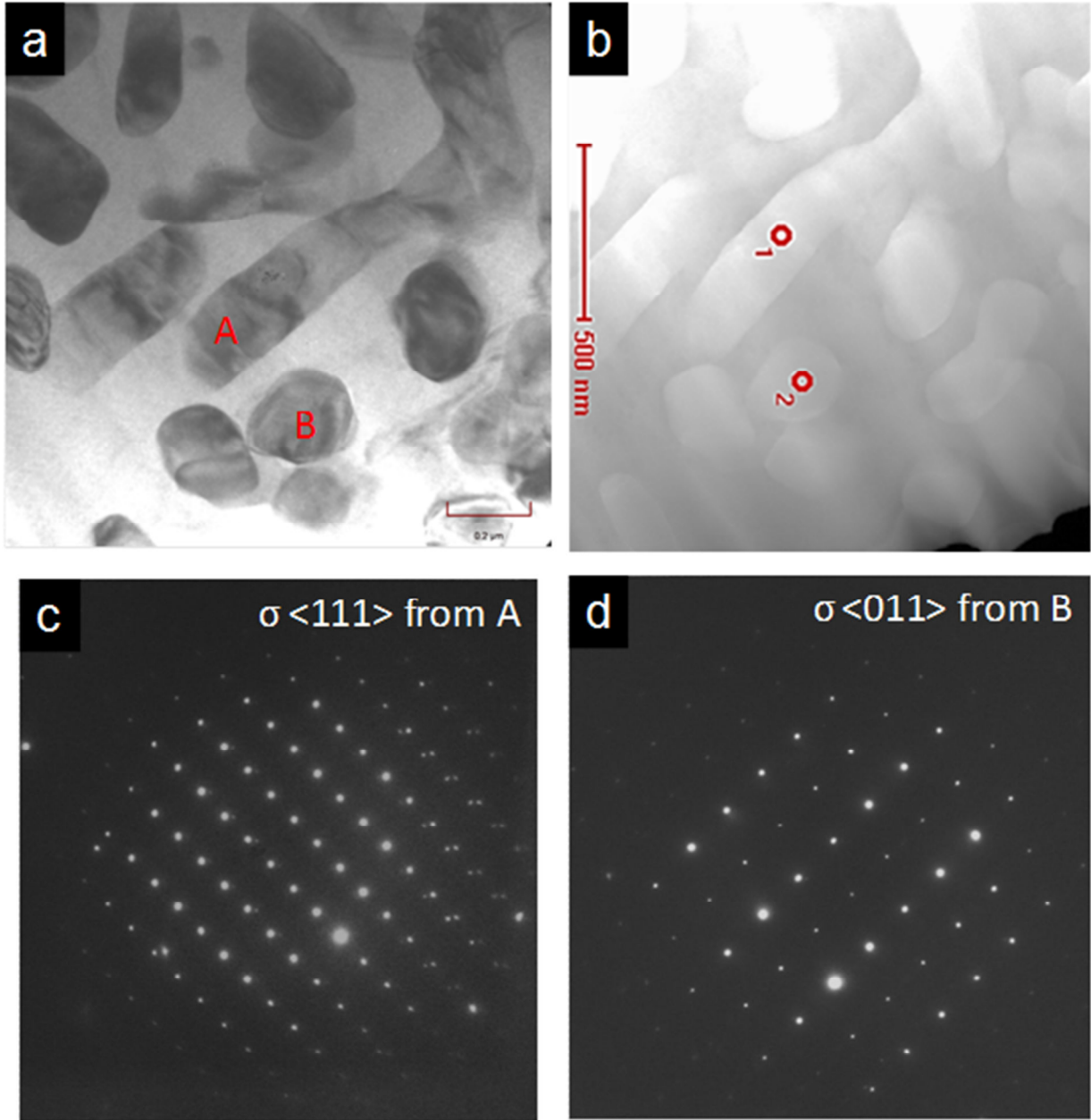


Figure 4-10: TEM results after aging at 700°C for 1000 h. (a) Bright-field image; (b) STEM-HAADF image; (c) SAED pattern collected from the σ -phase.

Table 4-3: Chemical compositions and lattice parameters for the phases observed in the $\text{Al}_{20}\text{Cr}_{25}\text{Co}_{25}\text{Ni}_{25}\text{Si}_5$ alloy after annealing at $900^\circ\text{C}/100$ h.

CHEMICAL COMPOSITION (at.%)						
Collection Method	Zone/phase	Al	Co	Cr	Ni	Si
SEM – EDS	ID / B2 matrix	30.49	20.94	10.06	35.06	3.44
	ID / σ	6.68	37.28	29.04	20.98	6.68
	ID / σ (on GBs)	4.51	29.93	43.87	13.12	8.57
	D / B2 matrix	31.18	20.35	8.61	36.45	3.41
	ID / σ (coarse)	3.63	29.27	46.26	11.99	8.86
	D / σ (nodules)	10.23	27.38	37.30	17.19	7.91
LATTICE PARAMETERS (Å)						
TEM	B2	$a = 2.873 \pm 0.027$				
TEM	σ (coarse)	$a = 8.679 \pm 0.016$, $b = 4.597 \pm 0.027$				
TEM	σ (nodule)	$a = 8.671 \pm 0.024$, $b = 4.641 \pm 0.038$				

ID = interdendritic region; D = dendritic region

Figs. 4-7(e) and 4-7(f) show backscattered SEM images of the alloy after 900°C/100 h of aging. Phase compositions for this aging condition are summarized in Table 4-3. Significant microstructural coarsening occurred, resulting in a microstructure consisting of large high Z-contrast precipitates dispersed in a low Z-contrast matrix. Using SAED in the TEM (Fig. 4-11), the two phases were identified as σ and B2. At this length scale of investigation, the microstructure was found to be similar to the one observed after aging at 700°C/1000 h.

The BCC precipitate phases observed in the dendritic regions transformed from disordered BCC to body centered tetragonal σ via an intermediate cubic χ phase. This phase transformation occurred as a direct result of diffusion within the region. The disordered BCC precipitates are believed to be a metastable α -Cr that is supersaturated in Ni and Co. It is hypothesized that this phase forms as a result of the B2 matrix phase having a limited solid solubility for Cr. This results in the rejection of Cr and in the formation of BCC precipitates that are rich in Cr. This hypothesis is supported by prior investigations of the ternary Al-Cr-Ni alloy system which show equilibrium between the B2 and disordered BCC phases [70-73]. The supersaturation with Ni and Co is a direct result of the slow diffusion kinetics expected in the investigated five component alloy system. During the early stages of annealing, the B2 matrix phase continues to reject Cr to achieve equilibrium. This Cr segregates to the B2/BCC interface where it presumably nucleates χ which grows, ultimately consuming the BCC phase. Over time, continued elemental diffusion results in the consumption of χ to form equilibrium σ phase precipitates within the ordered B2 matrix.

The formation of σ phases via an intermediate χ phase has been observed in a number of austenitic, ferritic, and duplex stainless steels and in some superalloys [1,2,74-82]. Little is known about when χ -phase forms as it has been observed at varying temperatures and times, but

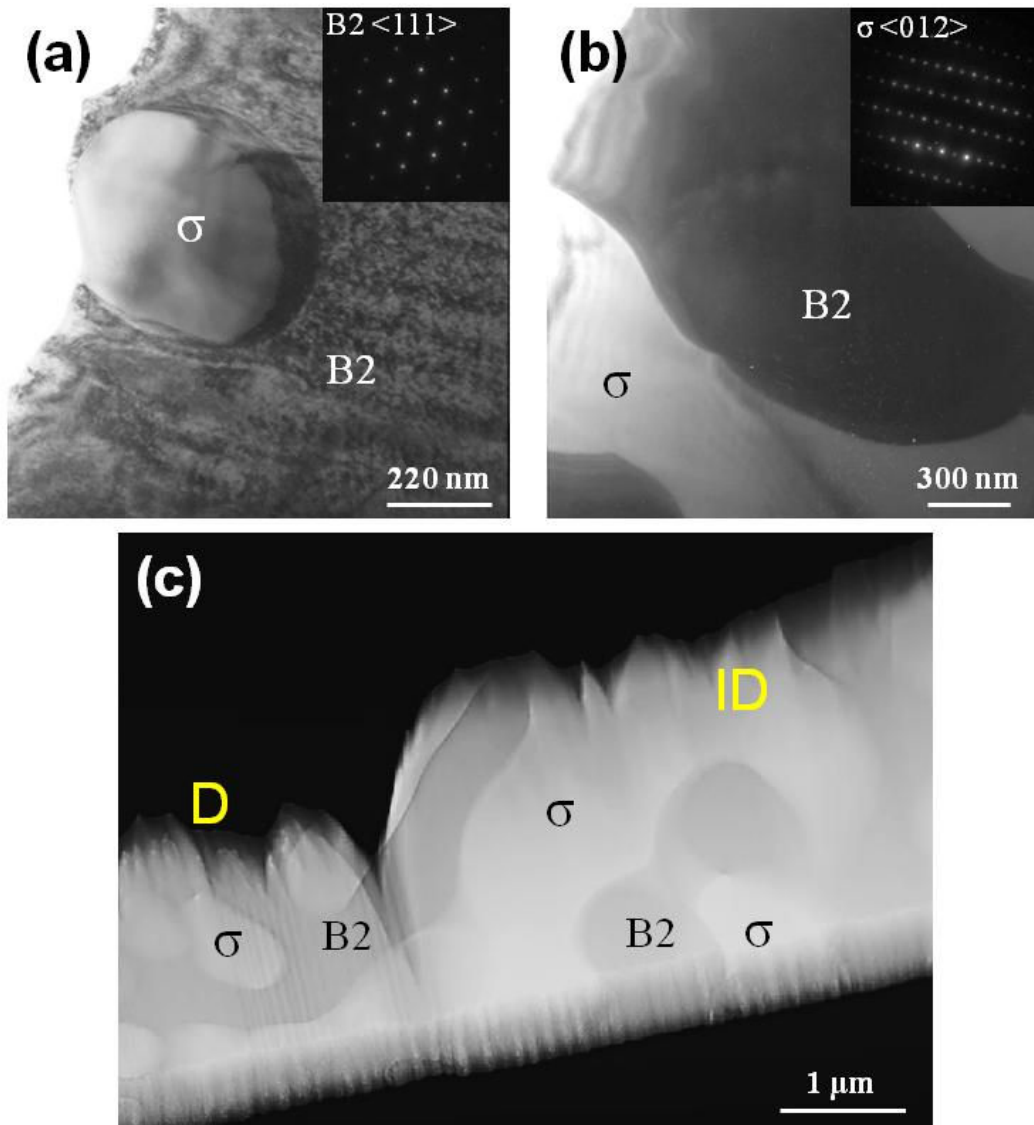


Figure 4-11: TEM results after aging at 900°C for 100 h. (a) A bright field TEM image collected from the dendritic region along with an SAED pattern for the B2 phase. (b) A bright field TEM image collected from the interdendritic region along with an SAED pattern for the σ phase. (c) A STEM-HAADF image collected from the boundary between dendritic and interdendritic regions.

it is most commonly observed during short term aging at temperatures between 700°C and 850°C. It is generally acknowledged that χ -phase is a metastable phase that can be the precursor to σ phase [78]. In steels, the χ phase has been found to nucleate at a ferrite/ferrite (i.e., BCC/BCC) interfaces and is gradually consumed to form the equilibrium σ phase. In the $\text{Al}_{20}\text{Ni}_{25}\text{Cr}_{25}\text{Co}_{25}\text{Si}_5$ alloy investigated in the present study, the nucleation point was the disordered BCC precipitates that formed during casting. With increased aging time the χ phase coexisted with σ phase before being consumed by the σ phase. This is the result of continued Cr diffusion within the alloy and χ acting as a nucleation site for σ phase [81].

Fig. 4-12 shows the hardness evolution during aging at 600°C, 700°C, and 900°C. The as-cast hardness was determined to be 865 ± 39 VHN. The alloy exhibited rapid age hardening at all three temperatures, reaching a maximum value of 1082 ± 24 VHN after 5 h at 600°C. At 700°C a peak hardness of 995 ± 32 VHN was reached after 0.5 h at 700°C. This level of hardness was maintained through 5 h of aging followed by a gradual decline to 934 ± 30 VHN after 100 h of aging. Further aging for 1000 h at 700°C resulted in a hardness of 977 ± 25 VHN, which was near the peak value for this temperature. At 900°C a peak hardness of 947 ± 30 VHN was achieved after 0.25 h of aging followed by a rapid decline to as-cast levels after 1 h of aging.

4.4 Comparison of Experimental and Computed Phase Equilibria

Phase fractions were calculated using the Thermo-CalcTM software package and are shown in Fig. 4-13. Table 4-4 shows a comparison of the experimental and calculated phases. Each of the three annealing temperatures is represented by vertical dashed lines on the plot. The phases detected experimentally at 900°C vary from those theoretically predicted. For example, Thermo-CalcTM outputs a B2 phase, a γ -FCC phase, and a disordered BCC phase.

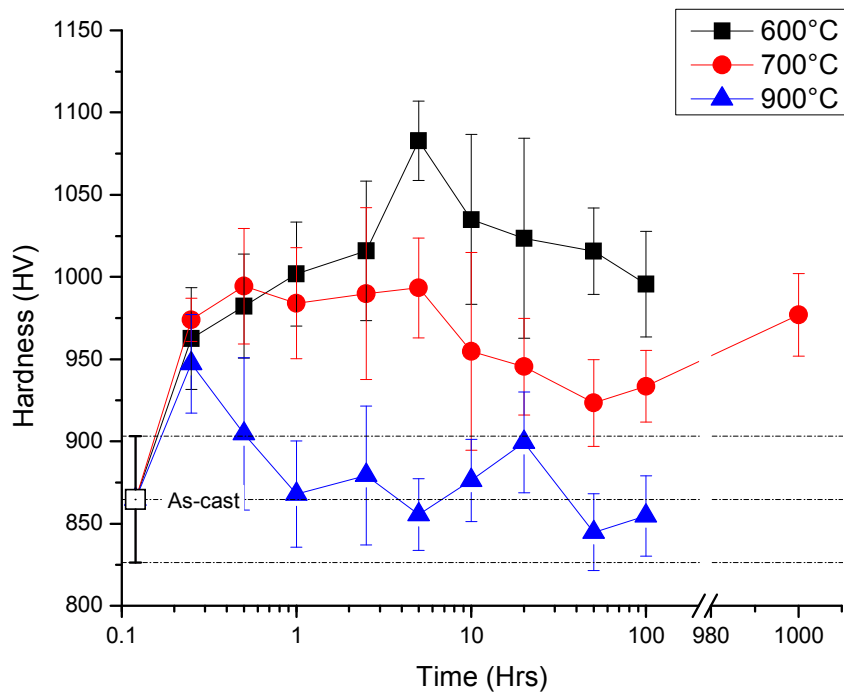


Figure 4-12: Variation in Vickers hardness with aging time for $Al_{20}Cr_{25}Co_{25}Ni_{25}Si_5$.

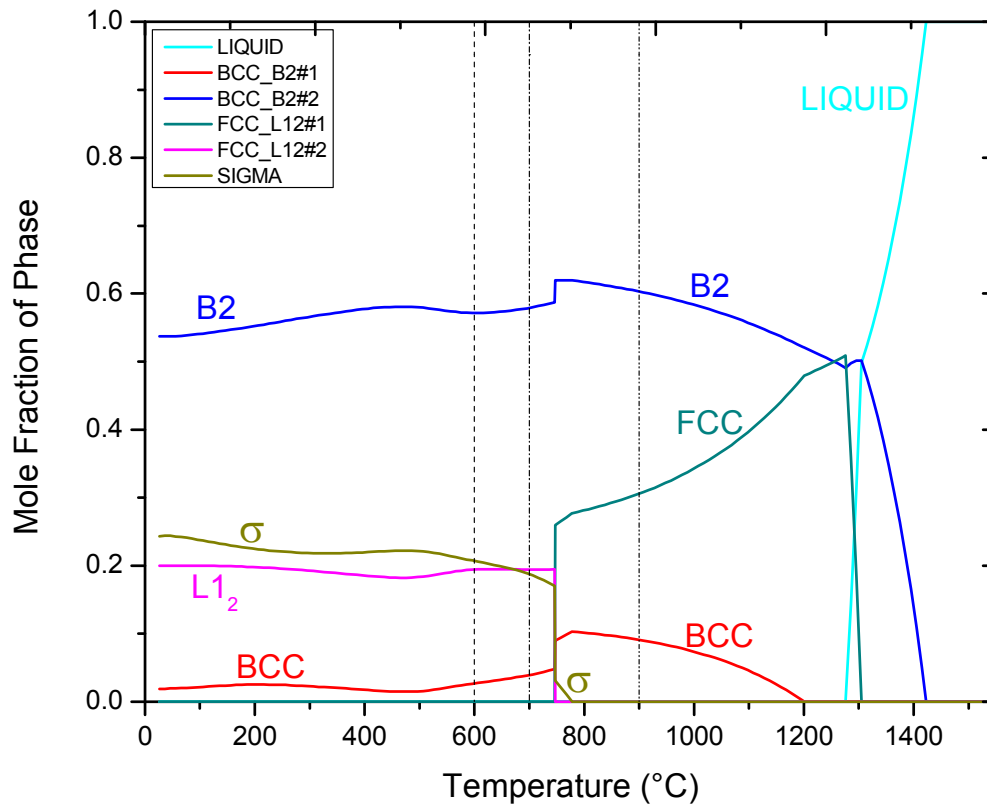


Figure 4-13: Equilibrium phase fractions (mole) as a function of temperature for the $\text{Al}_{20}\text{Cr}_{25}\text{Co}_{25}\text{Ni}_{25}\text{Si}_5$ alloy. Calculations were done using Thermo-Calc™ and the TCNI5 database.

Table 4-4: Comparison of the phases observed experimentally with those determined using Thermo-Calc™.

Temperature (°C)	Experimental	Thermo-Calc
600	B2+FCC+σ+BCC+χ	B2+σ+BCC+L1 ₂
700	B2+FCC+σ	B2+σ+BCC+L1 ₂
900	B2+FCC+σ	B2+FCC+BCC

As was previously discussed, B2, σ and χ phases were observed precipitation following short aging times at 700°C. However, when the aging time was increased, the χ -phase disappeared leaving only the B2 and σ -phases. Numerous studies of duplex stainless steels have shown that the χ -phase can form as a pre-cursor to the equilibrium σ -phase.

For the lower temperature heat treatments, the Thermo-Calc™ prediction provided closer agreement with the experimental results. The B2 and σ -phases were observed in the alloy; however no γ' phase (i.e., L1₂-FCC#2) was observed. The σ -phase fraction was also higher than that predicted by Thermo-Calc™. Similar to the 900°C results, the predicted disordered BCC phase was only observed in the as-cast alloy, but was not detected in the aged alloys (either at 600°C or 700°C). The differences between the calculated phase equilibria and the experimental results are likely due to slow diffusion kinetics coupled with the heavily cored microstructures observed in the as-cast alloy. It is believed that this combination of microstructural and physical features would delay the achievement of an equilibrium microstructure and prevent the formation of equilibrium volume fractions of phases. Similar observations have been made by Manzoni and others [30-32,83]. Thermo-Calc™ predictions are based on equilibrium conditions, and it is possible that equilibrium was never reached during heat treatment of this alloy.

One additional note can be made concerning the lack of a disordered BCC phase in the aged alloys. Previous studies by Ng *et. al.* have noted a similar discrepancy for Co containing and Co-free AlCrCuFeNi HEAs [31,83]. They suggest that the development of updated materials databases would improve available predictive capabilities.

4.5 Isothermal Oxidation Behavior

Isothermal oxidation experiments were conducted at 1050°C for times ranging from 20 to 1000 h. The results are tabulated in Table 4-5. The alloy showed little to no mass change during

Table 4-5: Isothermal oxidation results for the as-cast alloy (at.%).

Oxidation Time (Hrs)	Initial Weight (g)	Final Weight (g)	Change (g)	Surface Area (in ²)	Mass/Area (g/in ²)
20	0.1562	0.1564	0.0002	0.0615	3.252E-03
96	0.2237	0.2237	0.0000	0.0881	0.000E+00
500	0.3695	0.3696	0.0001	0.1639	6.101E-04
1000	0.2626	0.2630	0.0004	0.1326	3.017E-03

oxidation at 1050°C. Fig. 4-14 shows the resulting XRD patterns for each oxidation step. XRD revealed the presence of B2, σ , γ -FCC, and alumina phases. Fig. 4-15 shows SEM backscattered electron images of the oxidized samples. Each isothermal oxidation specimen contained two main phases: the B2 and σ -phase. Microstructural coarsening occurred with increasing oxidation time. As seen in Fig. 4-15 and Table 4-6, there is a small aluminum depleted zone below the oxide layer that contains almost equal parts Cr and Co with a high concentration of Ni. The size of the aluminum depleted zone does not vary significantly with oxidation time and from TEM analysis, this phase was found to be a γ -FCC phase, similar to NiCo with an $Fm\bar{3}m$ structure. It is important to note that this phase is seen predominately below the oxide layer. As expected, the alumina scale increases in thickness with longer oxidation time, but no internal oxidation was observed after 1000 h of oxidation.

Fig. 4-16 shows bright field TEM images and SAED patterns for specimens oxidized for 20 h and 500 h. Besides the disordered γ -FCC phase that formed just beneath the oxide scale, B2 and σ phases were identified. The diffraction patterns for the B2 phase contained some additional spots which were found to result from the presence of nano-scale Cr-rich σ precipitates within the B2 matrix. This precipitation was made more apparent through APT, some results from which are shown in Fig. 4-17 and Table 4-7. As can be seen in Fig. 4-17(a), these precipitates which were observed throughout the B2 phase had compositions that were similar to the coarse σ -phase observed in other portions of the alloy (except for an increase in Al with a decrease in Si and Co). Fig. 4-17(b) shows a reconstructed interface between the coarse σ phase and a B2 region that also contained nano-scale σ precipitates within a B2 matrix. In the region near the interface, an apparent precipitate free zone was observed. This was expected due to the low solid solubility for Cr in the B2 phase coupled with a high driving force for Cr

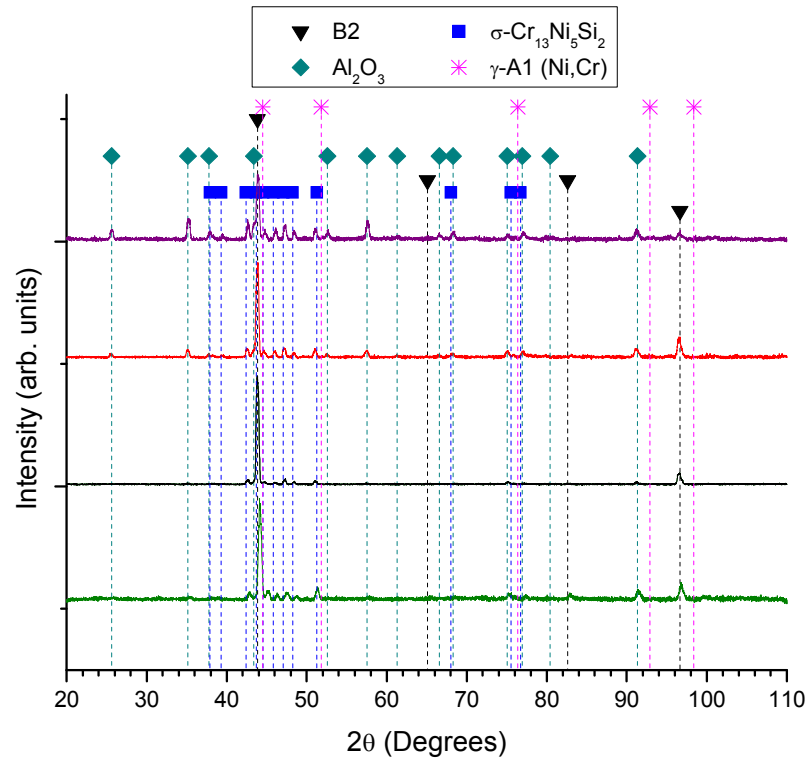


Figure 4-14: XRD patterns of the $\text{Al}_{20}\text{Cr}_{25}\text{Co}_{25}\text{Ni}_{25}\text{Si}_5$ for as-cast, 20 h, 96 h, 500 h, and 1000 h oxidized samples at 1050°C .

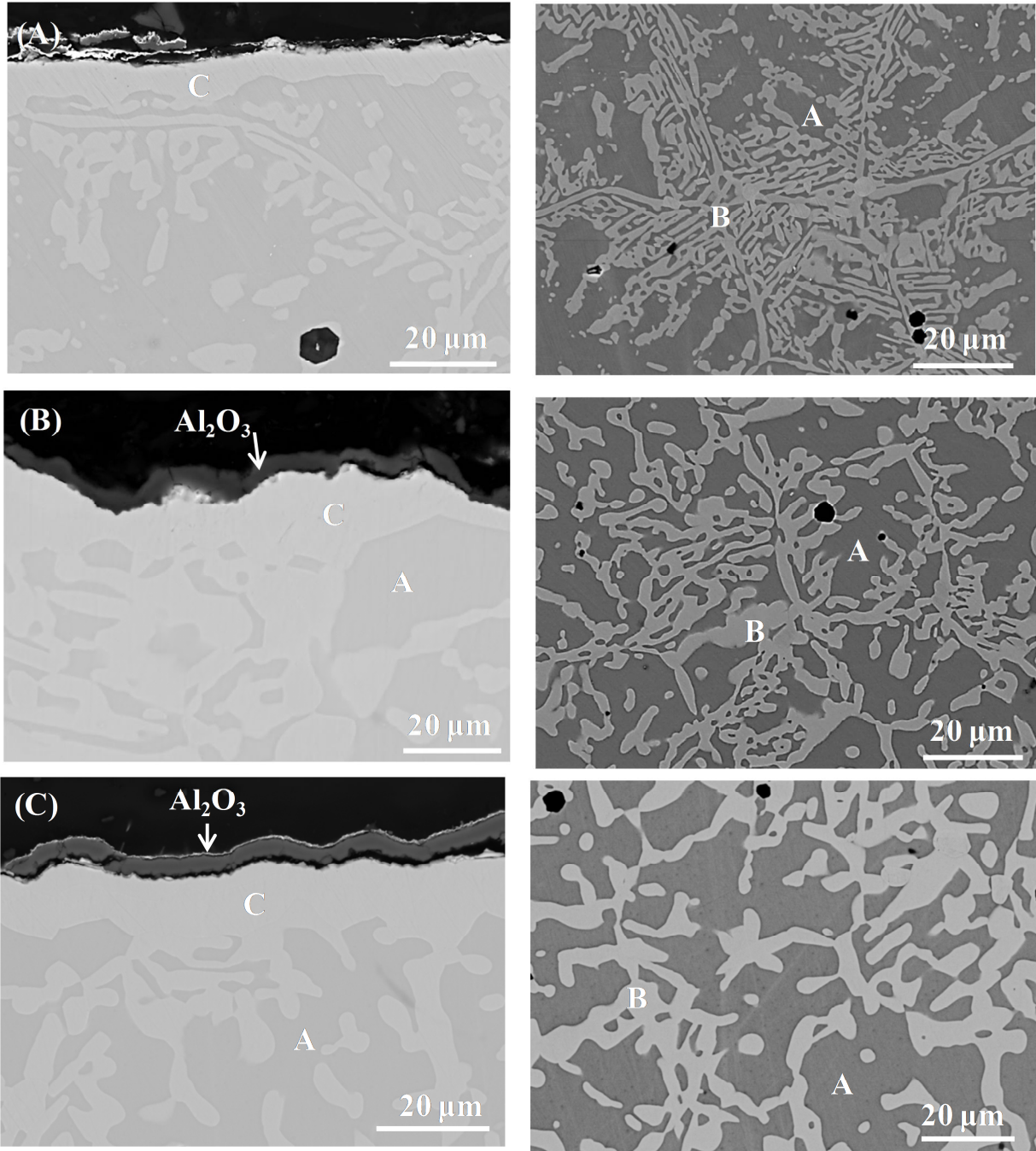


Figure 4-15: Backscattered SEM images of the oxide scale and microstructure within the alloy after (A) 20 h (B) 96 h and (C) 500 h of isothermal oxidation at 1050°C.

Table 4-6: Compositions of the three main phases observed in the oxidized samples.

20 h Oxidation			
Element	A B2 Region (Atomic %)	B σ -Region (Atomic %)	C γ -FCC (Atomic %)
Al	28.33 \pm 0.10	1.69 \pm 0.06	5.05 \pm 0.06
Si	4.17 \pm 0.07	8.83 \pm 0.06	6.01 \pm 0.06
Cr	12.05 \pm 0.09	51.02 \pm 0.15	32.08 \pm 0.13
Co	22.60 \pm 0.15	28.27 \pm 0.15	35.30 \pm 0.15
Ni	32.85 \pm 0.16	10.19 \pm 0.14	21.56 \pm 0.15
96 h Oxidation			
Element	A B2 Region (Atomic %)	B σ -Region (Atomic %)	C γ -FCC (Atomic %)
Al	28.77 \pm 0.10	1.65 \pm 0.05	5.24 \pm 0.07
Si	4.11 \pm 0.06	8.87 \pm 0.06	6.18 \pm 0.06
Cr	11.13 \pm 0.08	50.86 \pm 0.14	31.89 \pm 0.13
Co	22.60 \pm 0.15	28.41 \pm 0.15	35.48 \pm 0.15
Ni	33.39 \pm 0.15	10.21 \pm 0.14	21.20 \pm 0.15
500 h Oxidation			
Element	A B2 Region (Atomic %)	B σ -Region (Atomic %)	C γ -FCC (Atomic %)
Al	29.63 \pm 0.10	1.77 \pm 0.06	5.27 \pm 0.07
Si	4.17 \pm 0.06	9.23 \pm 0.06	6.24 \pm 0.06
Cr	10.88 \pm 0.08	51.25 \pm 0.15	32.03 \pm 0.13
Co	21.69 \pm 0.14	27.86 \pm 0.14	34.88 \pm 0.15
Ni	33.63 \pm 0.15	9.89 \pm 0.13	21.57 \pm 0.15

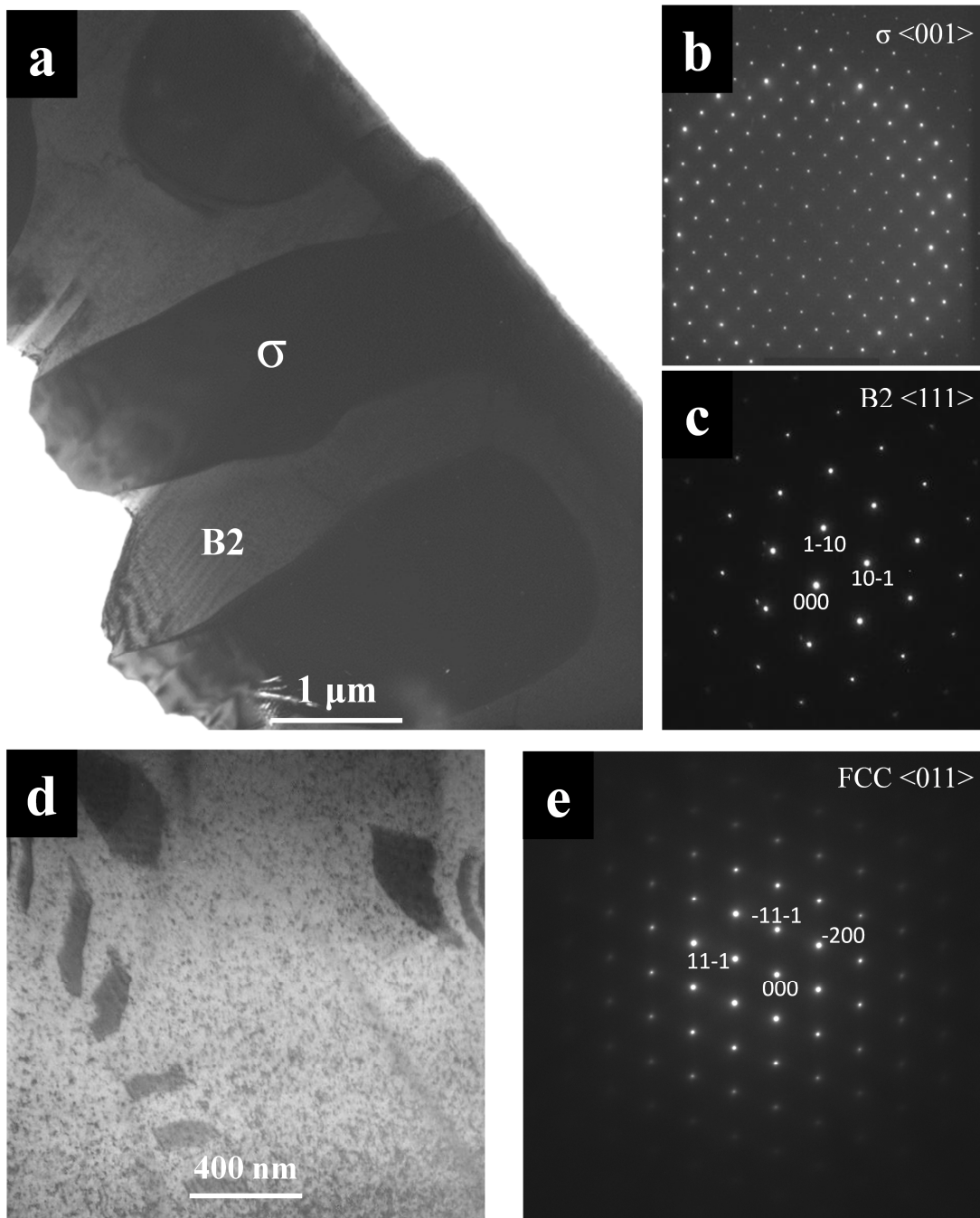


Figure 4-16: (a) Brightfield TEM image of 20 h oxidized sample with TEM diffraction for (b) σ region and (c) B2 region. (d) Brightfield TEM image of γ -FCC region with accompanying SAED pattern.

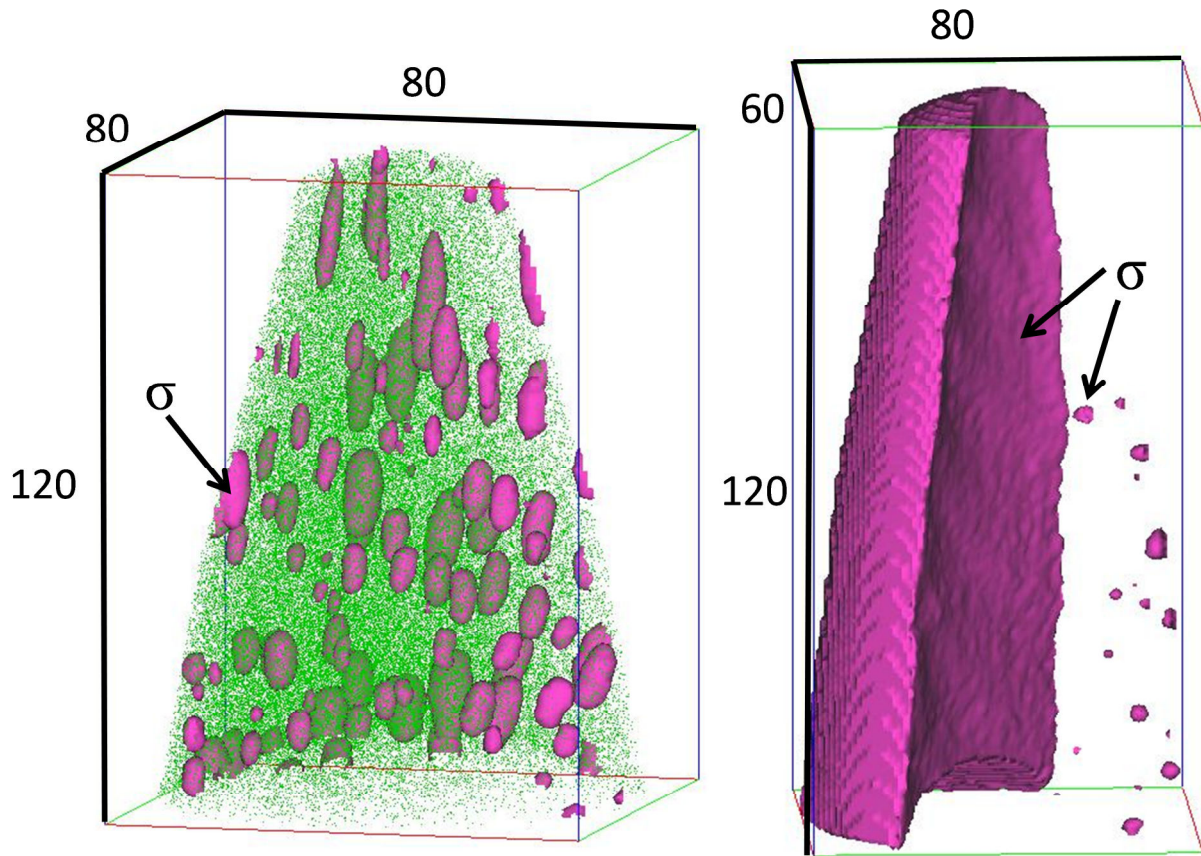


Figure 4-17: Three dimensional APT reconstructions of: (a) the B2 region revealing the presence of Cr-rich σ phase precipitates; and (b) the interface between coarse σ phase and a B2 region. Dimensions are in nm.

Table 4-7: Composition values for phases observed in atom probe analysis (at.%).

Element	σ	NiAl	Precipitation
Al	1.16	28.25	6.57
Si	8.03	3.45	4.67
Cr	47.35	9.94	53.99
Co	28.04	20.13	20.92
Ni	13.82	36.11	13.29

diffusion towards the σ phase to facilitate its growth. No nano-scale precipitation was observed within the σ phase regions.

One specimen was also sequentially oxidized for 100 h at 1050°C, but removed hourly to measure the specimen mass. Fig. 4-18 shows the specimen mass change that occurred during oxidation. A slight increase in mass is seen during initial oxidation then the mass gain curve steadys. A slight decrease in mass gain is observed at the end of the oxidation test resulting from spallation of the oxide. Microstructures and phases were investigated using SEM and XRD after 5, 10, 24, 50, and 100 h of oxidation. Fig. 4-19(a) through 4-19(d) show representative SEM images collected from the oxidized surfaces after various stages of oxidation. These surfaces were found to be composed of mixtures of chromia and alumina with the chromia apparently forming on top of an alumina layer.

The oxides appeared to be compact and dense, but contained a number of microcracks. Fig. 4-20 shows XRD patterns collected following various stages of oxidation. XRD revealed the presence of an ordered B2 phase, a σ phase, and a disordered FCC phase along with two oxides, chromia and alumina. After 100 h, the specimen was mounted and the cross section was analyzed revealing a continuous compact alumina scale below the chromia surface.

Figs. 4-19(e) and 4-19(f) show cross-sectional SEM images collected following 100 h of oxidation. Interestingly, in this specimen which was oxidized sequentially, the FCC zone was thicker and the oxide that formed on the alloy surface was found to consist of a chromia layer on top of an inner alumina layer. The increased thickness of the FCC zone is attributed to the depletion of Al from the alloy surface to form the alumina layer along with the continued diffusion of Cr to form this phase and the external chromia scale. Such a clearly observable

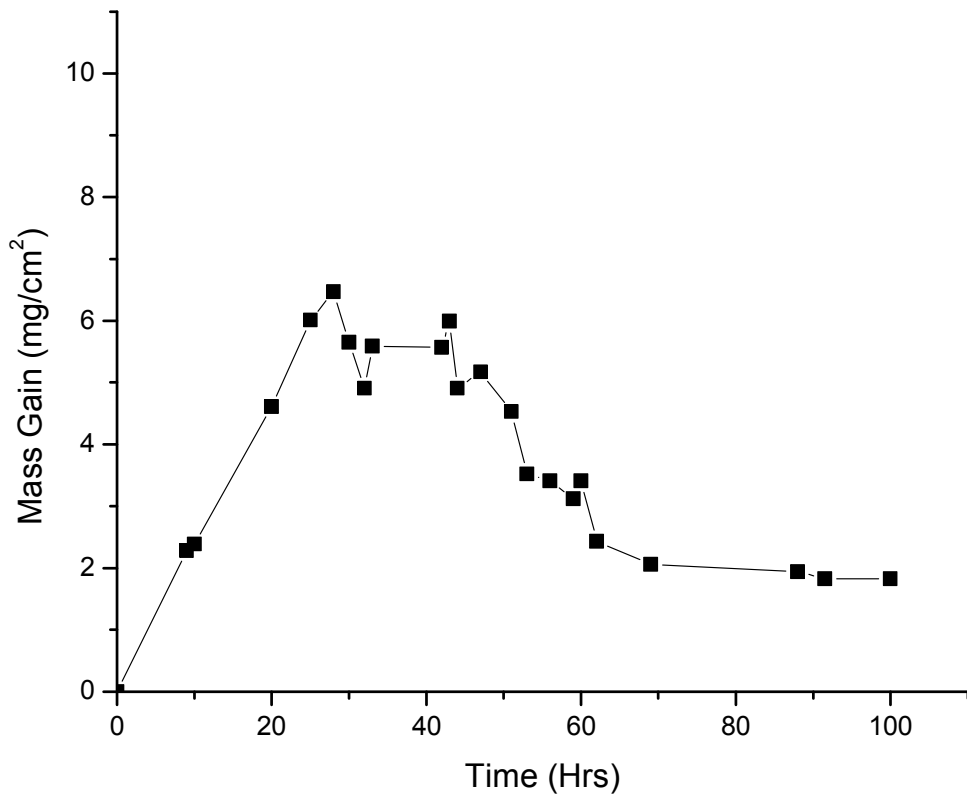


Figure 4-18: Mass gain curve for stepped/sequential oxidation tests at 1050°C.

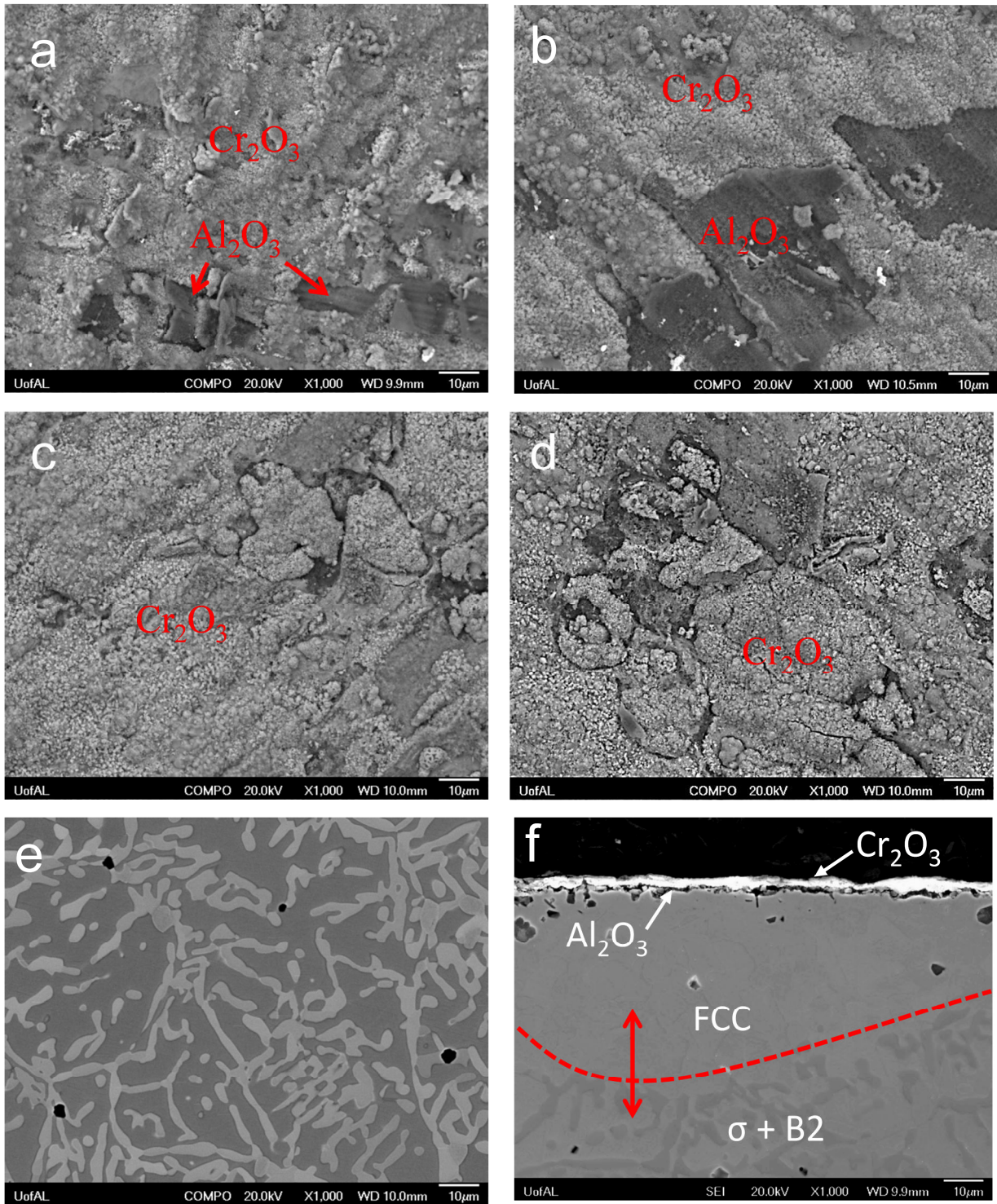


Figure 4-19: BSE images of the oxide formation for the $\text{Al}_{15}\text{Cr}_{10}\text{Co}_{35}\text{Ni}_{35}\text{Si}_5$ alloy after 5 h (a), 10 h (b), 24 h, and 50 h of oxidation at 1050°C and cross sectional BSE images of the alloy (e) and oxide scale (f) after 100 h of oxidation.

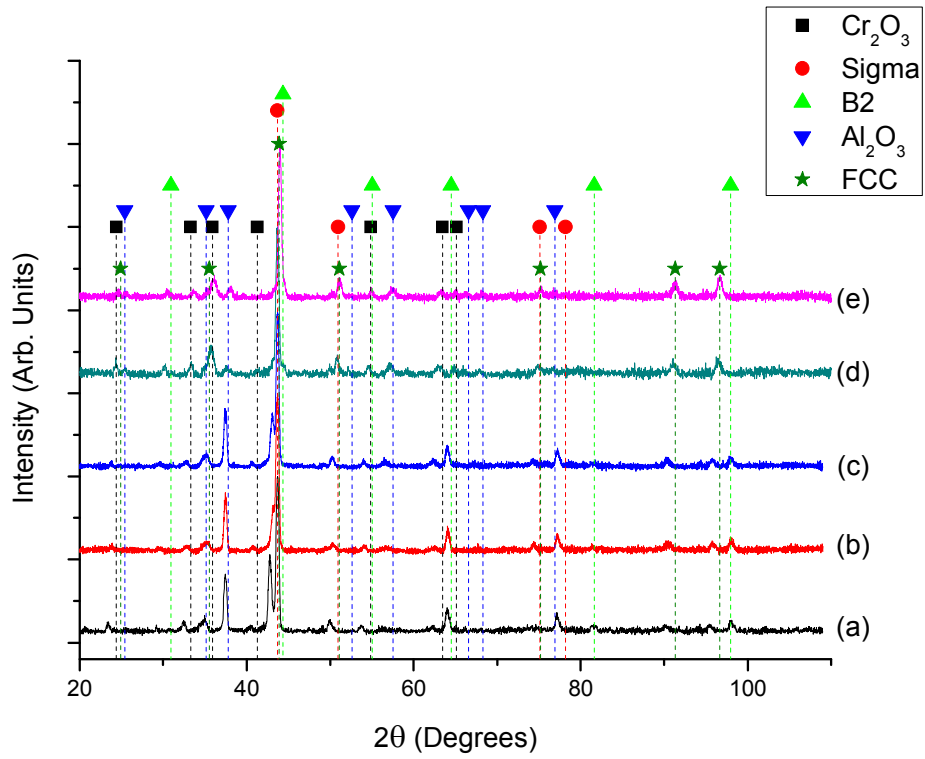


Figure 4-20: XRD patterns for the $\text{Al}_{20}\text{Cr}_{25}\text{Co}_{25}\text{Ni}_{25}\text{Si}_5$ alloy after oxidation for (a) 5 h, (b) 10 h, (c) 25 h, (d) 50 h, (e) 100 h at 1050°C .

layer of chromia, which was not observed in the specimens isothermally oxidized for 20, 96, and 500 h (described above). It is likely that all of the specimens formed a chromia layer first. However, in the case of this specimen, sequential oxidation is essentially cyclic oxidation. It is hypothesized that during the application of 100 1h cycles at 1050°C to the alloy, that conditions were amenable for rapid Cr diffusion to the alloy surface and through microcracks in the alumina scale to form the external layer of chromia. This diffusion would naturally occur during the heating and cooling stages where the differences in thermal expansion coefficient between alumina and chromia would manifest themselves most greatly.

The oxidation kinetics for this alloy are similar to those reported in Ni-Cr-Al alloys [84,85]. Base on the composition of the FCC phase formed under the oxide and assuming Ni/Co have equal probability for a given lattice site, the FCC region can be thought of as a ternary alloy. Base on this assumption the composition for the FCC region in weight percent is: Ni/Co 63.46 wt. %, Cr 30.40 wt. %, and Al/Si 6.14 wt.%. Giggins *et. al.* provided a ternary phase diagram for the type of oxidation observed within Ni-Cr-Al alloys. For the given FCC composition in the surface layer, the alloy is expected to form an external alumina scale [84]. For these compositions, the formation of this scale is preceded by a transient oxidation period. During this period there is rapid oxidation of the surface resulting in the formation of a thin chromia scale based on the high concentration of Cr in the sigma phase. This rapid oxidation of the Cr within the σ phase results in the phase transformation from σ to the γ -FCC. After the transition period, oxygen moves into the alloy forming alumina precipitates. This alumina layer inhibits the movement of oxygen further into the alloy and ultimately results in the formation of a continuous alumina scale below the initial transient chromia layer. Once the alumina scale has formed, the rate of growth is controlled by aluminum transportation through the scale.

4.6 Conclusions

In-depth analysis of the AlCrCoNiSi alloy revealed the following:

- (a) The as-cast alloy exhibited a cored dendritic microstructure. The primary dendrites were richer in Ni and Al while the interdendritic region was richer in Cr. The primary phases in the dendritic region were an ordered BCC (i.e., B2) phase that was isomorphous with β -NiAl. This region was also found to contain a high density of disordered BCC precipitates, that were rich in Cr and Co, but which had the same lattice parameter as the B2 phase. Based on diffraction data, it was deduced that these were α -(Cr,Co,Ni). The interdendritic regions were found to consist of fine σ phase lamellae or side plates interspersed with a B2 phase. This B2 phase had essentially the same composition as the phase observed in the dendritic regions, and was semicontinuous.
- (b) Heat treatments at 600, 700, and 900°C produced phase transformations and microstructural coarsening. At 700°C, the disordered BCC phase observed in the as-cast alloy transformed to equilibrium σ phase via an intermediate χ phase. The χ phase was ultimately consumed to form equilibrium σ . In addition, some disordered FCC phase precipitates were observed. Heat treatments at 900°C, led to the formation of very coarse microstructures consisting solely of σ and B2 phases.
- (c) Isothermal oxidation tests performed at 1050°C on the as-cast alloy revealing the formation of a continuous alumina scale. Mass was measured during the isothermal oxidation but no significant mass change was observed. The oxidized alloy consisted of two main phases: a B2 phase and σ phase that continued to coarsen with increasing oxidation time. APT was performed on the 20 h oxidized specimen revealing nano-scale sigma phase precipitates within the B2 phase. Similar precipitation was also observed

following long term heat treatments. An Al depleted γ -FCC region that was rich in Cr and Co was observed just below the oxide for all oxidized samples.

- (d) Sequential oxidation tests were also performed on the alloy. The same B2 and σ phases constituted the majority of this alloy. The γ -FCC phase was also observed just below the oxide. BSE SEM and EDS revealed that a thin layer of chromia had formed on the surface of the alloy above a continuous layer of alumina.

5. Al₁₅Ni₃₅Cr₁₅Co₃₅Si₅ ALLOY

5.1 Alloy Design and Crystal Structure

This alloy was designed using the method described in Chapter 4 [7]. The focus in this chapter was to develop an alloy that would contain less Al and which would consist of metastable FCC phase plus intermetallic precipitates. Using the atomic radii values published in reference [53], values of $\delta = 5.56\%$, $\Delta H_{\max} = 11.68 \text{ J/K}\cdot\text{mol}$, $\Delta S_{\max} = -17.17 \text{ kJ/mol}$, and $\Omega \approx 1.13$ were determined for the alloy which should, based upon the phase selection rules proposed by Yang and Zhang [7,20], yield an alloy consisting of a mixture of solid solution and intermetallic phases.

The as-cast alloy, shown in Fig. 5-1, was found to consist of large featureless regions that were rich in Ni and Co (labeled A) and regions containing alternating light and dark bands that were rich in Ni, Co, and Al (labeled B). The microstructures observed in region B were reminiscent of the martensitic regions reported in a number of Ni+Co based shape memory alloys [20,29,54,86-90]. Diffraction analyses, shown in Figs. 5-2, 5-3, and Table 5-1, revealed the presence of an L₁₀ Co₃₈Ni₃₃Al₂₉ phase ($a = 2.789 \text{ \AA}$, $c = 2.968 \text{ \AA}$), a disordered FCC γ phase, and an ordered FCC L₁₂ phase (i.e., γ') precipitates ($a = 3.628 \text{ \AA}$). A bright field TEM image taken from the martensitic region revealed a twinned martensite with a $(1\bar{1}1)$ twinning plane. It has been shown for certain CoNiAl alloys that a martensitic transformation from B2 to L₁₀ martensite can occur during cooling. This transformation results in symmetry loss within the alloy and in micro-twinning such as that shown in Fig. 5-3 [89,91]. The γ phase, which is the result of an aluminum depleted NiCo rich matrix with ordered γ' precipitation has been observed

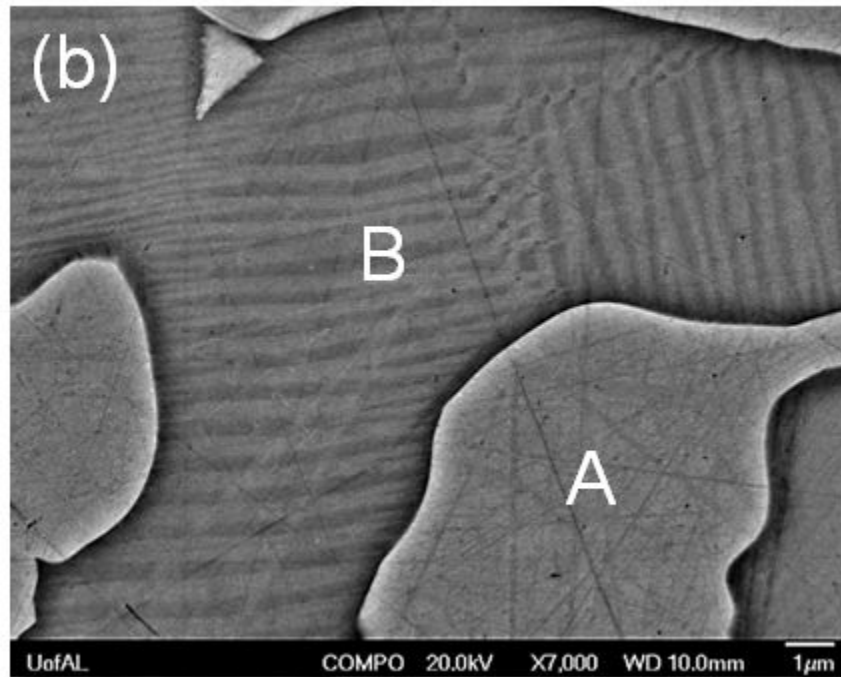
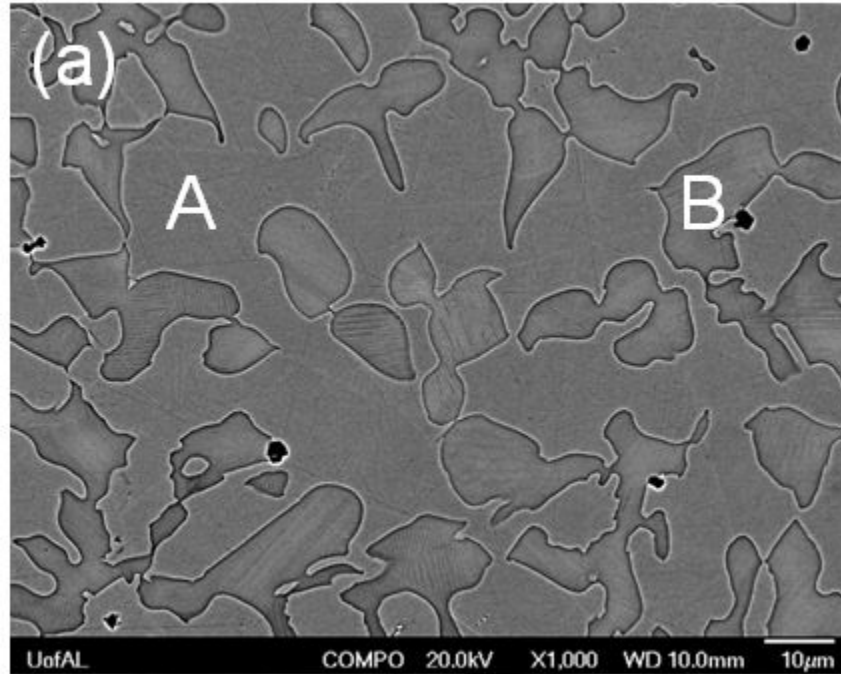


Figure 5-1: SEM backscattered electron images of the $\text{Al}_{15}\text{Cr}_{10}\text{Co}_{35}\text{Ni}_{35}\text{Si}_5$ alloy in the as-cast state. (a) Low magnification image showing disordered NiCo FCC regions (labeled A) and martenstic regions (labeled B). (b) A higher magnification SEM image.

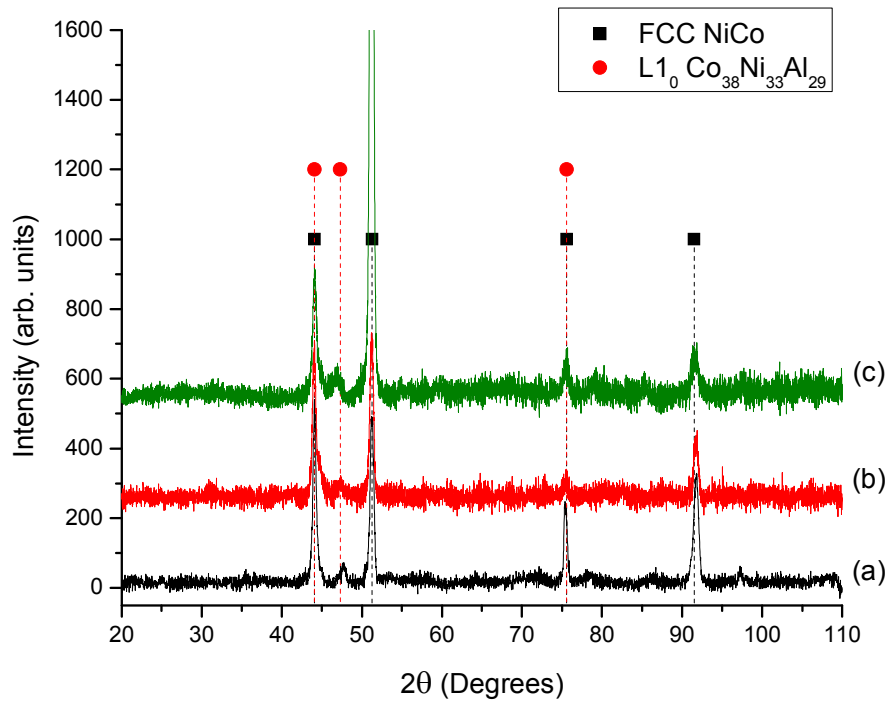


Figure 5-2: XRD patterns for the $\text{Al}_{15}\text{Cr}_{10}\text{Co}_{35}\text{Ni}_{35}\text{Si}_5$ alloy in the as-cast and select annealed conditions. (a) As-cast, (b) 600°C/20 h, and (c) 900°C/100 h.

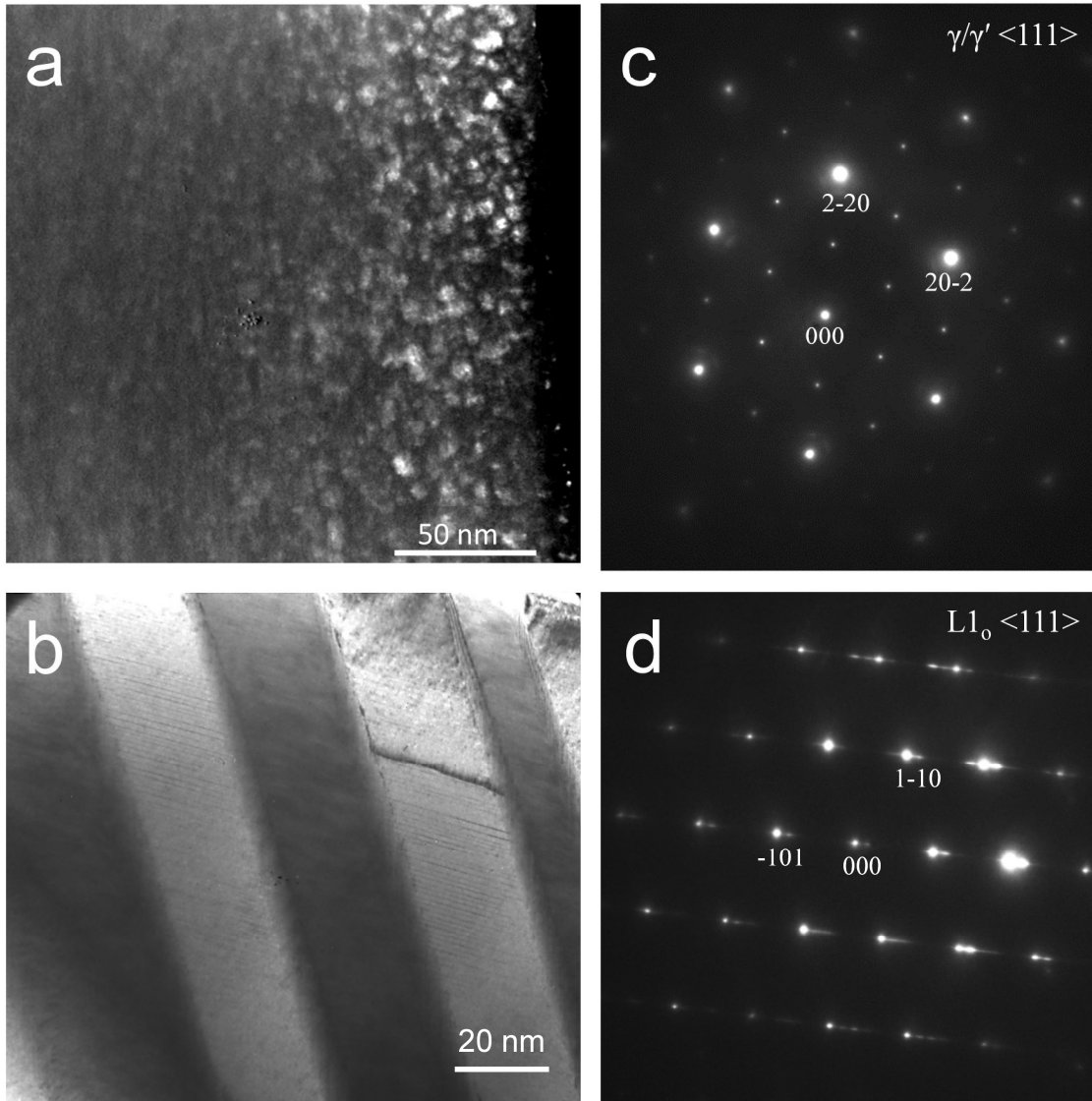


Figure 5-3: TEM bright field images and SAED patterns collected from regions A and B in the microstructure. Figures (a) and (c), which were collected from region A, indicate the presence of γ -FCC and γ' -L₂ phases. Figures (b) and (d), which were collected from region B, indicate the presence of a twinned L₁₀ martensite.

Table 5-1: Compositions of the (gamma)-region and martensitic region (at.%).

Zone/phase	Al	Co	Cr	Ni	Si
γ -FCC (A)	6.89 ± 0.04	40.85 ± 0.14	13.37 ± 0.69	35.80 ± 0.13	3.08 ± 0.02
$L1_0$ (B)	21.30 ± 0.09	27.69 ± 0.18	5.50 ± 0.07	40.75 ± 0.21	4.75 ± 0.05

in HEAs and Ni-base super alloys [22-25,30,92,93]. This formation of γ' precipitates is often the result of the ordering process during cooling. Fig. 5-4 and Table 5-2 show results from APT studies performed on the as-cast. The results confirmed the presence of a Co-rich γ matrix that contained Ni-rich γ' precipitates. No compositional variations were observed within the martensitic regions.

5.2 Influence of Annealing on Microstructure

Pieces of the as-cast button were heat treated at 600, 700, and 900°C for times ranging from 0.25 to 100 h. After each heat treatment step, Vickers hardness measurements were collected resulting in the hardening curves shown in Fig. 5-5. For the 600°C sample, a peak hardness of 495.9 ± 15.47 VHN was observed at approximately 20 h, with an increase of approximately 100 VHN above the as cast specimen hardness of 361.3 ± 6.45 VHN. The 700°C and 900°C specimens had relatively little fluctuation in hardness during aging with a peak hardness of 471.7 ± 16.44 VHN and 365.9 ± 18.86 VHN respectively.

Fig. 5-6a shows a BSE image of a specimen after annealing at 600°C/20 h. This image shows needle-like precipitates within region A. Figs. 5-7 show a STEM HAADF image of the two regions within the alloy and corresponding SAED patterns from each. The SAED patterns confirmed the presence of γ -FCC and γ' -L1₂ phases in Zone A and of a twinned L1₀ phase in zone B. Fig. 5-8 shows a bright field TEM image and a corresponding SAED pattern collected from zone B. From this data it was deduced that the plate-like precipitates were likely a G-phase (i.e., Ni₁₆Si₇Cr₆). Atom probe analysis was performed to provide a more clear understanding of the precipitate composition and is presented in Fig. 5-9 and Table 5-3. The analysis revealed large thin precipitates with high concentrations of Si and Ni. It is believe that Al substituted into

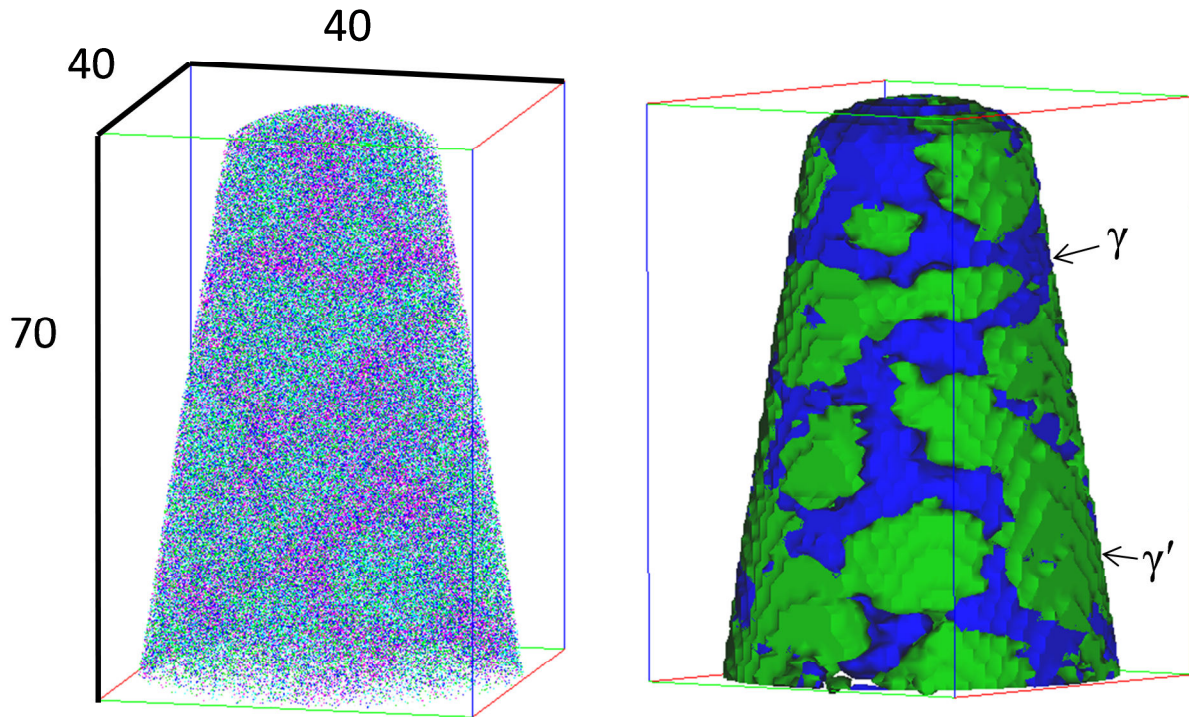


Figure 5-4: A 3D reconstruction of the $\text{Al}_{15}\text{Cr}_{10}\text{Co}_{35}\text{Ni}_{35}\text{Si}_5$ alloy showing γ' -precipitation (green) within a γ -matrix (blue). Dimensions are in nm.

Table 5-2: Compositions of the γ -matrix with γ' -precipitates as determined via APT (at.%).

Element	γ -Matrix Composition (Atomic)	γ' -Precipitation Composition (Atomic)
Al	7.70 ± 0.024	13.98 ± 0.022
Si	3.86 ± 0.022	4.26 ± 0.017
Cr	14.00 ± 0.035	8.275 ± 0.020
Co	42.59 ± 0.044	32.69 ± 0.028
Ni	31.86 ± 0.037	40.79 ± 0.028

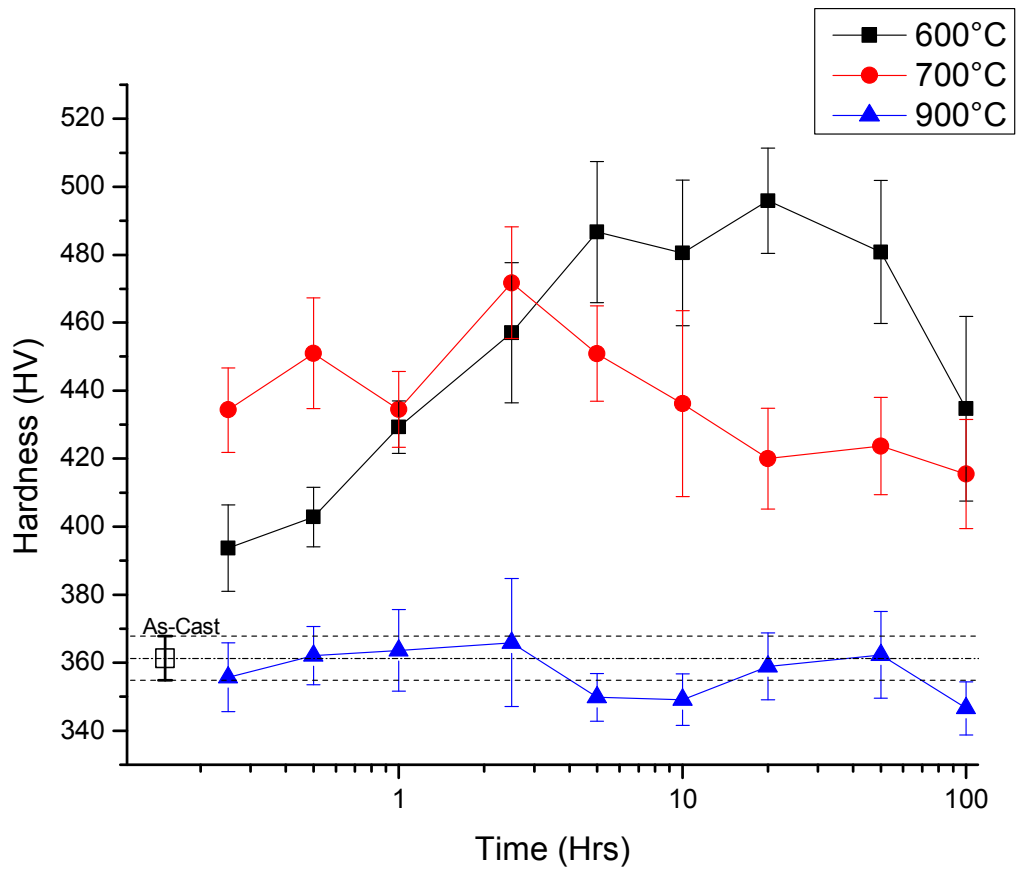


Figure 5-5: Variation in Vickers hardness with aging time for $Al_{15}Cr_{10}Co_{35}Ni_{35}Si_5$ alloy

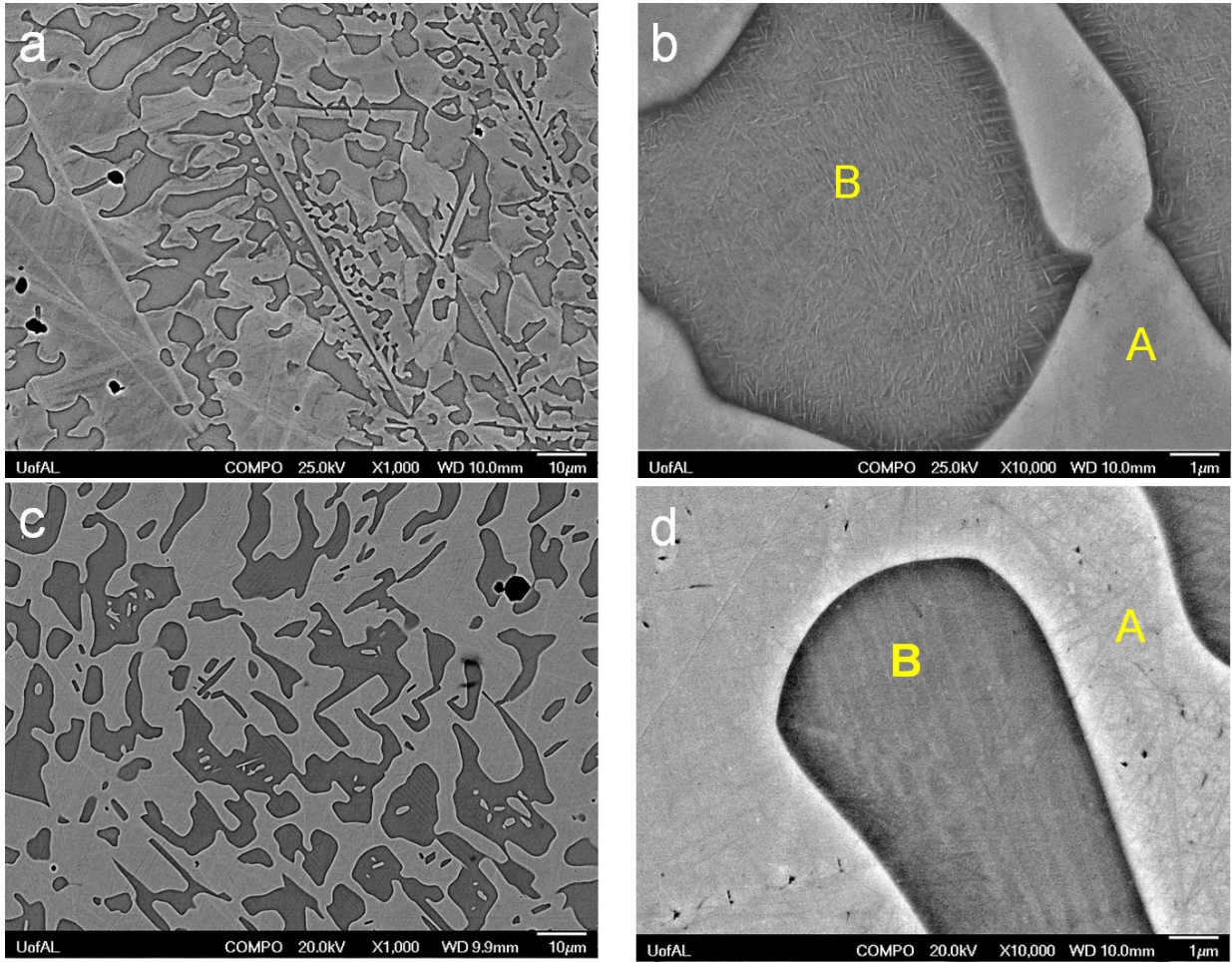


Figure 5-6: SEM backscattered electron image of the $\text{Al}_{15}\text{Cr}_{10}\text{Co}_{35}\text{Ni}_{35}\text{Si}_5$ alloy after aging for $600^\circ\text{C}/20\text{ hr}$ (a-b) and $900^\circ\text{C}/100\text{ hr}$ (c-d).

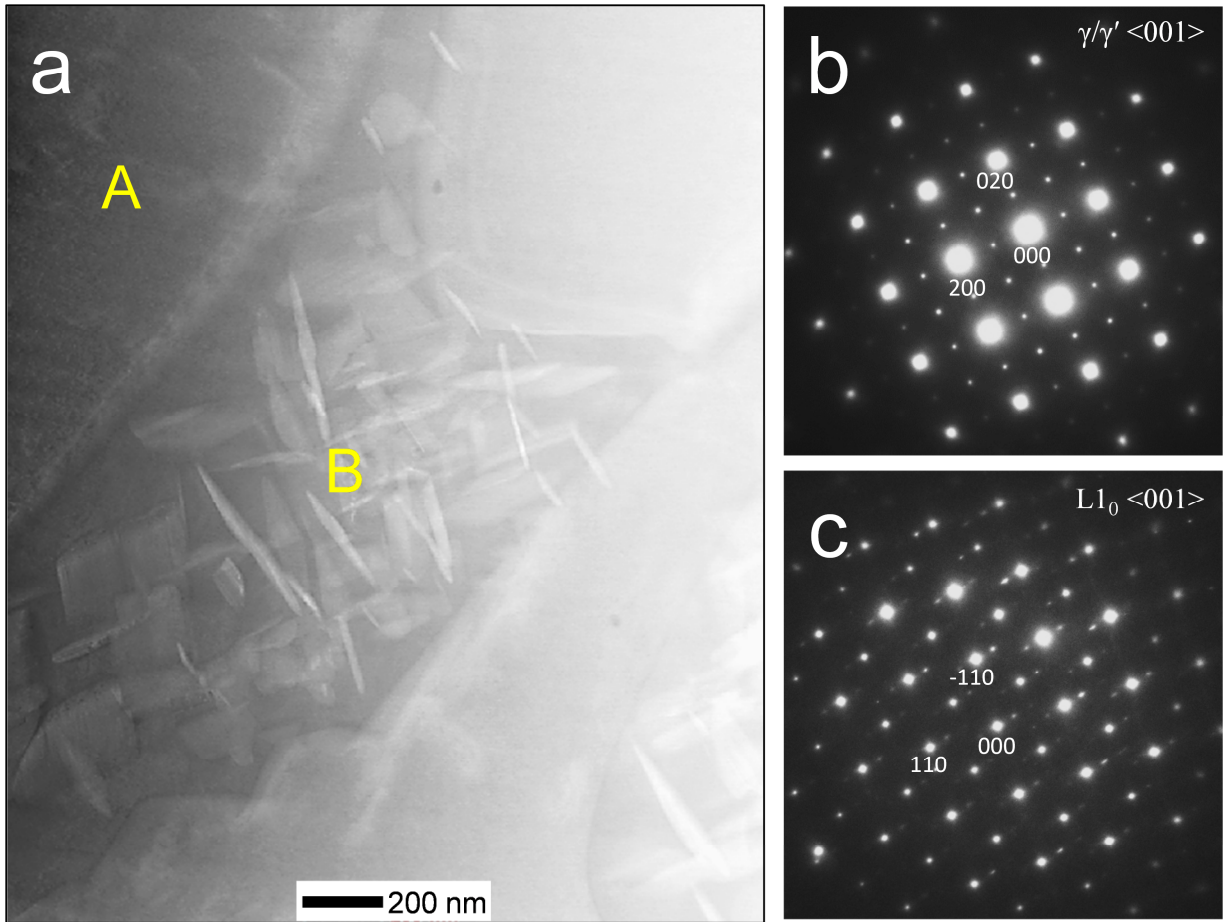


Figure 5-7: STEM-HAADF image illustrating the needle-like G phase precipitates in the martensitic region of the 600°C/20 hr heat treated specimen with accompanying SAED patterns for the two regions.

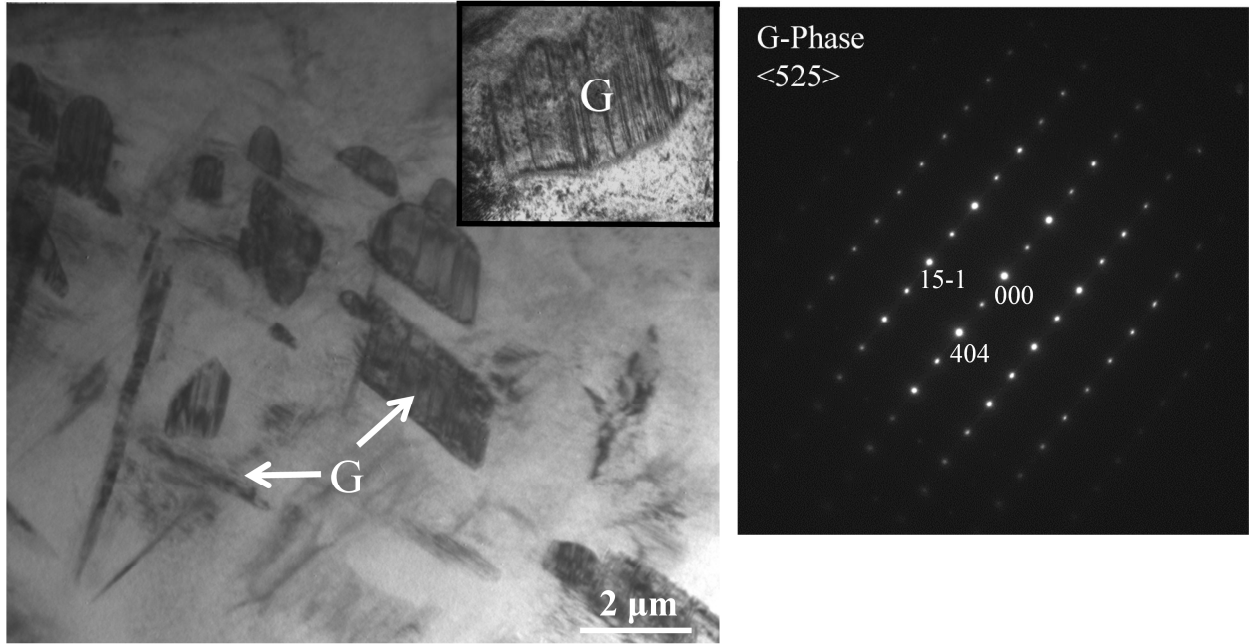


Figure 5-8: Brightfield TEM images showing needle-like G-phase precipitates and an SAED pattern collected from one of the precipitates.

Cr lattice sites. The G-phase was first observed in iron-based superalloys by Beattie and VerSnyder and is a metastable intermetallic phase that resulted from the high Si concentration within the L1₀ region [53]. This phase was later observed by Gudmundsson *et. al.* in a Co-Ni-Cr-Al-Y plasma sprayed coatings [12]. Fig. 5-6b shows the microstructure of the alloy after heat treating at 900°C/100 h. The plate-like precipitates in zone B disappeared and the microstructure coarsened, still consisting of the two main regions observed in the as-cast alloy. TEM analysis was also performed on further aged samples and the needle like precipitation was not observed but the γ -FCC matrix with γ' precipitation and martensitic L1₀ phase were present.

5.3 Comparison of Experimental and Computed Phase Equilibria

The phases that formed during annealing were compared with those calculated using Thermo-CalcTM. The results of the calculations are presented in Fig. 5-10 and Table 5-4. As was previously mentioned, two main phases observed after casting and annealing were a disordered FCC γ phase, an ordered FCC γ' -L1₂ phase, which precipitated within the FCC γ , and a tetragonal L1₀ phase. These phases were observed even after 1000 h of heat treatment at 900°C and were initially believed to be the equilibrium phases. However, the γ' was not predicted for this heat treatment temperature and the L1₀ phase was not predicted by Thermo-CalcTM for any of the heat treatment temperatures used in this study.

At 600°C and 700°C an ordered FCC γ' -L1₂ phase was predicted along with disordered BCC and B2 (i.e., ordered BCC) phases. However, only the γ' phase was observed and only in the form of precipitates dispersed in an FCC γ matrix. For the 900°C heat treatment, it was predicted that the γ' phase would transform to disordered γ -FCC phase and that ordered and disordered BCC phases would form. Again the ordered and disordered BCC phases were not

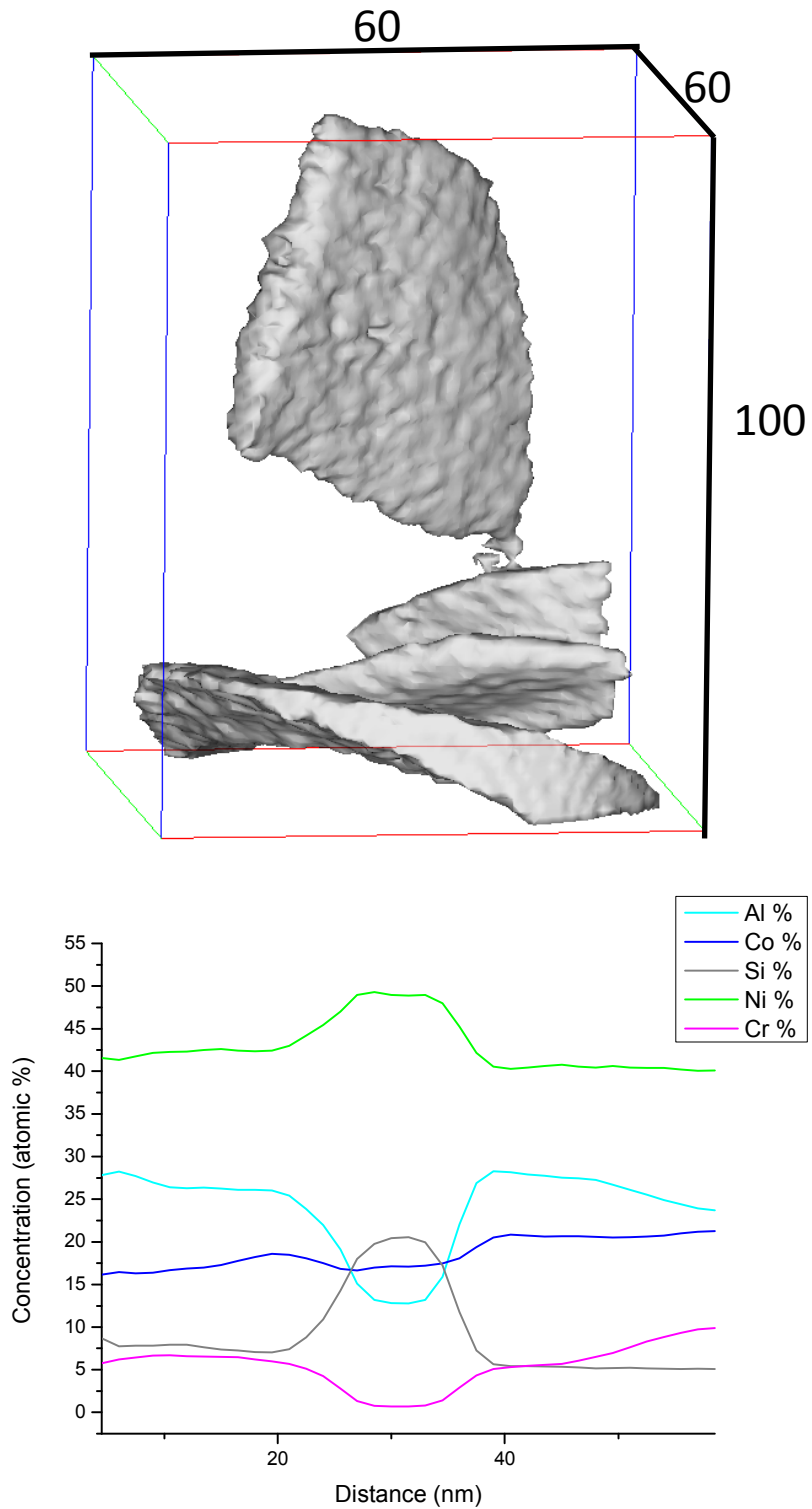


Figure 5-9: A 3D reconstruction of the G-phase precipitates with accompanying concentration profile for a select precipitate. Dimensions are in nm.

Table 5-3: Compositions of the G-phase and surrounding matrix as determined via APT (at.%).

Element	G-phase Composition (Atomic)	Matrix Composition (Atomic)
Al	13.92 ± 0.025	25.97 ± 0.015
Si	18.72 ± 0.032	6.10 ± 0.010
Cr	1.48 ± 0.009	6.64 ± 0.008
Co	16.73 ± 0.027	19.98 ± 0.013
Ni	49.15 ± 0.035	41.31 ± 0.016

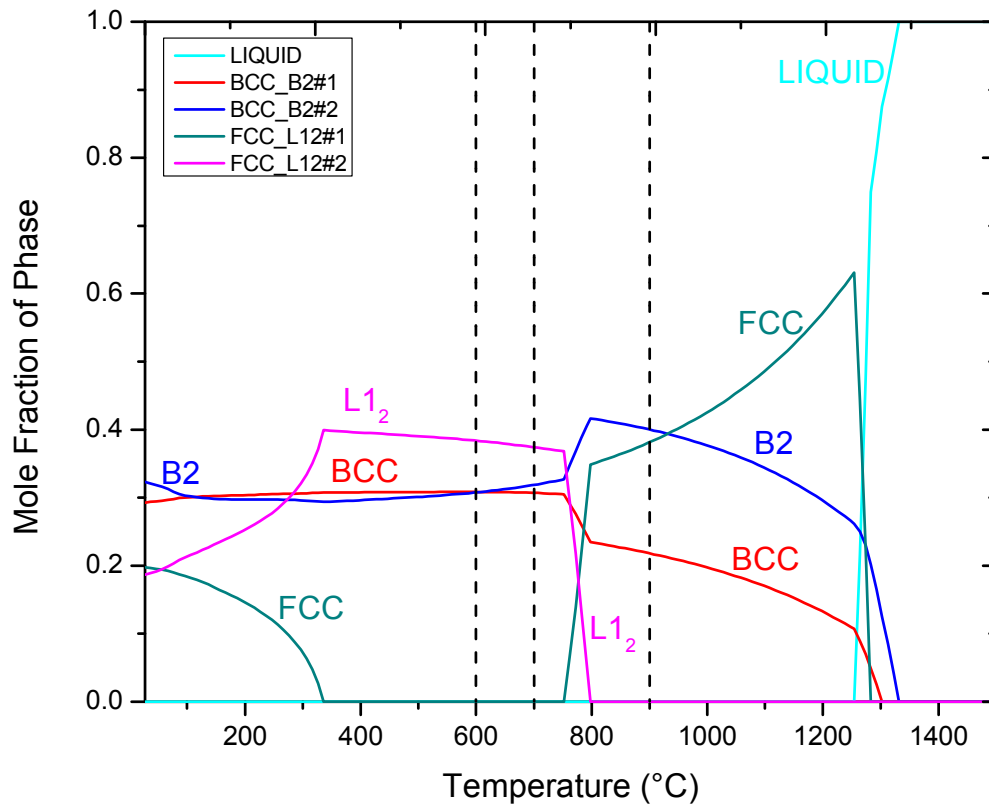


Figure 5-10: Thermo-Calc equilibrium phase diagram calculated for $\text{Al}_{15}\text{Cr}_{10}\text{Co}_{35}\text{Ni}_{35}\text{Si}_5$ using the CALPHAD method with the TCNI5 database.

Table 5-4: Comparison of the phases observed experimentally to that determined via Thermo-Calc

Temperature (°C)	Experimental	Thermo-Calc
600	$\gamma+L1_2+L1_o+G$	B2+BCC+L1 ₂
700	$\gamma+L1_2+L1_o$	B2+BCC+L1 ₂
900	$\gamma+L1_2+L1_o$	BCC+B2+FCC

occurred during cooling. For example, Schryvers and co-workers have shown that twinned L1₀ martensites frequently form in splat quenched B2 NiAl alloys [90,94,95]. Furthermore, these types of martensites have been observed in a number of shape memory alloys systems, often originating from high temperature B2 austenite phases [89,91,96,97]. It is thus concluded that B2 is one of the equilibrium phases for all of the heat treatment temperatures and times that were investigated.

The observed high temperature γ' phase is a bit more puzzling. Recent work by Task *et al.* has shown that the addition of Co in excess of 5 wt.% can suppress the formation of γ' in multicomponent NiCrAlY coating alloys [98]. Given the nature of this five component alloy, it is possible that this discrepancy is related to data limitations of the Thermo-CalcTM database.

Thus, the differences between the experimental and calculated phase content can be attributed to phase transformations that occurred during cooling and to data limitations in the Thermo-CalcTM database. In particular, the L1₀ martensite phase included in the TCNI5 database needs to be re-evaluated and simulated to include Ni and/or Co. When selecting only the phases observed within the alloy the phase diagram was predicted to contain a single γ -FCC phase for all temperature ranges.

5.4 Isothermal Oxidation Behavior

The as-cast alloy was isothermally oxidized at 1050°C for times ranging from 20 h to 500 h. Mass change results are summarized in Table 5-5. Fig. 5-11, shows resulting SEM backscattered electron images of the oxide scale and underlying alloy after each step of oxidation. Almost no mass change occurred during oxidation but spallation of the oxide scale was observed after 500 h. The spallation is believed to have occurred as a result of lateral oxide scale growth. This growth mechanism creates large growth stresses within the oxide resulting in

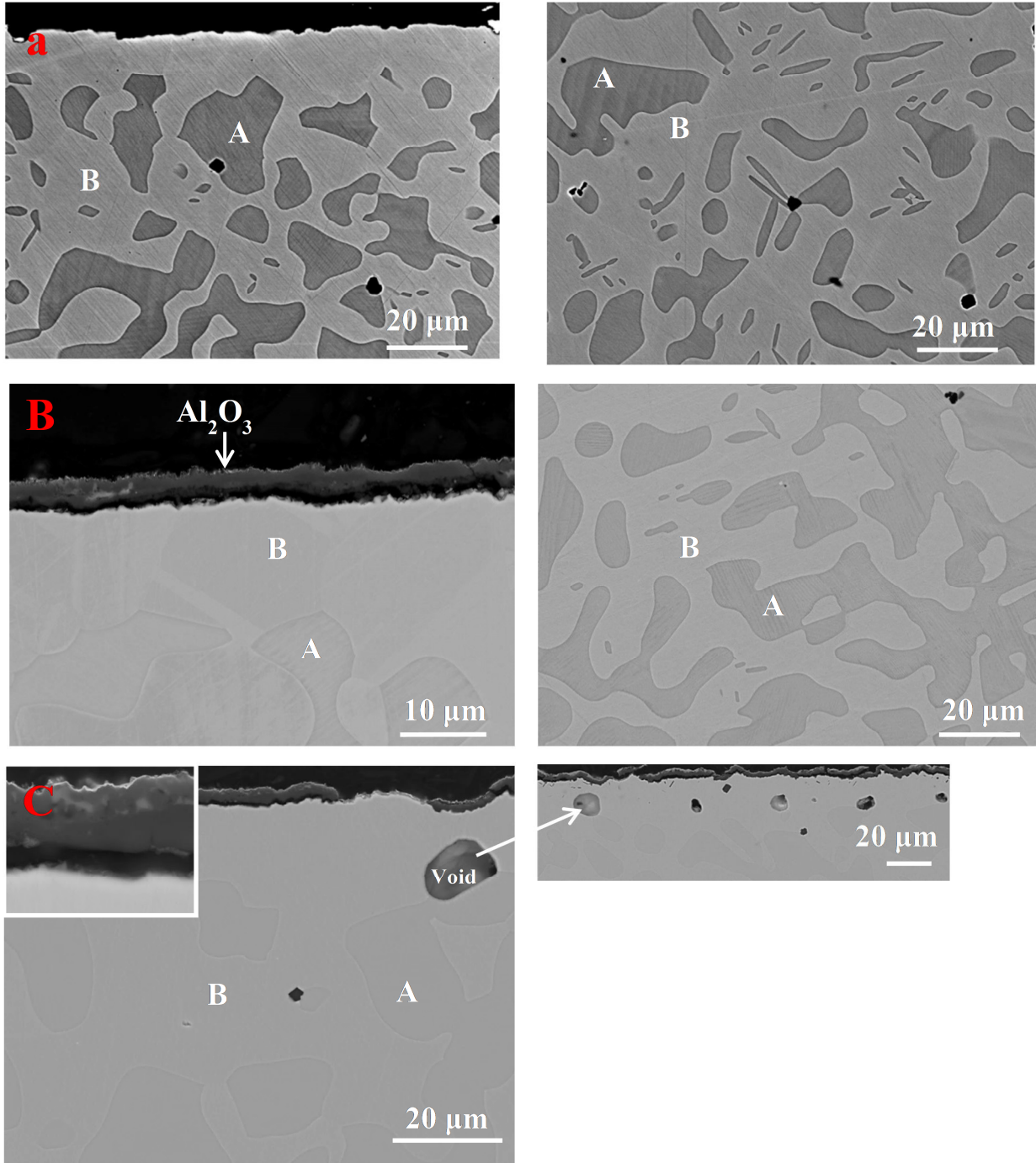


Figure 5-11: Backscattered SEM images of the oxide scale and microstructure within the alloy for (a) 20 h (b) 96Hrs and (c) 500 h of isothermal oxidation at 1050°C

Table 5-5: Oxidation results for the $\text{Al}_{20}\text{Cr}_{25}\text{Co}_{25}\text{Ni}_{25}\text{Si}_5$ alloy.

Oxidation Time (h)	Initial Weight (g)	Final Weight (g)	Change (g)	Surface Area (cm^2)	Mass/Area (g/cm^2)
20	0.3975	0.3975	0.0000	1.112	0.000
96	0.2095	0.2098	0.0003	0.621	4.829×10^{-04}
500	0.3729	0.3735	0.0006	1.083	5.542×10^{-04}

crack development within the scale [99-101]. The cracks allowed inward migration of oxygen resulting in the formation of an inner oxide scale, Fig. 5-11(c). With increasing oxidation time the outer scale became non uniform creating voids within the scale ultimately causing spallation in select areas. Voids typically less than 15 μ m were also observed just below the oxide scale after 500 h of oxidation. The voids are the result of aluminum and chromium diffusing from the γ -region [55]. The void formation is believed to be created by a Kirkendall effect where rapid diffusion of Al and Cr to the oxide scale results in an unequal flux creating large amounts of vacancies [26,34,99,102-104]. Fig. 5-12 shows XRD results after each step of oxidation. The results vary little with oxidation time, but show the presence of the γ -FCC, $L1_0$ and α - Al_2O_3 . Fig. 5-13 shows a brightfield TEM image with corresponding SAED which confirmed the presence of a tetragonal $L1_0$, FCC γ and γ' - $L1_2$ phases after oxidation, as were also seen in the heat treated alloys. What is interesting to note is that the scale spallation and void formation observed in this alloy were not seen after 500 h of oxidation in the previously studied $Al_{20}Cr_{25}Co_{25}Ni_{25}Si_5$ alloy even though that alloy contained a similar γ -FCC region below the oxide. This is attributed to the higher Cr and lower Ni concentrations in the γ -region of the $Al_{20}Cr_{25}Co_{25}Ni_{25}Si_5$ alloy, which catalyzed the growth of the alumina scale through their influences on Al activity [85,104,105].

The alloy was also oxidized for 100 h at 1050°C, but removed hourly to determine mass change. Fig. 5-14 shows the mass change during oxidation. An initial increase in mass is observed, but after 15 h spallation begins and mass is lost. After 100 h, significant mass loss occurred due to spallation. SEM and XRD analysis was performed after 5, 10, 24, 50, and 100 h, with the results shown in Fig. 5-15 and Fig. 5-16. XRD revealed the presence of a γ -FCC phase and alumina. The $L1_0$ phase was still present within the alloy but the FCC layer below the oxide

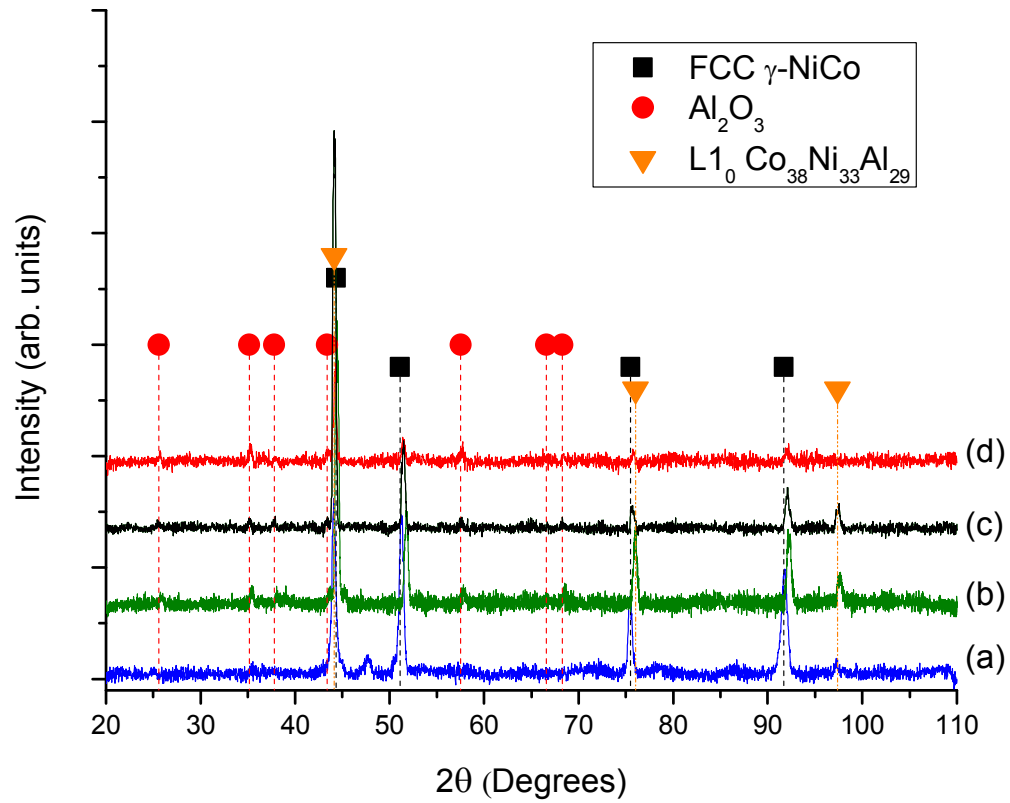


Figure 5-12: XRD pattern of the $\text{Al}_{15}\text{Cr}_{10}\text{Co}_{35}\text{Ni}_{35}\text{Si}_5$ alloy for the as-cast and oxidized states. (a) as-cast, (b) 20 h oxidized, (c) 96 h oxidation, (d) 500 h oxidation

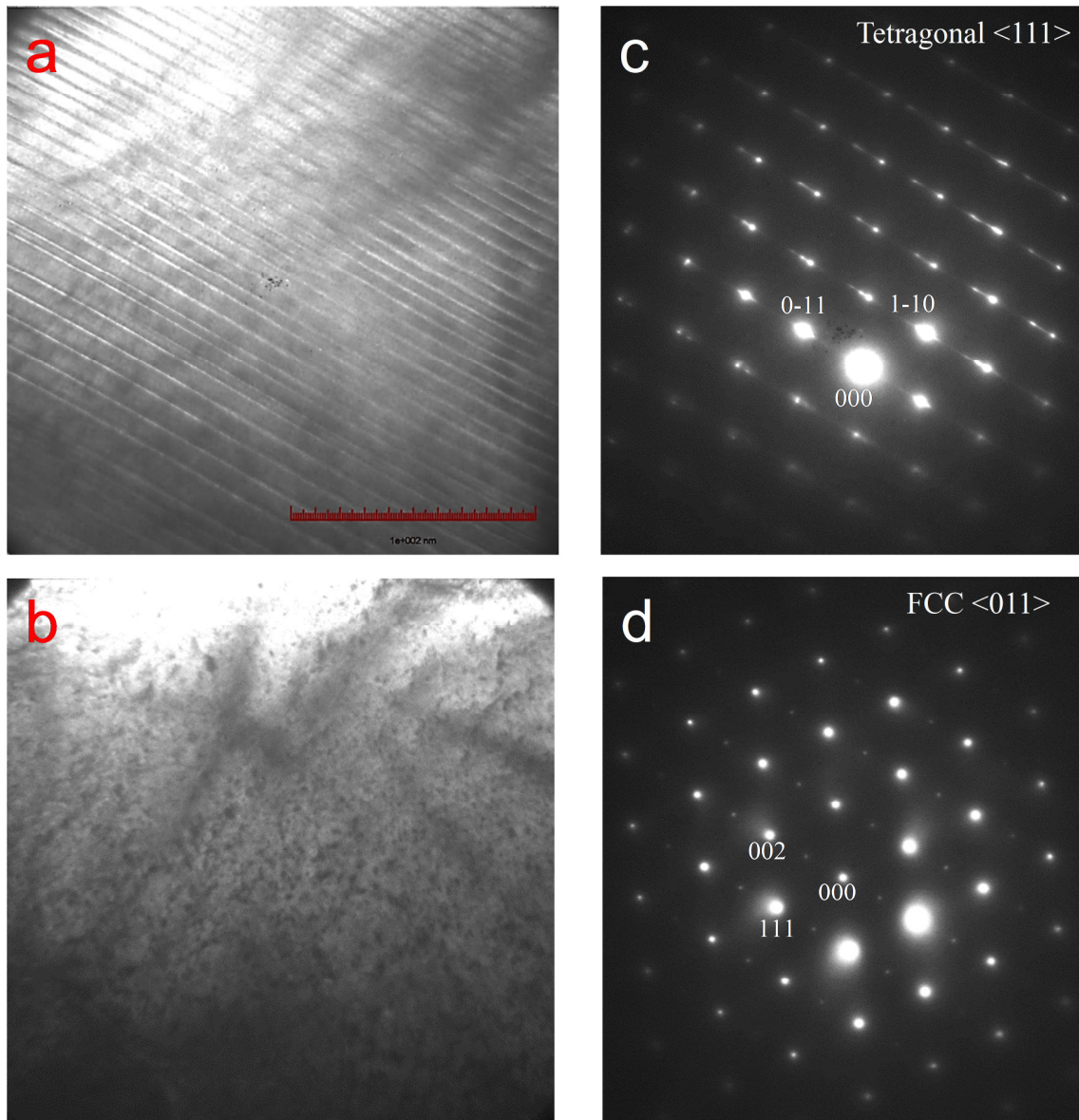


Figure 5-13: Brightfield TEM images and associated SAED patterns collected from regions A and B of the alloy after oxidation at 1050°C. (a) and (c) were collected from region A showing the results of a martensitic transformation. (b) and (d) were collected from the region B which contained fine γ' precipitates dispersed in an FCC γ matrix.

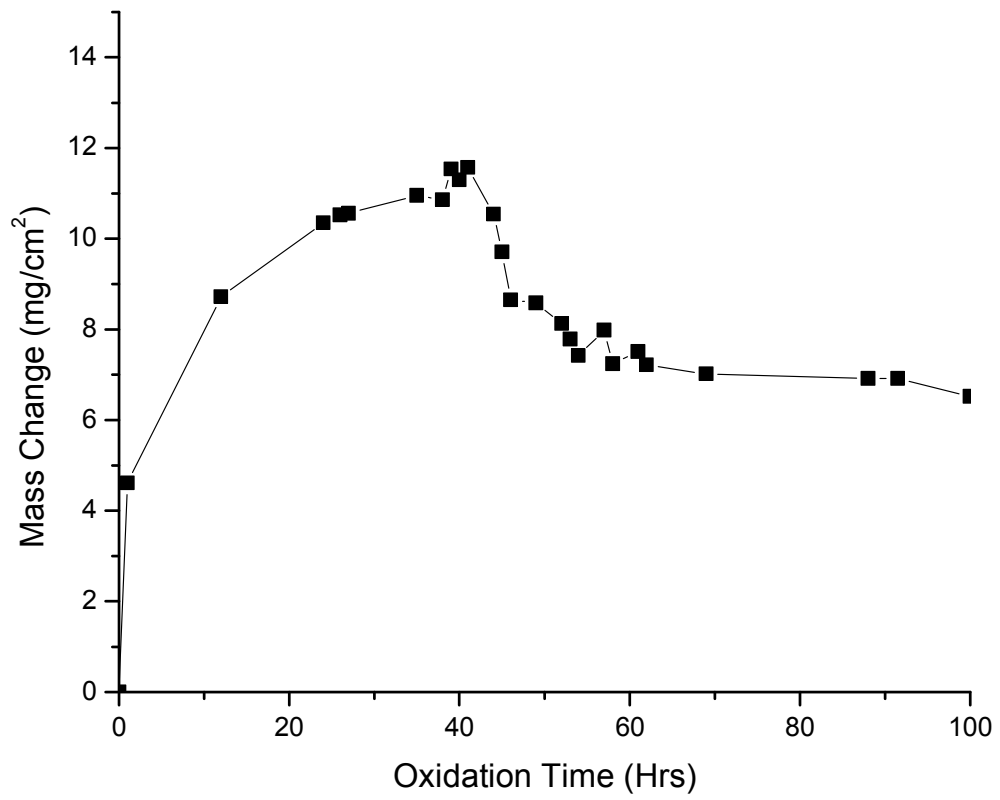


Figure 5-14: Mass gain curve for stepped/sequential oxidation.

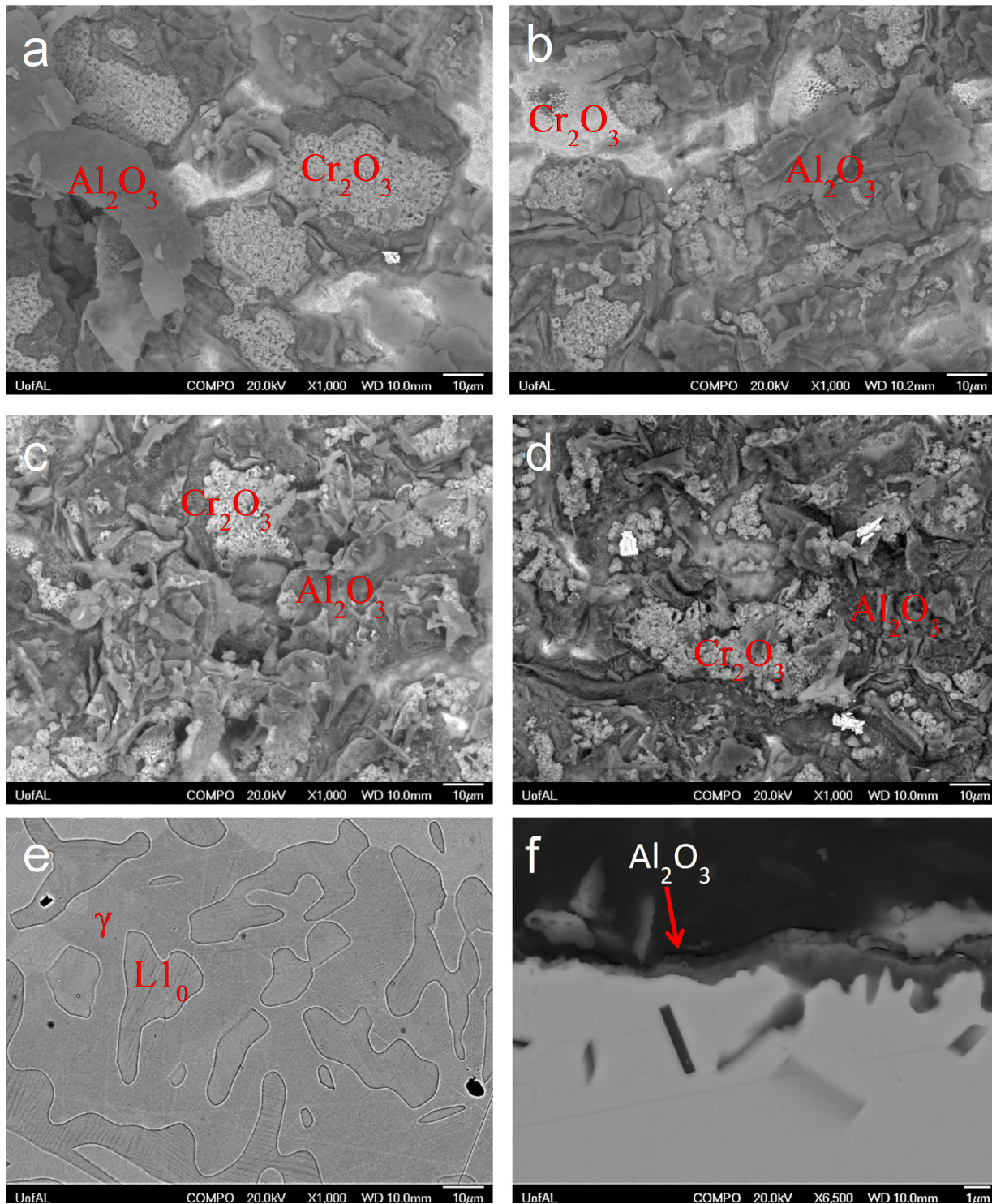


Figure 5-15: Backscattered electron images of the oxide formation for the $\text{Al}_{15}\text{Cr}_{10}\text{Co}_{35}\text{Ni}_{35}\text{Si}_5$ alloy after 5 h (a), 10 h (b), 24 h, and 50 h of oxidation at 1050°C and cross sectional backscattered electron images of the alloy (e) and oxide scale (f) after 100 h of oxidation

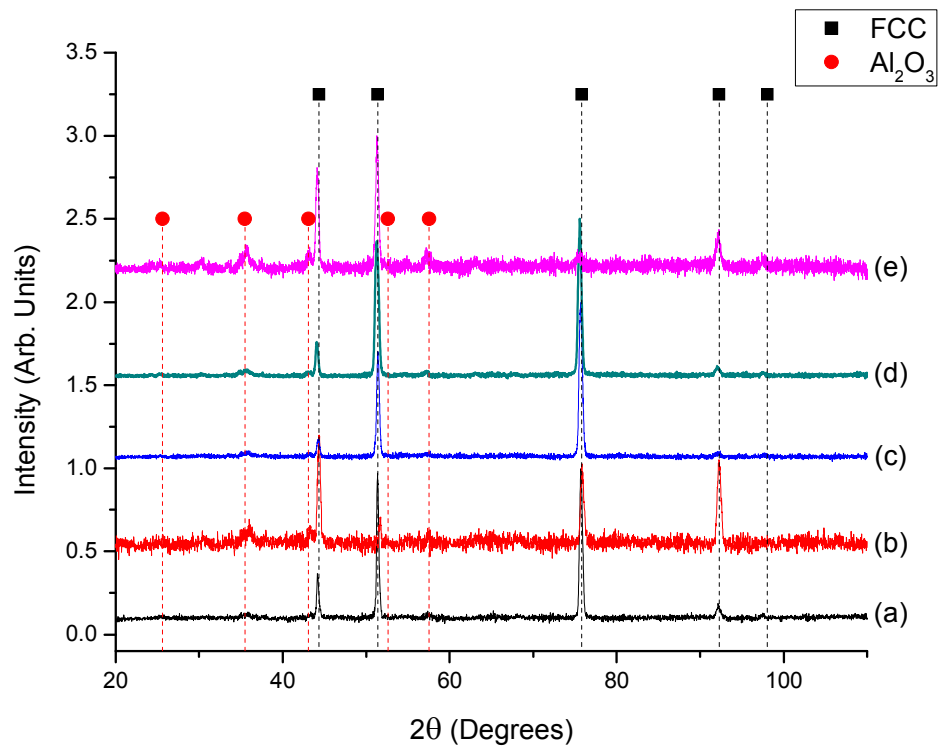


Figure 5-16: XRD patterns for the $\text{Al}_{15}\text{Cr}_{10}\text{Co}_{35}\text{Ni}_{35}\text{Si}_5$ alloy after oxidation for (A) 5 h, (B) 10 h, (C) 25 h, (D) 50 h, (E) 100 h at 1050°C .

scale was several microns thick, resulting in absence of the $L1_0$ phase from the XRD patterns. The SEM backscattered electron images revealed a non-uniform oxide layer of both chromia and alumina with areas of bare alloy. After 100 h, the specimen was mounted and the cross section analyzed revealing void formation and oxidation beneath the oxide scale. An alumina scale was present but less than $1\mu\text{m}$ thick.

The observed oxidation behavior was similar to that previously discussed for the $\text{Al}_{20}\text{Cr}_{25}\text{Co}_{25}\text{Ni}_{25}\text{Si}_5$ alloy. Based on the composition of region A and assuming that Ni/Co and Al/Si have an equal probability for occupying a given lattice site, this region can be qualitatively treated as a ternary Ni-Cr-Al alloy. Using this assumption, the composition for the region A in weight percent is: Ni/Co 82.71 wt.%, Cr 10.61 wt.%, Al/Si 6.68 wt.%. The work of Giggins et. al. provided a ternary phase diagram that can be used to predict the type of oxidation that will occur in Ni-Cr-Al based alloys [84]. On this basis, the phase (and the alloy) fall close to the group 1 and group 2 intersections. Group 1 alloys exhibit a tendency towards the formation of scales consisting of a mixture of oxides that are not protective. Group 2 alloys tend to form chromia surface scales with a subscale of alumina. Group 3 alloys tend to form protective external alumina scales. As seen in Fig. 5-15, the alloy forms both alumina and chromia after just 5 h of oxidation. This is because the high concentration of Si within the alloy which promotes the formation of both alumina and chromia and the transient nature of the oxidation. The oxidation kinetics can best be described by an initial formation of spinel ($\text{Ni}(\text{Cr},\text{Al})_2\text{O}_3$), NiO, and chromia. As oxidation time increases alumina formation begins below the initial oxide layer. This results in cracking of the surface oxide layer exposing the alumina and causing spallation. As oxidation time increase, alumina becomes the predominate oxide formed but

chromia and spinel oxides also form resulting in the discontinuous alumina and chromia oxide scale.

5.5 Conclusions

An $\text{Al}_{15}\text{Cr}_{10}\text{Co}_{35}\text{Ni}_{35}\text{Si}_5$ alloy was produced via arc melting in an argon atmosphere. Pieces of the as-cast alloy were heat treated and oxidized for varying lengths of time at three different temperatures to assess phase formation and oxidation behavior. The test revealed:

- a) The as-cast samples were found to contain three phases: an L1_0 -AlNiCo phase, a γ -FCC phase, and ordered γ' precipitates. The L1_0 phase formed as a result of the martensitic transformation of an equilibrium B2 phase during cooling. The γ' represents an equilibrium phase that would have precipitated out during cooling.
- b) After heat treatment needle like precipitates were observed within the L1_0 region following heat treatments of $600^\circ\text{C}/20$ h. Atom probe tomography and TEM analysis revealed the precipitates to be G-phase. Further aging at this temperature resulted in the same phases observed in the as-cast specimen.
- c) Isothermal oxidation test were performed at 1050°C with little to no mass gain or loss observed. Spallation of the oxide scale was observed after 500 h of oxidation and was accompanied by the formation of voids under the oxide scale. The void formation is a result of the Cr and Al diffusion to the surface to form the oxide scale.
- d) A stepped/sequential oxidation test was also performed which showed the formation of a mixed oxide scale that contained alumina and chromia. During the oxidation test, which was akin to cyclic testing, spallation of the oxide scale was observed resulting in mass loss during oxidation.

6. $\text{Al}_{17}\text{Ni}_{28}\text{Cr}_{26}\text{Co}_{28}\text{Si}_1$ COATINGS

6.1 *As-Cast and Annealed Microstructure*

An AlNiCrCoSi HEA coating with a composition that was similar to the $\text{Al}_{20}\text{Cr}_{25}\text{Co}_{25}\text{Ni}_{25}\text{Si}_5$ alloy described in Chapter 4 was prepared because of its high hardness and oxidation behavior. The as-deposited HEA coatings were dense and conformal showing no apparent chemical interactions with the underlying substrates. Fig. 6-1 shows representative XRD patterns collected from as-deposited and annealed coatings that were deposited onto alumina substrates. From the XRD, the as-deposited coatings were found to be single phase with metastable FCC crystal structures. Annealing resulted in the formation of additional phases, the contents of which increased with annealing time. After annealing four main phases were observed: a body-centered tetragonal σ phase ($D8_6$ -type crystal structure, $a = 9.120 \pm 0.081 \text{ \AA}$, $c = 4.718 \pm 0.084 \text{ \AA}$, $c/a = 0.52$), an ordered γ' phase ($L1_2$ -type crystal structure, $a = 3.312 \pm 0.077 \text{ \AA}$), a body-centered tetragonal martensite phase ($L1_0$ crystal structure, $a = 3.055 \pm 0.018 \text{ \AA}$, $c = 3.133 \pm 0.020 \text{ \AA}$), and a disordered FCC γ phase ($A1$ crystal structure, $a = 3.718 \pm 0.030 \text{ \AA}$).

TEM analysis was performed on the 100 and 500 h aged samples at 600°C to determine microstructural evolution and phase formation. Fig. 6-2 shows a bright field TEM images and SAED patterns reflecting the microstructures after heat treatments of $600^\circ\text{C}/100 \text{ h}$ and $600^\circ\text{C}/500 \text{ h}$. Fig. 6-2a shows the fine microstructure observed within the heat treated samples. The grain size ranges from 50 to 150nm and is approximately the same for both heat treated cases. Twinning was observed within the $L1_0$ structures similar to what was observed in the

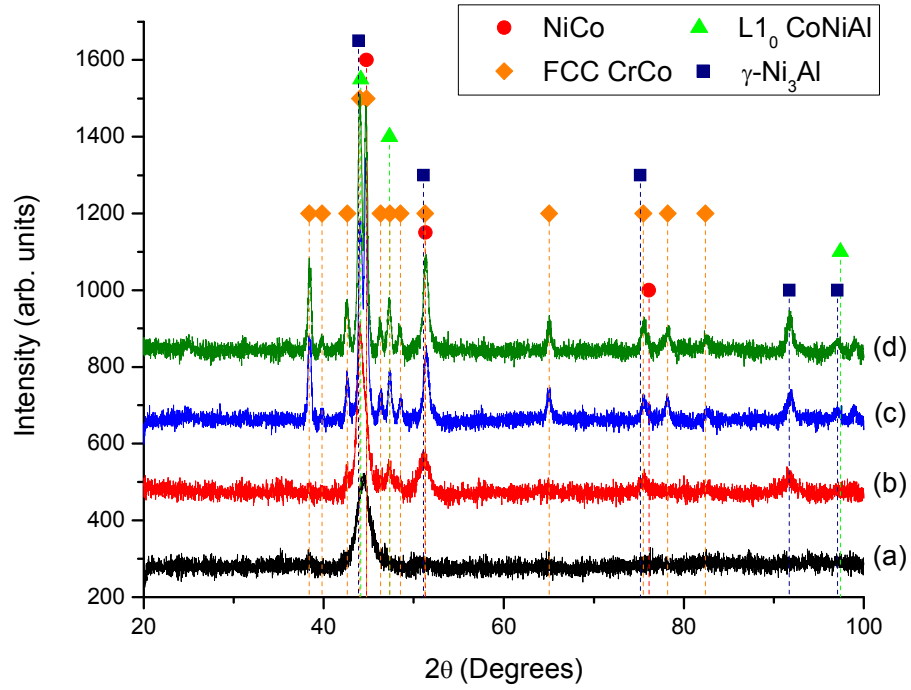


Figure 6-1: XRD patterns for the $\text{Al}_{17}\text{Cr}_{26}\text{Co}_{28}\text{Ni}_{28}\text{Si}_1$ coating on alumina in the as-cast and annealed conditions. (a) As-cast, (b) 600°C/0.25 h, (c) 600°C/100 h, and (d) 600°C/500 h.

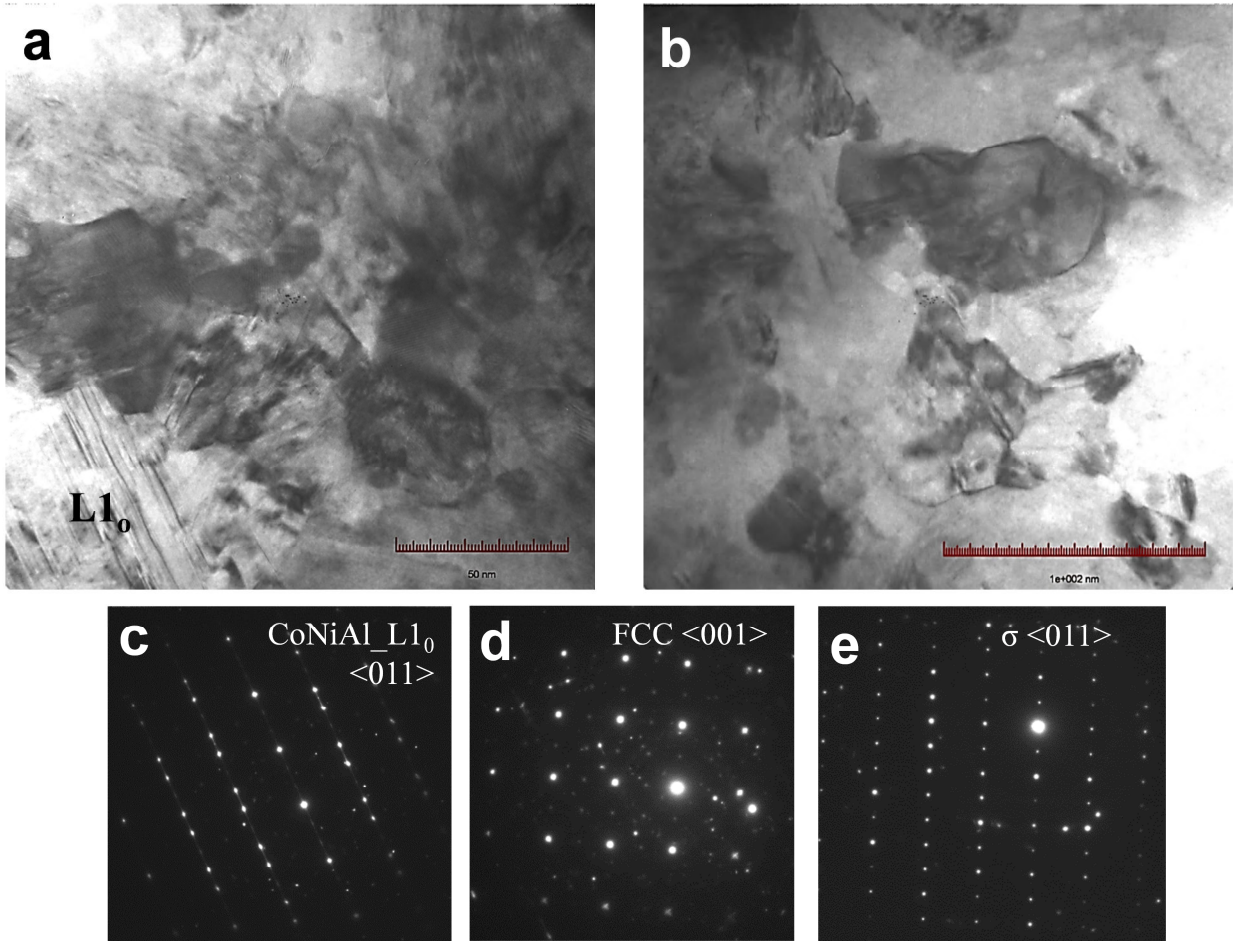


Figure 6-2: Bright Field TEM imaged of microstructure for (a) 600°C/100 h and (b) 600°C/500 h with corresponding SAED patterns for (c) L1₀ with a twinning structure, (d) γ -FCC, and (e) σ phase.

$\text{Al}_{15}\text{Ni}_{35}\text{Cr}_{10}\text{Co}_{35}\text{Si}_5$ bulk alloy described in Chapter 5. Nano-scale precipitation was observed within all grains; however these precipitates could not be identified by TEM analysis.

Fig. 6-3 and Table 6-1 show results from 3-D reconstructions of APT data collected from the 600°C/500 h heat treated specimen. Three runs of at least 18 million ions revealed four main phases: a Cr-rich σ -phase, a Co-rich γ -FCC phase, a Ni/Al rich γ' phase, and Al/Si-rich nano-scale precipitates. The compositions of these phases are summarized in Table 6-1.

Without the benefit of diffraction data, it is difficult if not impossible to quantify the identity of the nano-scale precipitates. However, based on the phase compositions presented in Table 6-1 and previous work on Al-Ni-Si alloys, the Al/Si rich phase could be one of three phases: Al_3Ni , Al_3Ni_2 , or $\text{Al}_6\text{Ni}_3\text{Si}$ [106-108]. Richter *et. al.* investigated the phase formation in Al-Ni-Si alloys with Ni concentrations below 33.3at.%. They discovered the solubility of Si in the Al_3Ni phase to be only 0.7at.%. For this reason the nano-scale precipitates are not believed to be Al_3Ni [106]. The Al_3Ni_2 phase was found to have a much higher solubility for Si (~11.5at.%). However, this phase has a very limited solubility for Ni. Because of this the, Al/Si rich phase are not believed to be Al_3Ni_2 the body centered cubic τ_3 phase ($\text{Al}_6\text{Ni}_3\text{Si}$) as a possibility [106]. One cannot rule out the possibility that a more complex quaternary or quinary phase forms, or that the deposition method used (DC magnetron sputtering) stabilized an otherwise metastable phase. Crystallographic data is needed to fully identify this phase.

The phases observed following heat treatments were compared with those predicted by Thermo-CalcTM modeling. In the specimen that was annealed at 600°C/500 h, the following phases were observed: σ -phase, γ' phase, a body-centered tetragonal L1_0 phase, and a γ phase. These phases match closely with those predicted by Thermo-CalcTM, as can be seen in Fig. 6-4. At 600°C Thermo-CalcTM predicts a B2 phase, FCC_L12 #2 which is the γ' phase, and the σ -

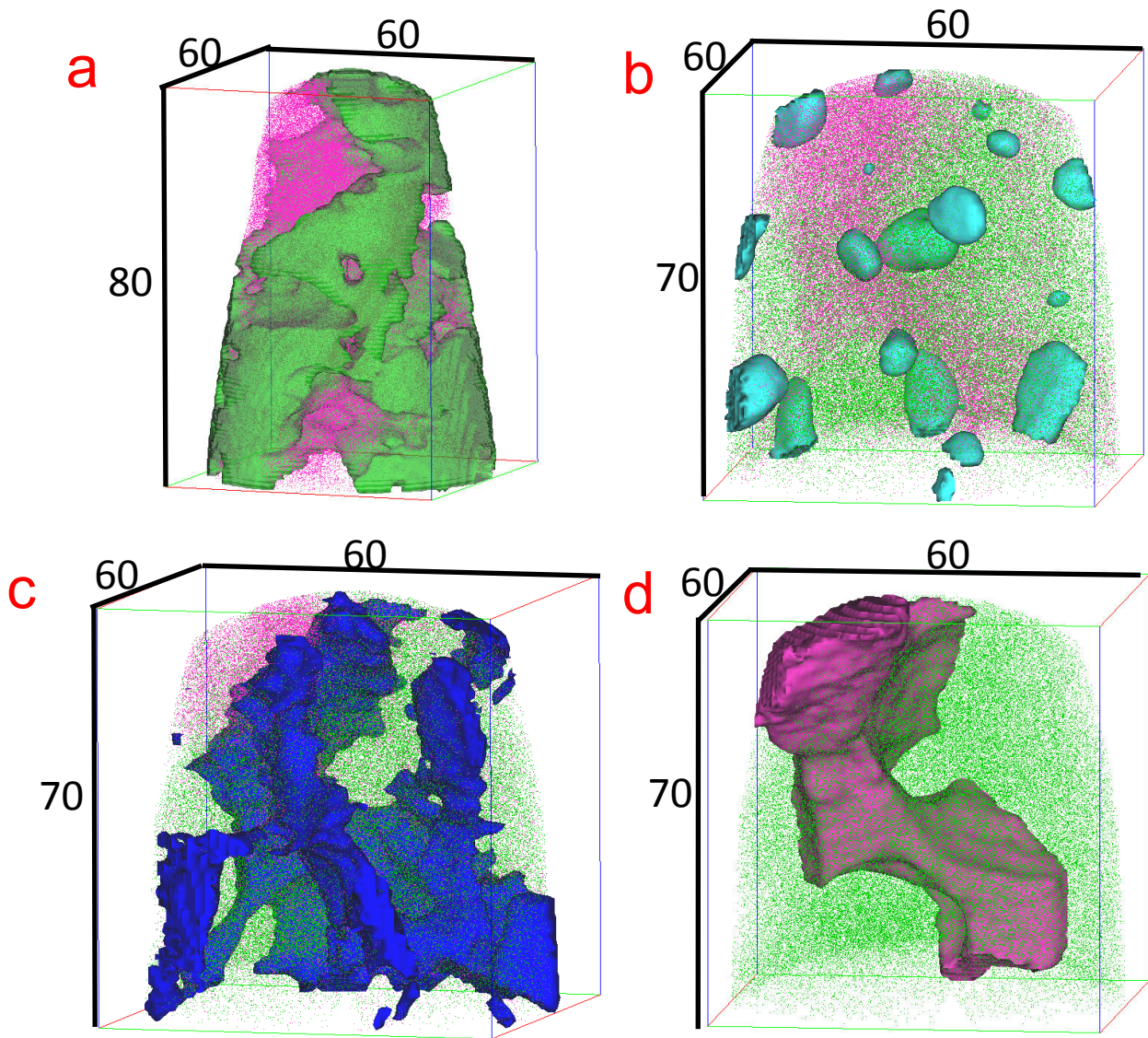


Figure 6-3: 3-D reconstructions of the 4 phases observed within the 600°C/500 hr heat treated coating: (a) γ' -Ni₃Al, (b) τ_3 -Al₆Ni₃Si, (c) γ -NiCo, (d) σ -CrCo. Dimensions are in nm.

Table 6-1: Phase compositions as determined via APT for the sputter deposited coating after annealing at 600°C/500 h.

	Cr-rich σ (Atomic %)	Co-rich γ (Atomic %)	Al-rich ppts. (Atomic %)	Ni/Al-rich γ' Matrix (Atomic %)
Al	1.073 \pm 0.014	4.559 \pm 0.027	53.66 \pm 0.247	23.181 \pm 0.042
Ni	11.235 \pm 0.020	22.923 \pm 0.053	17.223 \pm 0.165	40.849 \pm 0.040
Cr	50.330 \pm 0.072	27.940 \pm 0.054	2.2287 \pm 0.062	10.515 \pm 0.025
Co	34.624 \pm 0.070	43.522 \pm 0.054	6.92 \pm 0.113	23.175 \pm 0.032
Si	2.738 \pm 0.024	1.056 \pm 0.021	19.967 \pm 0.209	2.280 \pm 0.017

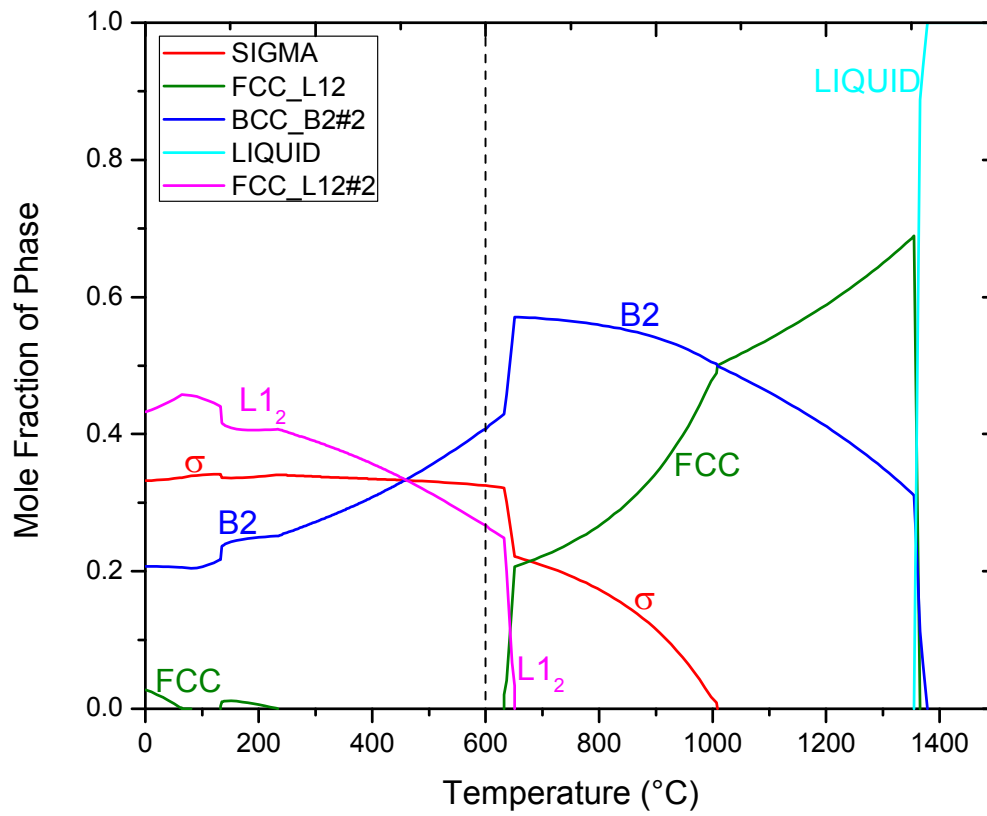


Figure 6-4: Thermo-Calc™ phase predictions for AlNiCrCoSi coatings.

phase. The B2 phase was the only predicted phase not observed within the alloy; however, as was noted in the previous chapter, very Ni/Co-rich B2 phases can transform martensitically upon cooling to L1₀. The FCC_L1₂ (disordered FCC γ -phase) is predicted at higher temperatures, but based on the complex phases often observed within co-sputtered alloys the formation at low temperatures is within reason [109].

6.2 Oxidation Behavior

Isothermal oxidation tests were performed on coatings that were deposited on a pure Ni substrates and CMSX-4 substrates. These tests were conducted at 1050°C in laboratory air for times ranging from 5 h to 240 h. A pure Ni substrate was also oxidized to provide a reference for the mass changes that occurred during oxidation. The results (Fig. 6-5) show a significant improvement in oxidation behavior when the HEA coating is applied to Ni in comparison to the uncoated substrate. Further improvement was observed when the coating was applied to CMXS-4; however this was not surprising in than CMSX-4 which is a second generation superalloy is more oxidation resistant than pure Ni. Fig. 6-6 shows XRD results for the isothermal oxidation steps on CMSX-4. The results show the as-deposited coating to be single phase with an FCC crystal structure. Oxidation resulted in the formation of chromia and alumina peaks which increased in size with increasing oxidation time.

Fig. 6-7 shows cross sectional SEM backscattered electron images for coatings deposited on CMSX-4 substrates that were isothermally oxidized at 1050°C. The coating formed a thick alumina scale after just 5 h of oxidation. Some internal oxidation was observed. Similar observations have been made in sputter deposited and electron beam deposited NiAl coatings and are attributed to rapid oxygen transport along columnar grain boundaries during processing

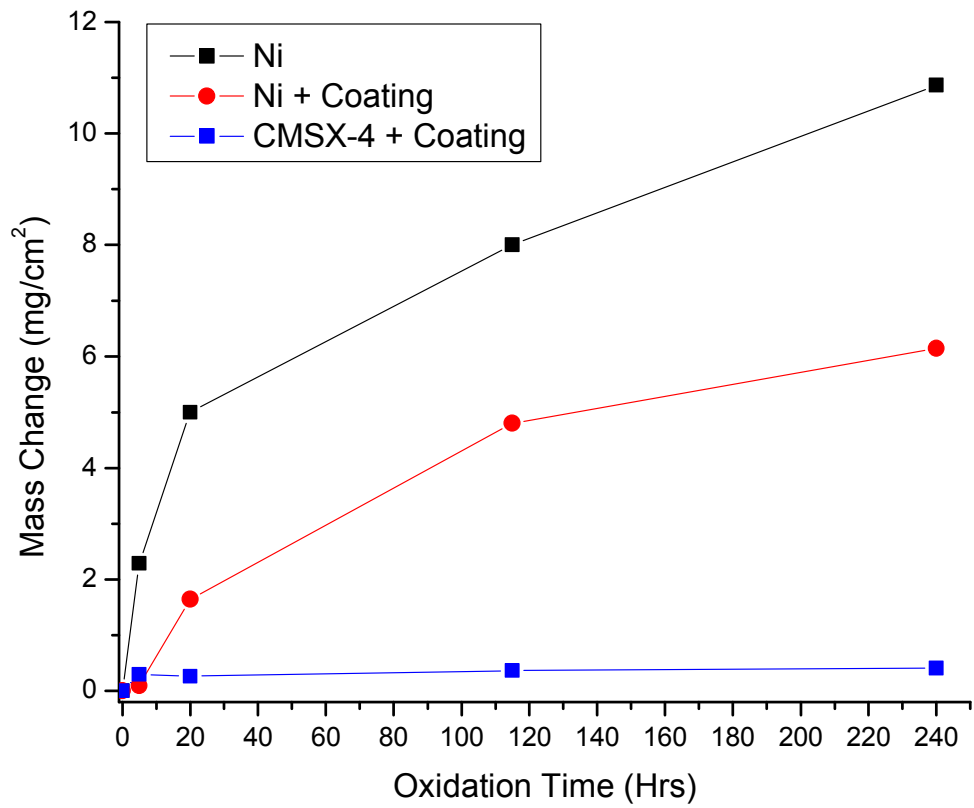


Figure 6-5: Mass change for oxidation time for pure Ni, Ni+HEA coating, CMSX-4 + HEA coating.

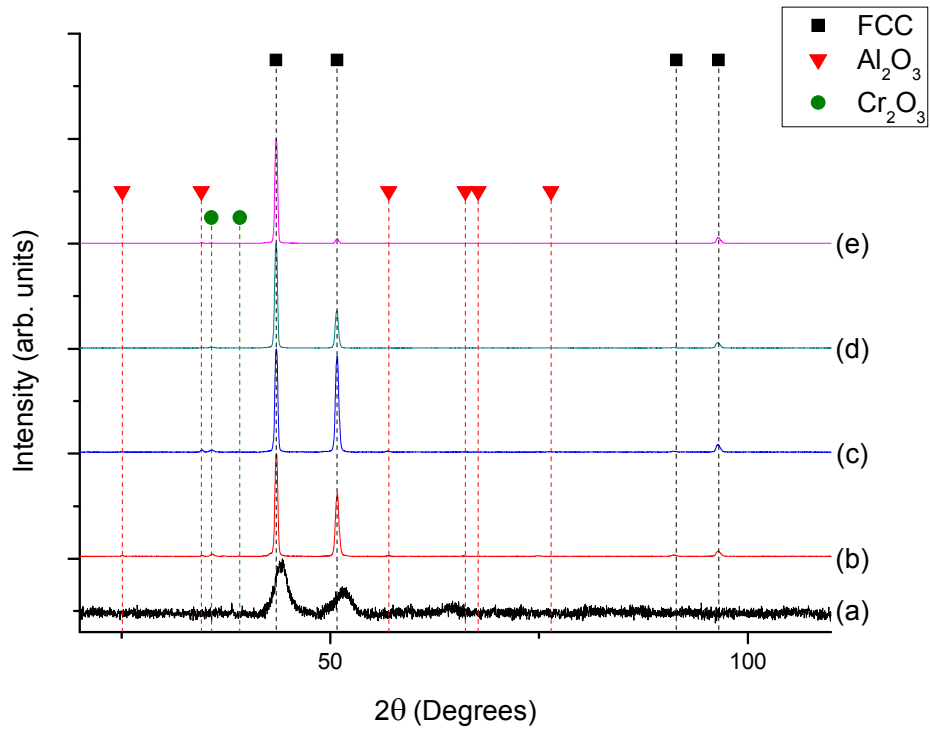


Figure 6-6: XRD patterns for the $\text{Al}_{17}\text{Cr}_{26}\text{Co}_{28}\text{Ni}_{28}\text{Si}_1$ coating on CMSX-4 in the as-cast and oxidized states: (a) As-cast, (b) $600^\circ\text{C}/0.25$ h, (c) $600^\circ\text{C}/100$ h, and (d) $600^\circ\text{C}/500$ h.

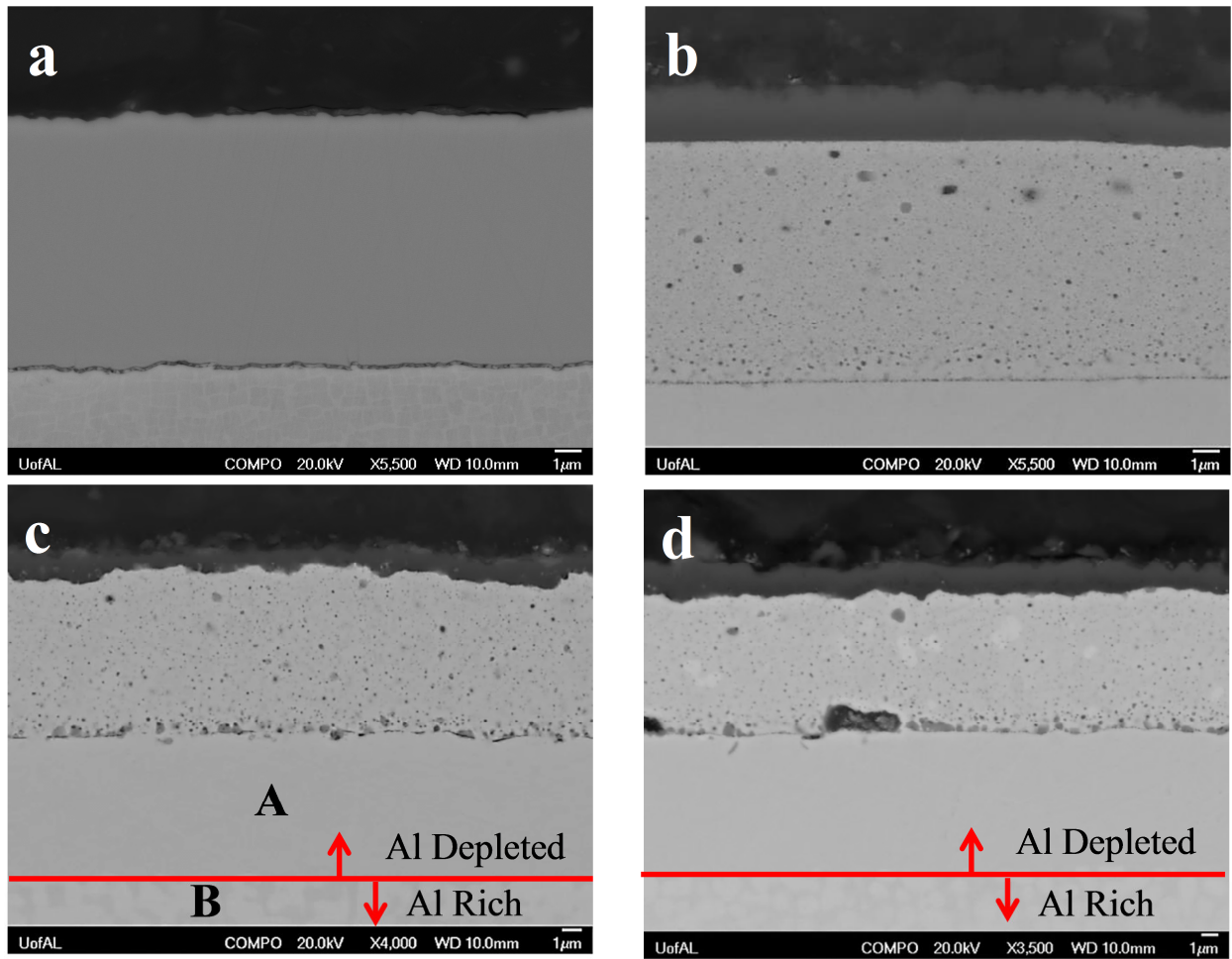


Figure 6-7: Backscattered electron SEM images the isothermal oxidation test performed on CMSX-4 for: (a) As-deposited, (b) 5 h oxidation, (c) 115 h oxidation, (d) 240 h oxidation

or during oxidation [110,111]. The formation of the alumina scale resulted in a drop of over 6 at.% in Al within the coating matrix from the as-deposited alloy. The matrix composition for each oxidation step is reported in Table 6-2. As oxidation time increased, the thickness of the oxide, 1.85 μm after 5 h to 2.05 μm after 240 h, and Al concentration, 9.65 at. % after 5 h and 8.45 at. % after 240 h, within the matrix varied only slightly from those observed after 5 h of oxidation. An Al depleted zone within the CMSX-4 substrate was observed after each isothermal oxidation step, starting below the coating substrate interface and progressing further into the CMSX-4, with composition variations reported in Table 6-3. There was also significant Cr and Co enrichment within this region. The thickness of the aluminum depleted layer did increase with oxidation time resulting from aluminum diffusing to the coating to stabilize the oxide scale.

Fig. 6-8 shows a comparison between previously studied β -NiAl+Cr+Zr/Hf coatings and the HEA coating investigated in this study. The HEA coatings were deposited on CMSX-4. The β -NiAl coating were also isothermally oxidized at 1050°C, but were 20 μm thicker and were deposited on the Ni-based superalloy Rene-N5 which is similar in composition but which is more oxidation resistant than CMSX-4. It is anticipated that the performance of the HEA coating could be improved by the development of optimized annealing schemes. However, this qualitative comparison shows the promise of HEAs for use as high temperature coatings.

6.3 Conclusions

An AlNiCrCoSi multi-component alloy was prepared via DC Magnetron sputtering. The deposition was performed using four targets and stage rotation. This resulted in dense columnar

Table 6-2: Coating composition after each step of isothermal oxidation at 1050°C.

Element	As-Deposited (Atomic %)	5 h (Atomic %)	20 h (Atomic %)	115 h (Atomic %)	240 h (Atomic %)
Al	16.17 ± 0.04	9.65	10.16	8.46	8.45
Co	0.85 ± 0.07	25.47	22.81	20.26	19.16
Ni	26.17 ± 0.07	38.85	43.97	50.80	51.68
Si/W/Ta	28.23 ± 0.16	2.94	1.92	2.58	2.90
Cr	28.58 ± 0.16	23.09	21.15	18.68	17.82

Table 6-3: Composition of Al depleted zone and Al rich zone within CMSX-4.

Element	A (Atomic %)	B (Atomic %)
Al	7.18	13.45
Ni	51.58	58.11
Co	20.17	11.60
Cr	18.36	7.21

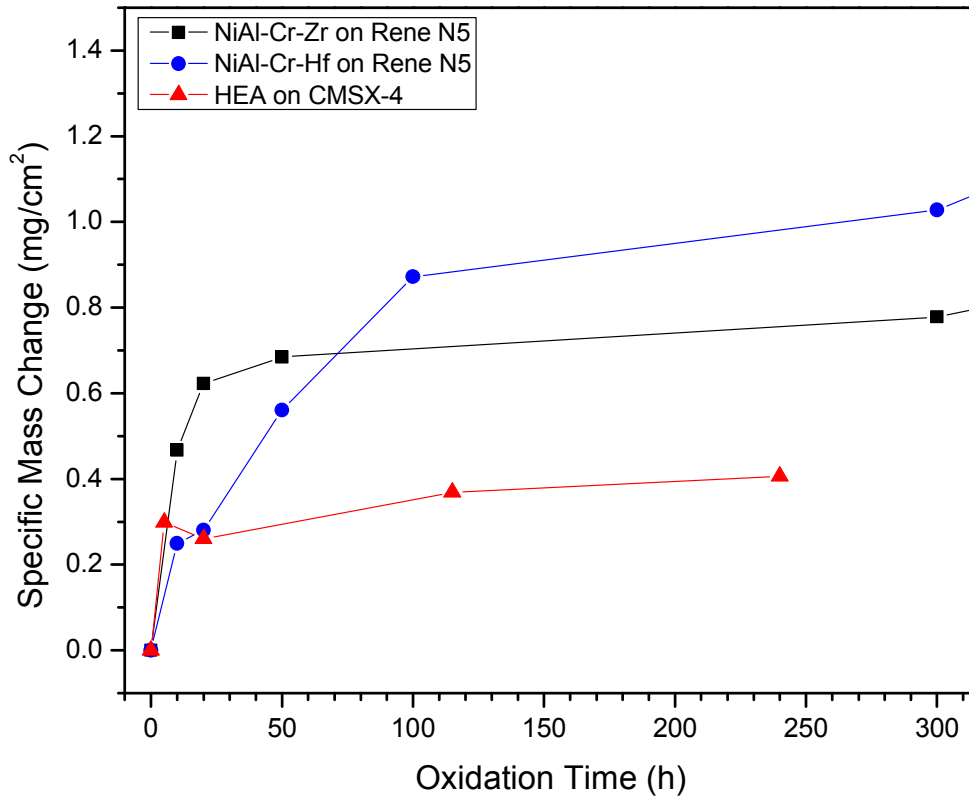


Figure 6-8: A comparison of previously studied β -NiAl+Cr+Zr/Hf coatings to the HEA coating produced in this study. Isothermal oxidation at 1050°C.

microstructure and approximately a 10 μ m thick coating. Aging and isothermal oxidation test were performed on the coatings which revealed the following:

- (1) Aging at 600°C resulted in the formation four main phases: tetragonal σ phase, an ordered γ' phase, a body-centered tetragonal $L1_0$ phase, and a γ - FCC phase. Nano-scale precipitation rich in Al and Si was also observed after atom probe analysis. The precipitates are believed to be a variant of Al_6Ni_3Si or some higher order intermetallic phase.
- (2) Isothermal oxidation test were performed at 1050°C for times ranging from 5 h to 240 h. The oxidation resulted in a typical parabolic mass curve, but showed significant improvement in oxidation behavior when comparing the HEA coating on Ni/CMSX-4 to pure Ni. The tests resulted in the formation of a dense alumina scale and the depletion of Al within the matrix. This resulted in a single phase FCC matrix and an in an Al depleted zone within the CMSX-4 substrate.
- (3) When compared to previously studies β -NiAl coatings the parabolic mass gain was improved. This is likely the result of the formation of a thicker and denser alumina scale than that observed within the β -NiAl coatings.

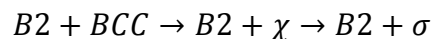
7. GENERAL DISCUSSION AND CONCLUSIONS

7.1 Summary and Discussion of Work

Two bulk HEAs were designed using the criteria proposed by X. Yang and Y. Zhang [7]. This model takes into account the effects of ΔS_{mix} and ΔH_{mix} with the atomic size difference to determine the phase formation of the alloy. The model builds upon the first rules of phase formation prediction presented by Zhang *et. al.* [32]. Based on the equations presented in Chapter 2, the alloys fall within the solid solution/intermetallic region. This region was selected to promote precipitation hardening. The two alloys were composed of Ni-Al-Cr-Co-Si with varying atomic percents. The constituents were selected because of their use in Ni-based alloys and high temperature applications. A coating was also prepared to provide insight into the similarities between the coating and bulk alloy.

The $\text{Al}_{20}\text{Ni}_{25}\text{Cr}_{25}\text{Co}_{25}\text{Si}_5$ bulk alloy was found to have dendritic microstructure after casting. The dendritic region was composed of a B2 matrix with disordered BCC platelets that exhibited a cube-on-cube orientation relationship and a γ/γ' -like structure. Based on APT and TEM SAED analysis, the platelets were determined to be α -Cr. The inter-dendritic region was found to consist of a Cr-rich σ -phase interspersed with a semi-continuous B2 phase.

The as-cast specimens were then heat treated at 600°C, 700°C, and 900°C to determine the effects of annealing on the microstructure. After short periods of aging, the dendritic region underwent the following transformation:



The χ -phase precipitation exhibited a similar cube on cube orientation to that of the α -Cr. As aging time was increased the metastable χ -phase acted as a nucleation site for σ -phase precipitation, as previously discussed in Chapter 4. Additional γ -FCC phase was also observed via TEM.

The $\text{Al}_{15}\text{Ni}_{35}\text{Cr}_{10}\text{Co}_{35}\text{Si}_5$ alloy contained a vastly different microstructure. The as-cast specimen was composed of two main phases: a twinned L1_0 -AlNiCo phase and a γ -FCC phase with ordered γ' precipitation. These phases remained constant during aging except at 600°C , where G-phase precipitation was observed for aging times under 20 h.

The oxidation behavior of the alloys was also examined through a series of isothermal and stepped/sequential oxidation tests. The $\text{Al}_{20}\text{Ni}_{25}\text{Cr}_{25}\text{Co}_{25}\text{Si}_5$ alloy was found to form a compact alumina scale during isothermal oxidation that grew with increasing aging time. During the isothermal oxidation tests very little mass change was observed. The stepped/sequential oxidation resulted in the formation of a chromia scale with an underlying alumina scale. For both the stepped/sequential and isothermal oxidation tests, three main phases were observed: a B2 phase, a Cr-rich σ -phase, and a γ -FCC phase. Nano-scale precipitates were detected within the dendritic regions via APT and determined to be the σ phase. The γ -FCC phase formed predominately below the oxide scale as a result of aluminum depletion within the alloy.

Isothermal oxidation of the as-cast $\text{Al}_{15}\text{Ni}_{35}\text{Cr}_{10}\text{Co}_{35}\text{Si}_5$ alloy also resulted in the formation of a coherent alumina scale. Similar to the $\text{Al}_{20}\text{Ni}_{25}\text{Cr}_{25}\text{Co}_{25}\text{Si}_5$ alloy little to no mass change was observed during oxidation, but spallation of the oxide scale did occur after extended periods of oxidation. The formation of voids below the oxide was also observed as a result of Cr and Al depletion within the alloy. The stepped/sequential oxidation of this alloy resulted in the formation of alumina and chromia scales. Areas absent of an oxide scale were also observed

resulting from spallation of the scale. The oxidized alloy contained the same phases observed after casting: a twinned $L1_0$ -AlNiCo phase, a disordered γ -FCC phase, and an ordered γ' precipitate phase.

Based on the results from the bulk alloys, an $Al_{17}Ni_{28}Cr_{26}Co_{28}Si_1$ coating was produced using DC magnetron sputtering. The coatings were annealed at 600°C for varying times to assess microstructural evolution. The as-deposited coating was single phase with a metastable FCC crystal structure. Annealing resulted in the formation of four main phases: a σ phase, an ordered γ' phase, a body-centered tetragonal $L1_0$ phase, and a γ - FCC phase. Nano scale precipitates that were rich in Al and Si were also observed. They could not be identified but are believed to be either τ_3 Al_6Ni_3Si or some higher order intermetallic phase.

The coating was also deposited on pure Ni and Ni-based superalloy CMSX-4 and put through a series of isothermal oxidation tests to determine the oxidation behavior of the alloy. The oxidation resulted in the formation of a compact alumina scale that increased in thickness with increased oxidation time. The oxidation resulted in a typical parabolic mass gain curve, but when comparing the coated Ni to the pure Ni, vast improvement in mass gains were observed. Further improvements were observed in terms of mass gain when the AlNiCrCoSi alloy was deposited on CMSX-4. The oxidation resulted in the formation of a single phase FCC microstructure.

The previously discussed results provide insight into the phase formation rules for HEAs. Both alloys were designed to fall within the solid solution intermetallic region based on their atomic size difference and the enthalpy and entropy of mixing. This region is defined by the possibility of a simple solid solution formation or the formation of a solid solution with ordered intermetallic precipitates. For the $Al_{20}Ni_{25}Cr_{25}Co_{25}Si_5$ bulk alloy this criterion was not met. The

ordered B2 phase contained intermetallic precipitates but a second intermetallic main phase was also formed. The $\text{Al}_{15}\text{Ni}_{35}\text{Cr}_{10}\text{Co}_{35}\text{Si}_5$ bulk alloy also fell outside this criterion. A simple FCC phase was formed but included ordered FCC precipitates within the phase and a complex martensitic phase was formed. Based on these results further refinement of phase prediction rules are needed or other considerations must be made when selecting alloying elements. As was noted by Guo *et. al.*, a highly negative enthalpy of mixing between elements can result in unwanted phase formation, such as intermetallic compounds instead of a solid solution [16]. However, the precipitation of these intermetallic phases are also the cause for the favorable wear resistances exhibited by HEAs and similar multicomponent alloys.

This study also provides insight into the effect of composition on phase formation and oxidation behavior in HEA systems. Phase differences between the two bulk alloys were expected because of the significant differences in Co, Ni, Al and Cr contents in the investigated alloys. It is well known that Ni and Co stabilize FCC phases whereas higher concentrations of Al stabilize BCC and B2 phases. What is of interest is the lack of significant intermetallic precipitation in the $\text{Al}_{15}\text{Ni}_{35}\text{Cr}_{10}\text{Co}_{35}\text{Si}_5$ alloy because of the high concentration of Si, which resulted in many intermetallic compounds in the $\text{Al}_{20}\text{Ni}_{25}\text{Cr}_{25}\text{Co}_{25}\text{Si}_5$ alloy. The Si in the $\text{Al}_{15}\text{Ni}_{35}\text{Cr}_{10}\text{Co}_{35}\text{Si}_5$ alloy went into solution with the two main phases unlike in the $\text{Al}_{20}\text{Ni}_{25}\text{Cr}_{25}\text{Co}_{25}\text{Si}_5$ alloy where it showed a preference to the Cr and Co rich phases.

In terms of oxidation behavior, the study shows the importance of Cr in high temperature oxidation. The lack of Cr and Al in the $\text{Al}_{15}\text{Ni}_{35}\text{Cr}_{10}\text{Co}_{35}\text{Si}_5$ alloy resulted in increased stress within the oxide scale and spallation. This also led to void formation underneath the oxide scale. The oxidation of the $\text{Al}_{20}\text{Ni}_{25}\text{Cr}_{25}\text{Co}_{25}\text{Si}_5$ alloy formed a similar FCC phase below the oxide scale

but the higher concentration of Al and Cr stabilized the scale resulting in a dense continuous oxide.

The results also provide understanding into the similarities between bulk multi-component alloys and compositionally similar coatings. Although the coating was not the exact composition of the $\text{Al}_{20}\text{Ni}_{25}\text{Cr}_{25}\text{Co}_{25}\text{Si}_5$ alloy, many similar phases were observed. The phases that differed, such as Ni_3Al instead of NiAl , were expected because of the slightly lower aluminum and silicon concentrations combined with the higher nickel, cobalt, and chromium concentrations. Although there were many similarities in the main phases, the precipitation of the $\text{Al}_6\text{Ni}_3\text{Si}$ phase, which was not observed within the bulk alloy, shows complexity of phase formation within coatings and the difficulty of correlation properties and microstructural evolution between the two.

7.2 Conclusions

The goal of this study was to provide a better understanding of the possible use of HEAs in high temperature environments either as a coating or bulk alloy. The study also hoped to provide insight into the correlation between phase formations in bulk alloys and sputter deposited coatings. The results from the $\text{Al}_{20}\text{Ni}_{25}\text{Cr}_{25}\text{Co}_{25}\text{Si}_5$ alloy show the promise of the select alloy for use in high temperatures because of its oxidation behavior and unique chromia and alumina oxide formation. The alloy formed a continuous oxide scale and little internal oxidation was observed after extensive isothermal oxidation. The alloy was also found to have a high hardness, which is favorable, however, a better understanding of its mechanical behavior is required.

The $\text{Al}_{15}\text{Ni}_{35}\text{Cr}_{10}\text{Co}_{35}\text{Si}_5$ alloy revealed the effects of concentration on phase formation and oxidation behavior. The $\text{Al}_{15}\text{Ni}_{35}\text{Cr}_{10}\text{Co}_{35}\text{Si}_5$ alloy did not form intermetallic precipitates, as seen in the $\text{Al}_{20}\text{Ni}_{25}\text{Cr}_{25}\text{Co}_{25}\text{Si}_5$ alloy, except the metastable G-phase for short annealing times. This is believed to be the result of a higher solubility of Si within the martensitic and FCC phases. The decrease in Al and Cr, when compared to the $\text{Al}_{20}\text{Ni}_{25}\text{Cr}_{25}\text{Co}_{25}\text{Si}_5$ alloy, resulted in a discontinuous oxide scale that was composed of alumina and chromia. The decrease resulted in spallation of the scale and void formation underneath the scale, which was not observed in the $\text{Al}_{20}\text{Ni}_{25}\text{Cr}_{25}\text{Co}_{25}\text{Si}_5$ alloy.

The $\text{Al}_{17}\text{Ni}_{28}\text{Cr}_{26}\text{Co}_{28}\text{Si}_1$ coating also shows promise of use in high temperature applications. The coating formed a continuous alumina scale after short periods of isothermal oxidation that was stable for oxidation time up to 240 h. The coating also exhibited lower mass gains than thicker β -NiAl based coatings deposited on more oxidation resistant substrates. The coating also provided a better understanding of the correlation between the bulk alloy phase formation and the coating counterpart. Although a coating with a composition closer to that of the alloy is needed to fully understand the correlation, similar phases were observed in both alloys and those that differ were expected because of the variation in concentration.

7.3 Suggestions for Future Work

Expansion on the presented research should include an investigation into the wear behavior of the $\text{Al}_{20}\text{Ni}_{25}\text{Cr}_{25}\text{Co}_{25}\text{Si}_5$ and $\text{Al}_{15}\text{Ni}_{35}\text{Cr}_{15}\text{Co}_{35}\text{Si}_5$ alloys and nanoindentation to better determine the hardness of each phase. A detailed cyclic oxidation study would also be beneficial to better understand the oxidation kinetics. Depending on the proposed application it may also

be beneficial to change the oxidation environment, such as adding steam or using ash during the oxidation test.

An investigation into the effects of constituent substitution is also need for the two alloys. For example replacing Cr or Si with another element of similar atomic size but that has a lower enthalpy of mixing with the other elements, such as Mo or Hf respectively. This will move the alloy closer to the predicted solid solution region and provide insight into the driving force behind the phase formation in these complex alloys. Similar oxidation and annealing tests should be performed to compare microstructural evolution and oxidation behavior. This will also provide a comparison between a solid solution HEA and the multi-component HEA investigated in this research.

For the coating aspect, it is desired to have a coating closer to that of the $\text{Al}_{20}\text{Ni}_{25}\text{Cr}_{25}\text{Co}_{25}\text{Si}_5$ alloy. This will provide a more accurate comparison between bulk alloy phases and those observed within the coating. Cyclic oxidation test and higher temperature annealing is also desired to obtain a better understanding of the oxidation behavior and phase formation at high temperatures. In term of mechanical property comparison, nanoindentation and wear testing of the coatings are also desired to provide a more in depth understanding of the mechanical properties and how they compare to the bulk alloy counterpart.

A detailed investigation into how varying deposition parameters, such as temperature, pressure and rotation speed, influence the microstructures and mechanical properties of the coating is also desired. It is well known that these factors play a large role in coating microstructure which affects the overall properties. An example design of experiments is presented in table 7-1 showing the different tests that could be performed to better understand these effects. Results would provide a way of optimizing deposition parameters to achieve a

coating with the best oxidation behavior and mechanical properties. Other avenues for investigation include the influences of heat treatments prior to oxidation. The results of this study show that heat treatment can dramatically alter the phase distributions within these alloys.

Table 7-1: Design of Experiments to determine optimum sputtering conditions

StdOrder	RunOrder	Temperature (°C)	Pressure (mTorr)	Rotation (RPM)
15	1	525	6	13.5
6	2	700	2	25
7	3	350	10	25
13	4	525	6	13.5
5	5	350	2	25
4	6	700	10	2
9	7	525	6	13.5
10	8	525	6	13.5
12	9	525	6	13.5
11	10	525	6	13.5
2	11	700	2	2
1	12	350	2	2
8	13	700	10	25
16	14	525	6	13.5
14	15	525	6	13.5
3	16	350	10	2

REFERENCES

- [1] H. K. Zeytin and A. Tekin, "Effect of microstructure on hardness and wear resistance of a silicon modified Cr-Ni-Co superalloy," *High Temperature Materials and Processes* 19 (2000) 17-23.
- [2] H. K. Zeytin and A. Tekin, "SEM and TEM investigations on a Cr-Ni-Co superalloy," *High Temperature Materials and Processes* 19 (2000) 135-140.
- [3] H. K. Zeytin, A. A. Kaya and A. Tekin, "Microstructural evolution in a Ni-Cr-Co based superalloy during cooling from the melt," *Materials Characterization* 57 (2006) 86-93.
- [4] J. R. Nicholls, "Designing oxidation-resistant coatings," *JOM* 52 (2000) 28-35.
- [5] J. R. Nicholls, "Advances in coating design for high-performance gas turbines," *MRS Bulletin* 28 (2003) 659-670.
- [6] S. Bose, High Temperature Coatings, (Butterworth-Heinemann, Burlington, MA, 2007).
- [7] X. Yang and Y. Zhang, "Prediction of high-entropy stabilized solid-solution in multi-component alloys," *Materials Chemistry and Physics* 132 (2012) 233-238.
- [8] W.-H. Wu, C.-C. Yang and J.-W. Yeh, "Industrial Development of High-Entropy Alloys," *Annales de chimie Science des matériaux* 31 (2006) 737-747.
- [9] J. W. Yeh, Y. L. Chen, S. J. Lin and S. K. Chen, "High-Entropy Alloys - A New Era of Exploitation," *Materials Science Forum* 560 (2007) 1-9.
- [10] J. W. Yeh, S. K. Chen, S. J. Lin, J. Y. Gan, T. S. Chin, T. T. Shun, C. H. Tsau and S. Y. Chang, "Nanostructured high-entropy alloys with multiple principal elements: Novel alloy design concepts and outcomes," *Advanced Engineering Materials* 6 (2004) 299-303.
- [11] B. Cantor, I. T. H. Chang, P. Knight and A. J. B. Vincent, "Microstructural development in equiatomic multicomponent alloys," *Materials Science and Engineering: A* 375-377 (2004) 213-218.
- [12] Y. Zhang and Z. Yunjun, "Solid Solution Formation Criteria for High Entropy Alloys," *Materials Science Forum* 561-565 (2007) 1337-1339.
- [13] S. Guo and C. T. Liu, "Phase stability in high entropy alloys: Formation of solid-solution phase or amorphous phase," *Progress in Natural Science: Materials International* 21 (2011) 433-446.

- [14] Y. Zhang, Y. J. Zhou, J. P. Lin, G. L. Chen and P. K. Liaw, "Solid-Solution Phase Formation Rules for Multi-component Alloys," *Advanced Engineering Materials* 10 (2008) 534-538.
- [15] P. K. Huang, J. W. Yeh, T. T. Shun and S. K. Chen, "Multi-Principal-Element Alloys with Improved Oxidation and Wear Resistance for Thermal Spray Coating," *Advanced Engineering Materials* 6 (2004) 74-78.
- [16] T.-T. Shun, C.-H. Hung and C.-F. Lee, "Formation of ordered/disordered nanoparticles in FCC high entropy alloys," *Journal of Alloys and Compounds* 493 (2010) 105-109.
- [17] J. M. Zhu, H. M. Fu, H. F. Zhang, A. M. Wang, H. Li and Z. Q. Hu, "Synthesis and properties of multiprincipal component AlCoCrFeNiSi_x alloys," *Materials Science and Engineering: A* 527 (2010) 7210-7214.
- [18] A. Cunliffe, J. Plummer, I. Figueroa and I. Todd, "Glass formation in a high entropy alloy system by design," *Intermetallics* 23 (2012) 204-207.
- [19] S. Guo, Q. Hu, C. Ng and C. T. Liu, "More than entropy in high-entropy alloys: Forming solid solutions or amorphous phase," *Intermetallics* 41 (2013) 96-103.
- [20] Y. Zhang, X. Yang and P. K. Liaw, "Alloy Design and Properties Optimization of High-Entropy Alloys," *JOM* 64 (2012) 830-838.
- [21] M.-H. Tsai, K.-Y. Tsai, C.-W. Tsai, C. Lee, C.-C. Juan and J.-W. Yeh, "Criterion for Sigma Phase Formation in Cr- and V-Containing High-Entropy Alloys," *Materials Research Letters* 1 (2013) 207-212.
- [22] S.-T. Chen, W.-Y. Tang, Y.-F. Kuo, S.-Y. Chen, C.-H. Tsau, T.-T. Shun and J.-W. Yeh, "Microstructure and properties of age-hardenable Al_xCrFe_{1.5}MnNi_{0.5} alloys," *Materials Science and Engineering A* 527 (2010) 5818-5825.
- [23] C. Huang, Y. Zhang, J. Shen and R. Vilar, "Thermal stability and oxidation resistance of laser clad TiVCrAlSi high entropy alloy coatings on Ti-6Al-4V alloy," *Surface and Coatings Technology* 206 (2011) 1389-1395.
- [24] J. Jiang and X. Luo, "High temperature oxidation behaviour of AlCuTiFeNiCr high-entropy alloy," *Advanced Materials Research* 652-654 (2013) 1115-1118.
- [25] O. N. Senkov, S. V. Senkova, D. M. Dimiduk, C. Woodward and D. B. Miracle, "Oxidation behavior of a refractory NbCrMo_{0.5}Ta_{0.5}TiZr alloy," *Journal of Materials Science* 47 (2012) 6522-6534.
- [26] G. B. Gibbs and R. Hales, "The influence of metal lattice vacancies on the oxidation of high temperature materials," *Corrosion Science* 17 (1977) 487-507.
- [27] A. Takeuchi and A. Inoue, "Classification of bulk metallic glasses by atomic size difference, heat of mixing and period of constituent elements and its application to

- characterization of hte main alloying element," *Materials Transactions* 46 (2005) 2817-2829.
- [28] S. Guo, C. Ng, J. Lu and C. T. Liu, "Effect of valence electron concentration on stability of fcc or bcc phase in high entropy alloys," *Journal of Applied Physics* 109 (2011) 103505.
- [29] F. Otto, Y. Yang, H. Bei and E. P. George, "Relative effects of enthalpy and entropy on the phase stability of equiatomic high-entropy alloys," *Acta Materialia* 61 (2013) 2628-2638.
- [30] A. Manzoni, H. Daoud, S. Mondal, S. van Smaalen, R. Völkl, U. Glatzel and N. Wanderka, "Investigation of phases in Al₂₃Co₁₅Cr₂₃Cu₈Fe₁₅Ni₁₆ and Al₈Co₁₇Cr₁₇Cu₈Fe₁₇Ni₃₃ high entropy alloys and comparison with equilibrium phases predicted by Thermo-Calc," *Journal of Alloys and Compounds* 552 (2013) 430-436.
- [31] C. Ng, S. Guo, J. Luan, S. Shi and C. T. Liu, "Entropy-driven phase stability and slow diffusion kinetics in an Al_{0.5}CoCrCuFeNi high entropy alloy," *Intermetallics* 31 (2012) 165-172.
- [32] C. Zhang, F. Zhang, S. Chen and W. Cao, "Computational Thermodynamics Aided High-Entropy Alloy Design," *JOM* 64 (2012) 839-845.
- [33] N. Saunders and A. P. Miodownik, CALPHAD (Calculation of Phase Diagrams): A Comprehensive Guide, (Pergamon Press, Oxford, 1998).
- [34] H. J. Grabke, M. W. Brumm and B. Wagemann, "The Oxidation of NiAl," *Materials and Corrosion* 47 (1996) 675-677.
- [35] M.-H. Chuang, M.-H. Tsai, W.-R. Wang, S.-J. Lin and J.-W. Yeh, "Microstructure and wear behavior of Al_xCo_{1.5}CrFeNi_{1.5}Ti_y high-entropy alloys," *Acta Materialia* 59 (2011) 6308-6317.
- [36] V. Dolique, A. L. Thomann, P. Brault, Y. Tessier and P. Gillon, "Thermal stability of AlCoCrCuFeNi high entropy alloy thin films studied by in-situ XRD analysis," *Surface and Coatings Technology* 204 (2010) 1989-1992.
- [37] C. Li, J. C. Li, M. Zhao and Q. Jiang, "Effect of alloying elements on microstructure and properties of multiprincipal elements high-entropy alloys," *Journal of Alloys and Compounds* 475 (2009) 752-757.
- [38] M.-H. Tsai, H. Yuan, G. Cheng, W. Xu, W. W. Jian, M.-H. Chuang, C.-C. Juan, A.-C. Yeh, S.-J. Lin and Y. Zhu, "Significant hardening due to the formation of a sigma phase matrix in a high entropy alloy," *Intermetallics* 33 (2013) 81-86.
- [39] A. Manzoni, H. Daoud, R. Völkl, U. Glatzel and N. Wanderka, "Phase separation in equiatomic AlCoCrFeNi high-entropy alloy," *Ultramicroscopy* in press (2013).

- [40] I. Baker, H. Wu, X. Wu, M. K. Miller and P. R. Munroe, "The microstructure of near-equiatomic B2/f.c.c. FeNiMnAl alloys," *Materials Characterization* 62 (2011) 952-958.
- [41] S.-T. Chen, W.-Y. Tang, Y.-F. Kuo, S.-Y. Chen, C.-H. Tsau, T.-T. Shun and J.-W. Yeh, "Microstructure and properties of age-hardenable Al_xCrFe_{1.5}MnNi_{0.5} alloys," *Materials Science and Engineering: A* 527 (2010) 5818-5825.
- [42] L. M. Wang, C. C. Chen, J. W. Yeh and S. T. Ke, "The microstructure and strengthening mechanism of thermal spray coating Ni_xCo_{0.6}Fe_{0.2}Cr_ySi_zAlTi_{0.2} high-entropy alloys," *Materials Chemistry and Physics* 126 (2011) 880-885.
- [43] V. Dolique, A. L. Thomann, P. Brault, Y. Tessier and P. Gillon, "Complex structure/composition relationship in thin films of AlCoCrCuFeNi high entropy alloy," *Materials Chemistry and Physics* 117 (2009) 142-147.
- [44] V. Dolique, A. L. Thomann and P. Brault, "High-Entropy Alloys Deposited by Magnetron Sputtering," *Plasma Science, IEEE Transactions on* 39 (2011) 2478-2479.
- [45] W.-R. Wang, W.-L. Wang, S.-C. Wang, Y.-C. Tsai, C.-H. Lai and J.-W. Yeh, "Effects of Al addition on the microstructure and mechanical property of Al_xCoCrFeNi high-entropy alloys," *Intermetallics* 26 (2012) 44-51.
- [46] X. Feng, G. Tang, L. Gu, X. Ma, M. Sun and L. Wang, "Preparation and characterization of TaNbTiW multi-element alloy films," *Applied Surface Science* 261 (2012) 447-453.
- [47] K. Thompson, D. Lawrence, D. J. Larson, J. D. Olson, T. F. Kelly and B. Gorman, "In situ site-specific specimen preparation for atom probe tomography," *Ultramicroscopy* 107 (2007) 131-139.
- [48] D. Tomus and H. P. Ng, "In situ lift-out dedicated techniques using FIB–SEM system for TEM specimen preparation," *Micron* 44 (2013) 115-119.
- [49] M. K. Miller, Atom Probe Tomography: Analysis at the Atomic Level, (Kluwer Academic/Plenum Press, New York, NY, 2000).
- [50] O. C. Hellman, J. Rusing, J. T. Sebastian and D. N. Seidman, "Atom-by-atom chemistry of internal interfaces: simulations and experiments," *Materials Science and Engineering C* 15 (2001) 13-15.
- [51] C. T. Sims, N. S. Stoloff and W. C. Hagel, eds., Superalloys II (John Wiley and Sons, New York, 1987).
- [52] R. C. Reed, The Superalloys Fundamentals and Applications, (Cambridge University Press, Cambridge, UK, 2006).
- [53] O. N. Senkov and D. B. Miracle, "Effect of the atomic size distribution on glass forming ability of amorphous metallic alloys," *Materials Research Bulletin* 36 (2001) 2183-2198.

- [54] J. Liu, H. X. Zheng and J. G. Li, "Effect of solidification rate on microstructure and crystal orientation of ferromagnetic shape memory alloys Co–Ni–Al," *Materials Science and Engineering: A* 438–440 (2006) 1061-1064.
- [55] Y. Shida, G. C. Wood, F. H. Stott, D. P. Whittle and B. D. Bastow, "Intergranular oxidation and internal void formation in Ni-40% Cr alloys," *Corrosion Science* 21 (1981) 581-597.
- [56] F. A. Golightly, F. H. Stott and G. C. Wood, "The influence of yttrium additions on the oxide-scale adhesion to an iron-chromium-aluminum alloy," *Oxidation of Metals* 10 (1976) 163-187.
- [57] D. A. Porter, K. A. Easterling and M. Y. Sherif, Phase Transformations in Metals and Alloys, Third Edition, (CRC Press, Boca Raton, FL, 2009).
- [58] K. P. Gupta, S. B. Rajendraprasad, A. K. Jena and R. C. Sharma, "Co-Cr-Ni system," *Transactions of the Indian Institute of Metals* 37 (1984) 699-701, 703-708.
- [59] F. Fendik, "Improvements in spinodal alloys from past to present," *Materials And Design* 42 (2012) 131-146.
- [60] Y. P. Wang, B. S. Li, M. X. Ren, C. Yang and H. Z. Fu, "Microstructure and compressive properties of AlCrFeCoNi high entropy alloy," *Materials Science and Engineering: A* 491 (2008) 154-158.
- [61] C.-M. Lin and H.-L. Tsai, "Evolution of microstructure, hardness, and corrosion properties of high-entropy Al_{0.5}CoCrFeNi alloy," *Intermetallics* 19 (2011) 288-294.
- [62] C.-J. Tong, Y.-L. Chen, S.-K. Chen, J.-W. Yeh, T.-T. Shun, C.-H. Tsau, S.-J. Lin and S.-Y. Chang, "Microstructure characterization of Al_xCoCrCuFeNi high-entropy alloy system with multiprincipal elements," *Metallurgical and Materials Transactions A: Physical Metallurgy and Materials Science* 36 (2005) 881-893.
- [63] C.-Y. Hsu, T.-S. Sheu, J.-W. Yeh and S.-K. Chen, "Effect of iron content on wear behavior of AlCoCrFexMo_{0.5}Ni high-entropy alloys," *Wear* 268 (2010) 653-659.
- [64] C.-Y. Hsu, C.-C. Juan, W.-R. Wang, T.-S. Sheu, J.-W. Yeh and S.-K. Chen, "On the superior hot hardness and softening resistance of AlCoCr_xFeMo_{0.5}Ni high-entropy alloys," *Materials Science and Engineering: A* 528 (2011) 3581-3588.
- [65] B. S. Li, Y. P. Wang, M. X. Ren, C. Yang and H. Z. Fu, "Effects of Mn, Ti and V on the microstructure and properties of AlCrFeCoNiCu high entropy alloy," *Materials Science and Engineering: A* 498 (2008) 482-486.
- [66] X.-W. Qiu, Y.-P. Zhang, L. He and C.-g. Liu, "Microstructure and corrosion resistance of AlCrFeCuCo high entropy alloy," *Journal of Alloys and Compounds* 549 (2013) 195-199.

- [67] S. Singh, N. Wanderka, B. S. Murty, U. Glatzel and J. Banhart, "Decomposition in multi-component AlCoCrCuFeNi high-entropy alloy," *Acta Materialia* 59 (2011) 182-190.
- [68] S. Singh, N. Wanderka, K. Kiefer, K. Siemensmeyer and J. Banhart, "Effect of decomposition of the Cr–Fe–Co rich phase of AlCoCrCuFeNi high entropy alloy on magnetic properties," *Ultramicroscopy* 111 (2011) 619-622.
- [69] Y. Zhang, S. G. Ma and J. W. Qiao, "Morphology transition from dendrites to equiaxed grains for AlCoCrFeNi high-entropy alloys by copper mold casting and bridgman solidification," *Metallurgical and Materials Transactions* 43 (2012) 2625-2630.
- [70] V. Raghavan, "Al-Cr-Ni (Aluminum-Chromium-Nickel)," *Journal of Phase Equilibria and Diffusion* 27 (2006) 381-388.
- [71] V. Raghavan, "Al-Cr-Ni (Aluminum-Chromium-Nickel)," *Journal of Phase Equilibria and Diffusion* 29 (2008) 175.
- [72] V. Raghavan, "Al-Cr-Ni (Aluminum-Chromium-Nickel)," *Journal of Phase Equilibria and Diffusion* 30 (2009) 61-63.
- [73] V. Raghavan, "Al-Cr-Ni (Aluminum-Chromium-Nickel)," *Journal of Phase Equilibria and Diffusion* 31 (2010) 279-281.
- [74] I. C. I. Okafor and O. N. Carlson, "Equilibrium studies on a chi phase strengthened ferritic alloy," *Metallurgical Transactions A* 9A (1978) 1651-1657.
- [75] T. H. Chen, K. L. Weng and J. R. Yang, "The effect of high-temperature exposure on the microstructural stability and toughness property in a 2205 duplex stainless steel," *Materials Science and Engineering* A338 (2002) 259-270.
- [76] J. Michalska and M. Sozanska, "Qualitative and quantitative analysis of σ and χ phases in 2205 duplex stainless steel," *Materials Characterization* 56 (2006) 355-362.
- [77] D. M. Escriba, E. Materna-Morris, R. L. Plaut and A. F. Padilha, "Chi-phase precipitation in a duplex stainless steel," *Materials Characterization* 60 (2009) 1214-1219.
- [78] A. Kashiwar, N. P. Vennela, S. L. Kamath and R. K. Khatirkar, "Effect of solution annealing temperature on precipitation in 2205 duplex stainless steel," *Materials Characterization* 74 (2012) 55-63.
- [79] J. K. Shin, H. J. Jang, K. W. Cho and C. J. Park, "Effects of sigma and chi phases on the localized corrosion resistance of SR50A super austenitic stainless steel," *Corrosion* 69 (2013) 364-371.
- [80] S. H. Algie and E. O. Hall, "Site ordering in some σ phase structures," *Acta Crystallographica* 20 (1966) 142.

- [81] S. K. Ghosh and S. Mondal, "High temperature ageing behaviour of a duplex stainless steel," *Materials Characterization* 59 (2008) 1776-1783.
- [82] H. K. Zeytin., A. A. Kaya and A. Tekin, "Microstructural evolution in a Ni–Cr–Co based superalloy during cooling from the melt," *Materials Characterization* 57 (2006) 86-93.
- [83] C. Ng, S. Guo, J. Luan, Q. Wang, J. Lu, S. Shi and C. T. Liu, "Phase stability and tensile properties of Co-free Al_{0.5}CrCuFeNi₂ high-entropy alloys," *Journal of Alloys and Compounds* 584 (2014) 530-537.
- [84] C. S. Giggins and F. S. Pettit, "Oxidation of Ni-Cr-Al alloys between 1000°C and 1200°C," *Journal of the Electrochemical Society* 118 (1971) 1782-1790.
- [85] Y. Niu, X. J. Zhang, Y. Wu and F. Gesmundo, "The third-element effect in the oxidation of Ni–xCr–7Al alloys in 1atm O₂ at 900–1000°C," *Corrosion Science* 48 (2006) 4020-4036.
- [86] C. Ng, S. Guo, J. Luan, S. Shi and C. T. Liu, "Entropy-driven phase stability and slow diffusion kinetics in an Al 0.5CoCrCuFeNi high entropy alloy," *Intermetallics* 31 (2012) 165-172.
- [87] S. Guo, C. Ng, J. Lu and C. T. Liu, "Effect of valence electron concentration on stability of fcc or bcc phase in high entropy alloys," *Journal of Applied Physics* 109 (2011).
- [88] J. Liu and J. G. Li, "Microstructure, shape memory effect and mechanical properties of rapidly solidified Co–Ni–Al magnetic shape memory alloys," *Materials Science and Engineering: A* 454–455 (2007) 423-432.
- [89] B. Bartova, N. Wiese, D. Schryvers, J. N. Chapman and S. Ignacova, "Microstructure of precipitates and magnetic domain structure in an annealed shape memory alloy," *Acta Materialia* 56 (2008) 4470-4476.
- [90] P. L. Potapov, P. Ochin, J. Pons and D. Schryvers, "Nanoscale inhomogeneities in melt-spun Ni–Al," *Acta Materialia* 48 (2000) 3833-3845.
- [91] H. E. Karaca, I. Karaman, D. C. Lagoudas, H. J. Maier and Y. I. Chumlyakov, "Recoverable stress-induced martensitic transformation in a ferromagnetic CoNiAl alloy," *Scripta Materialia* 49 (2003) 831-836.
- [92] N. Wanderka and U. Glatzel, "Chemical composition measurements of a nickel-base superalloy by atom probe field ion microscopy," *Materials Science and Engineering: A* 203 (1995) 69-74.
- [93] C. H. Liebscher, R. Voelkl and U. Glatzel, "Electron energy losses by channelling-enhanced microanalysis in a γ' -strengthened Ni-base alloy with Ti additions," *Acta Materialia* 57 (2009) 4217-4223.

- [94] E. P. George, C. T. Liu, J. A. Horton, C. J. Sparks, M. Kao, H. Kunsmann and T. King, "Characterization, processing, and alloy design of NiAl-based shape memory alloys," *Materials Characterization* 32 (1994) 139-160.
- [95] D. Schryvers and D. Holland-Moritz, "Martensitic transformations and microstructures in splat-cooled Ni-Al," *Materials Science and Engineering: A* 273–275 (1999) 697-702.
- [96] C. M. Wayman, "Shape memory alloys," *MRS Bulletin* 18 (1993) 49-56.
- [97] K. Otsuka and C. M. Wayman, Shape Memory Materials, (Cambridge University Press, Cambridge, UK, 1999).
- [98] M. N. Task, D. E. Kim, Z.-K. Liu, B. Gleeson, F. S. Pettit and G. H. Meier, "Phase stability and oxidation behavior of an alumina scale-forming NiCrAlY alloy," *Oxidation of Metals* 74 (2010) 179-191.
- [99] C. H. Xu, W. Gao and S. Li, "Oxidation behaviour of FeAl intermetallics – the effect of Y on the scale spallation resistance," *Corrosion Science* 43 (2001) 671-688.
- [100] B. A. Pint, J. R. Martin and L. W. Hobbs, "The oxidation mechanism of θ -Al₂O₃ scales," *Solid State Ionics* 78 (1995) 99-107.
- [101] B. A. Pint, J. R. Martin and L. W. Hobbs, "¹⁸O/SIMS characterization of the growth mechanism of doped and undoped α -Al₂O₃," *Oxidation of Metals* 39 (1993) 167-195.
- [102] A. Kumar, M. Nasrallah and D. L. Douglass, "The effect of yttrium and thorium on the oxidation behavior of Ni-Cr-Al alloys," *Oxidation of Metals* 8 (1974) 227-263.
- [103] F. H. Stott, G. C. Wood, Y. Shida, D. P. Whittle and B. D. Bastow, "The development of internal and intergranular oxides in nickel-chromium-aluminium alloys at high temperature," *Corrosion Science* 21 (1981) 599-624.
- [104] F. H. Stott and G. C. Wood, "The mechanism of oxidation of Ni-Cr-Al alloys at 1000°–1200°C," *Corrosion Science* 11 (1971) 799-812.
- [105] A. Ul-Hamid, "A TEM study of the oxide scale development in Ni–Cr–Al alloys," *Corrosion Science* 46 (2004) 27-36.
- [106] K. W. Richter and H. Ipser, "The Al–Ni–Si phase diagram between 0 and 33.3 at.% Ni," *Intermetallics* 11 (2003) 101-109.
- [107] M. Jain and S. P. Gupta, "Formation of intermetallic compounds in the Ni–Al–Si ternary system," *Materials Characterization* 51 (2003) 243-257.
- [108] V. Raghavan, "Al-Ni-Si (Aluminum-Nickel-Silicon)," *Journal of Phase Equilibria and Diffusion* 26 (2005) 262-267.

- [109] B. Cantor and R. W. Cahn, "Metastable alloy phases by co-sputtering," *Acta Metallurgica* 24 (1976) 845-852.
- [110] M. A. Bestor, Investigation of the Effect of Hafnium and Chromium Additions on the Microstructures and Short-Term Oxidation Properties of DC Magnetron Sputtered β -NiAl Bond Coats Deposited on Ni-Based Superalloys, Ph.D. Dissertation Thesis, The University of Alabama, Tuscaloosa, AL, 2010.
- [111] H. Guo, Y. Cui, H. Peng and S. Gong, "Improved cyclic oxidation resistance of electron beam physical vapor deposited nano-oxide dispersed β -NiAl coatings for Hf-containing superalloy," *Corrosion Science* 52 (2010) 1440-1446.